UNIVERSITÉ DE STRASBOURG

ÉCOLE DOCTORALE Mathématiques, Sciences de l'Information et de l'Ingénieur

Laboratoire iCube – UMR 7357

THÈSE présentée par :

Robin Faivre

soutenue le **05 novembre 2014**

pour obtenir le grade de : **Docteur de l'Université de Strasbourg**

Spécialité : Télédétection

Multi-sensor remote sensing parameterization of heat fluxes over heterogeneous land surfaces

THÈSE dirigée par :

Mme NERRY Françoise	Directrice de recherche, CNRS
M MENENTI Massimo	Professeur, TU Delft

RAPPORTEURS :

M SOBRINO José	Professeur, Universidad de Valencia
Mme OTTLÉ Catherine	Directrice de recherche, CNRS

AUTRES MEMBRES DU JURY :

Mme JIA LI	Professeur, Chinese Academy of Science
M NAJJAR Georges	HDR, Université de Strasbourg
M BASTIAANSSEN Wim	Professeur, TU Delft

Multi-sensor remote sensing parameterization of heat fluxes over heterogeneous land surfaces

PhD Thesis

Robin Faivre

Abstract

The parameterization of heat transfer by remote sensing, and based on SEBS scheme for turbulent heat fluxes retrieval, already proved to be very convenient for estimating evapotranspiration (ET) over homogeneous land surfaces. However, the use of such a method over heterogeneous landscapes (e.g. semi-arid regions or agricultural land) becomes more difficult, since the principle of similarity theory is compromised by the presence of different heat sources with various heights.

This thesis aims at first to propose and evaluate some models based on vegetation geometry for retrieving the surface roughness length for momentum transfer (z_{0m}), which is a key parameter in the characterization of heat transfer. Such an investigation can only be led at a small scale with very-high resolution remote sensing data, for a precise description of the land surface. Therefore, the second aspect of this work is to determine how to address the characterization of heat transfer for regional studies. Then, the reliability of SEBS for estimating turbulent heat fluxes at large spatial and temporal scales has been evaluated. To do so, the Multi-Scale SEBS approach (MSSEBS) has been implemented for a 2.4 million km^2 area including the Tibetan Plateau and the headwaters of the major rivers of East and South Asia. The addition of gap-filled hourly FY-2 LST data to advanced daily averaged net radiation and land surface parameters, allows to compute time-series of land surface ET over the Tibetan Plateau during the period 2008-2010, and on a daily basis.

Keywords: Optical remote sensing, heterogeneous land surfaces, surface energy balance, heat transfer, evapotranspiration, roughness length, LIDAR, meso-scale atmospheric model, spatial and temporal resolutions.

Preface

The achievement of a PhD is rarely the fact of a single candidate, it is rather the interaction with various people which contributes to make it possible.

Thus, I am first grateful to my promotor Massimo Menenti for offering me this PhD opportunity. I also really appreciated the inspiring discussions we had and the (precious) time and effort he has put into my thesis. My grateful thanks are extended to my second promotor Françoise Nerry for her support of my work. Her honest and critical looks into my manuscript were very valuable to me. My deep thanks to my third promotor Li Jia (RADI, Chinese Academy of Science), and especially for providing me all the needed data.

I express my great appreciation to Jérôme Colin for his scientific and pedagogic support during all these years. Our collaboration was initiated on my first internship among the TRIO team in 2008. He is obviously one of those who contributed to my academic and technical progression. I also acknowledge the whole TRIO team for its friendliness and cheerfulness, which contributed to nice working conditions.

Many thanks to Li Xin, Wang Jiemin and Hu Zeyong (CAREERI, Chinese Academy of Science) for giving me access to ground measurements performed in the Heihe River basin during the WATER project, and also for the answers to my technical issues. I also thank the ITP staff for the journey arrangements in Tibet, and for their support in the WP3 field campaign.

My keen appreciation goes to Kenishi Ueno (University of Tsukuba), Philippe Dobrinsky (LMD) and Fabien Maussion (TU Berlin) for their precious help and advices about WRF. Thanks again to Kenishi Ueno and also to Shiori Sugimoto (Hokkaido University) for providing the additional WRF dataset used in Chapter 7. A special thank to Antonio Lopes (University of Coimbra) for his support about the Windstation CFD model.

Many thanks to Liu Qiang (RADI, Chinese Academy of Science) for his precious help in the pre-processing of the LIDAR and WiDAS datasets. Thanks also to Zhansheng Li for checking the GRAPES data, and Bai Jie for the production of the EC footprint. A deep thank to Laure Roupioz for the production of the daily averaged net radiation maps. Good luck for the last rush! A great thank to our

former intern Nicolai Holzer (TU Dresden) for the development of some precious data processing tools. A warm thank to Hamid Ghafarian (TU Delft) for the gap-filled LST time-series, and for your special requests about heat flux time-series, it allowed me to produce more interesting results in this thesis. Many thanks to Wolfgang Babel (Bayreuth University) for the production of the Level 2 radiative and energy balance ground measurements at the four stations. A great recognition to Roderik Koenders (TU Delft) for the dutch translation of the propositions and the summary.

I would like to address my sympathy to all my friends of the SERTIT, with a special mention for Hervé Yésou who is clearly a benevolent godfather, for Claire Huber with who I started my geography studies ten years ago and developed a passion for remote sensing, and also for Carlos Uribe who is my first (but not last) colombian friend.

Thank you to all my friends, I had a great time with so many people during my PhD. If somebody expected to find his or her name here but doesn't, please forgive me, since the exhaustive list would be too long. A special thank to the employees and volunteers of the Bretz'Selle bicycle workshop, you really meant a lot to me, and I am sincerely glad to be your president.

I would like to thank my family for their encouragements, trust and support. Thanks to my parents for offering me the opportunity to achieve university studies. Thanks to my grandmother for her unconditional moral and material support during all these years.

Last but certainly not least, I would like to thank my beloved partner in life Luz Maria for just being who she is. Her love and trust in me were always a great motivation and an inexhaustible source of energy. Thank you Luz for having patience, I will be also there for you during your own PhD.

Robin Faivre
October 2014
Strasbourg, France

Contents

List of Figures

List of Tables

List of Symbols

A_f	Frontal area of a roughness element (-)
A_T	Total area covered by a roughness element (-)
B	Planck function (W/m^2/sr)
c_p	Air specific heat (10^3 J/(kg·K))
C_D	Obstacle drag coefficient (-)
C_R	Drag coefficient for an isolated obstacle (-)
C_s	Drag coefficient for an obstacle free surface (-)
d_0	Displacement height (m)
e_a	Water vapor pressure of air (Pa)
e_0	Saturation water vapor pressure of air (Pa)
ET	evapotranspiration (mm)
ET_d	Daily evapotranspiration (mm/day)
ET_h	Hourly evapotranspiration (mm/hour)
f_c	Fractional vegetation cover (-)
f_s	Fractional soil cover (-)
g	Acceleration due to gravity (m/s)
G_0	Soil heat flux density (W/m^2)
H	Sensible heat flux density (W/m^2)
H_c	Sensible heat flux density from foliage (W/m^2)
H_s	Sensible heat flux density from soil (W/m^2)
h_v	Vegetation height (m)
k	Von Karman constant (0.4)
kB^{-1}	Non-dimensional parameter (-)
$(kB^{-1})'$	Aerodynamic-radiometric non-dimensional parameter (-)
L	Monin-Obukhov length (m)
LAI	Leaf area index (m^2/m^2)
$Lw\downarrow$	Downward longwave radiation flux density (W/m^2)
Pr	Prandtl number (0.71)
r_{ah}	Aerodynamic resistance for heat transfer (s/m)
r_{ah}'	Aerodynamic-radiometric resistance because of the use of T_{rad} in a single-source model (s/m)

$r_{ah,c}$	Leaf boundary layer resistance (s/m)
$r_{ah,s}$	Soil boundary layer resistance (s/m)
$r_{ah,w}$	Aerodynamic resistance for heat transfer at the wet-limit (s/m)
r_{am}	Aerodynamic resistance for momentum transfer (s/m)
r_{aw}	Aerodynamic resistance for water vapor transfer (s/m)
r_{ex_r}	Aerodynamic resistance for heat transfer (s/m)
r_{ex0}	Excess resistance, identifies the difference between aerodynamic resistance for momentum transfer r_{am} and aerodynamic resistance for heat transfer r_{ah} (s/m)
r_{ex0}'	Aerodynamic-radiometric excess resistance (s/m)
R_i	Richardson number (-)
Rn	Net radiation flux density (W/m^2)
Rn_a	Daily average net radiation flux density (W/m^2)
Rn_c	Net radiation flux density absorbed by foliage (W/m^2)
Rn_L	Net longwave radiation flux density (W/m^2)
Rn_S	Net shortwave radiation flux density (W/m^2)
Rn_s	Net radiation flux density absorbed by soil surface (W/m^2)
$Sw\downarrow$	Downward shortwave radiation flux density (W/m^2)
T_a	Air temperature (K)
T_{aero}	Aerodynamic temperature (K)
T_b	Surface brightness temperature (K)
T_c	Canopy temperature (K)
T_{rad}	TOC radiometric temperature (K)
T_s	Soil temperature (K)
u	Wind speed (m/s)
$u*$	Friction velocity (m/s)
z	Reference height (m)
z_0	Source height (m)
z_{0h}	Roughness length for heat transfer (m)
z_{0m}	Roughness length for momentum transfer (m)
α	Albedo (-)
Δ	Rate of change of saturation water vapor pressure with temperature (Pa/K)
ϵ	Emissivity (-)
ϵ_c	Top-of-canopy emissivity (-)
ϵ_f	Vegetation emissivity (-)
ϵ_s	Soil emissivity (-)
γ	Psychrometric constant (Pa/K)
Γ_c	Ratio of soil heat flux to net radiation for full vegetation canopy (0.05)
Γ_s	Ratio of soil heat flux to net radiation for bare soil (0.315)

Λ	Evaporative fraction (-)
λE	Latent heat flux flux density (W/m^2)
λE_c	Latent heat flux flux density from foliage (W/m^2)
λE_s	Latent heat flux flux density from soil (W/m^2)
λ_f	Frontal area index (-)
λ_p	Plan area index (-)
Λ_r	Relative evaporation (-)
ψ_h	Monin-Obukhov stability correction function for heat transfert (-)
ψ_m	Monin-Obukhov stability correction function for momentum transfert (-)
ρ	Spectral reflectance (-)
ρ_a	Air density (kg/m^3)
σ	Constant of Stefan-Boltzmann (5.6704 $\cdot 10^{-8}$ W/m^2/K^{-4})
τ_0	Surface shear stress (kg/m^2/s)
θ_{av}	Virtual potential temperature of air (K)
θ_{s0}	Solar zenith angle ($^\circ$)
θ_v	Zenith view angle ($^\circ$)

List of Acronyms

AATSR	Advanced Along-Track Scanning Radiometer
AMS	Automatic Meteorological Station
ARW	Advanced Research WRF
ASL	Atmospheric Surface Layer
BAS	Bulk Atmospheric Similarity
CCD	Charge-Coupled Device
CFD	Computational Fluid Dynamics
DEM	Digital Elevation Model
DSM	Digital Surface Model
EBC	Energy Balance Closure
EC	Eddy Covariance system
ENVISAT	ENVIronment SATellite
EO	Earth Observation
FOV	Field Of View
JRA-25	Japanese 25-year Re-Analysis
LAI	Leaf Area Index
LAS	Large Aperture Scintillometer
LIDAR	Light Detection And Ranging
LSE	Land Surface Emissivity
LST	Land Surface Temperature
MODIS	MODerate resolution Imaging Spectroradiometer
MODTRAN	MODerate resolution TRANsmission model
MOS	Monin-Obukhov Similarity theory
MSSEBS	Multi-Scale Surface Energy Balance System
NASA	National Aeronautics and Space Administration
NCDC	National Climatic Data Center
NDVI	Normalized Difference Vegetation Index
NIR	Near InfraRed
NOAA	National Oceanic and Atmospheric Administration
NWPM	Numerical Weather Prediction Model
PBL	Planetary Boundary Layer

RMSE	Root Mean Square Error
SEB	Surface Energy Balance
SEBI	Surface Energy Balance Index
SEBS	Surface Energy Balance System
SLSTR	Sea and Land Surface Temperature Radiometer
SMTMS	Soil Moisture and Temperature Measurement System
SRB	Surface Radiative Balance
SW	Split Window
TIR	Thermal InfraRed
TOA	Top Of Atmosphere
TOC	Top Of Canopy
TP	Tibetan Plateau
VNIR	Visible and Near InfraRed
WATER	Watershed Allied Telemetry Experimental Research
WiDAS	Wide-Angle Infrared Dual-mode Line/Area Array Scanner
WRF	Weather Research and Forecasting

Chapter 1

General introduction

Evapotranspiration (ET) of land surfaces represents a key parameter for hydrological model closure and water management. Evapotranspiration is a common term of both water and energy balance of land surface, as the amount of water evaporated corresponds to the energy consumed in the liquid-vapor phase transition. Likewise, vapor transport is associated with (latent) heat transport. Latent heat flux stands for the energy transfer, which flows per time unit represented by water vaporization from land surface to the atmosphere. Evapotranspiration is controlled by soil moisture, vegetation type and its growing state, at-surface available energy and atmospheric state.

In these processes, it is crucial to determine accurately the partitioning of available energy into sensible heat flux (heating or cooling of the surface) and latent heat flux (evapotranspiration from surface) over a wide range of spatial and temporal scales. Observation and modeling of turbulent heat fluxes at the land surface has been a very active research area at least since the work of Bowen (1926) on the relative magnitude of heat transfer over dry and wet surfaces (Monteith, 1965; Feddes, 1971; Verma et al., 1976; Hall et al., 1979; Price, 1982; De Bruin and Jacobs, 1989; Beljaars and Holtslag, 1991; Lhomme et al., 1994). Most conventional techniques that employ point measurements to estimate the terms of energy balance are representative only of local scales and cannot be extended to large areas because of the land surface heterogeneity, of the dynamic nature and of the spatial distribution of heat transfer.

Remote sensing, with its capability of large spatial and frequent temporal coverage, has become a widely used and powerful tool to monitor land and environmental changes. Land surface properties, e.g. surface albedo, fractional vegetation cover, and land surface temperature, retrieved from Earth Observation (EO) in the optical spectral domain (i.e. from visible, near-infrared to thermal infrared) are used in many models dealing with hydrological, meteorological and ecological processes. The estimation and monitoring of ET by remote sensing has also be-

come a common application.

1.1 Heat exchange at the land-atmosphere interface

The exchange of heat at the land surface and atmosphere interface is dependent of the available energy, which is dissipated in three ways. A fraction enters in the soil and heats it by conduction, called the ground heat flux. The remaining energy is dissipated towards the atmosphere as turbulent convective exchange. The flow of momentum carries heat into the air (sensible heat flux) and water vapor (latent heat flux). The distribution of energy among the three heat fluxes is dependent on the surface properties and conditions. Depending on soil type and land use, the surface properties such as albedo and emissivity vary and alter the radiation balance. Surface conditions such as humidity, vegetation state and snow cover strongly influence the radiative forcing and result in a change of the surface temperature, available energy for turbulent heat fluxes and their partitioning. Also, the terrain morphology has to be taken into account besides horizontal heterogeneity. The latter includes both the spatial variability of land surface properties and the thermodynamic state of the land surface. The lower layers of the atmosphere are strongly coupled with land surface processes and, therefore, exhibit significant spatial heterogeneity.

Turbulent exchanges occur between land surface and atmosphere up to a level corresponding to the top of the planetary boundary layer (PBL). Beyond this layer, the atmosphere is free, its motion and thermodynamic state are not dependent of the surface. The height of the boundary layer has a daily cycle for which it reaches a maximum, due to the turbulent heat fluxes from the surface during the day. It acts as an integrator of the scalars exchanged; its development is progressive face to the strong spatial and temporal variability of fluxes from the surface. Its condition has a feedback effect because it determines the gradients of temperature and humidity and thus fluxes. This interaction between the boundary layer and the surface tends towards equilibrium when the whole layer is mixed. We then consider two scales to the properties of the boundary layer (McNaughton and Raupach, 1996) : the time required to achieve the balance (characteristic time scale), and the distance over which the air mass must move to achieve equilibrium (atmospheric length scale). The planetary boundary layer has not a uniform structure, but is usually subdivided into vertical sub-layers (Brutsaert, 1982) :

- The surface layer, located at the interface soil-atmosphere, mostly influenced by the surface heterogeneity and whose height is determined by surface heat fluxes.

- The mixing layer, upper part of the PBL where air mass is more homogeneous, and whose movement is determined by both the state of the surface and the Earth's rotation.

The sensible heat flux is related to the temperature gradient between the surface and a reference level. In the case of a homogeneous and infinite surface, it is assumed that the air mass is in equilibrium with the surface (i.e. vertical fluxes are constant) and a temperature measurement at a given level is representative of the temperature of the air mass at any point at this level. However, for the same atmospheric conditions, partitioning and density of the heat fluxes exchanged between the surface and the atmosphere varies greatly over an heterogeneous area. Thus, as each element of the surface creates its own internal boundary layer, we consider that the temperature measurement must be made at a reference level such that the effects of surface heterogeneities are incorporated into the mixed layer. However, it seems difficult that the gradient measured can be representative of turbulent fluxes exchanged by the underlying surface, since the surface layer is disturbed by the heterogeneous surroundings.

Although the measurement of heat fluxes is feasible at the scale of a meteorological station for homogeneous surfaces, it is impossible to perform large-scale measurements, across a watershed for instance. The use of a numerical weather prediction model (NWPM) coupled with a land surface model allows simulating the evolution of three-dimensional turbulent heat fluxes over time. However, this type of model requires many input variables, possible data assimilation and an important computation time. Furthermore, data from Earth Observation have demonstrated their usefulness for the spatialization of evapotranspiration and many studies have developed algorithms for estimating the energy balance over natural and cultivated areas (review of Li et al. (2009c), among others). Data acquired in the visible and near infrared allow for retrieving the surface albedo, which associated with the surface temperature measured in the thermal infrared domain enables for the spatialization of radiative balance. Variables such as the fractional vegetation cover (fc) or leaf area index (LAI) are used to characterize the land surface properties and are required to compute key parameters intervening in the parameterization of heat transfer (Choudhury et al., 1987; Su et al., 2001).

1.2 Surface energy balance algorithms

Some of the proposed algorithms allow partitioning of turbulent flow between a wet and dry limit expressed by the normalized temperature gradient between the surface and the atmosphere at a reference level (Li et al., 2009c). This concept proposed by Menenti and Choudhury (1993) is called Surface Energy Balance

Index (SEBI). The boundary conditions are either observed (Bastiaanssen et al., 1998; Roerink et al., 2000) or calculated (Su, 2002; Jia et al., 2003a; Colin, 2006). This type of approach already proved to be efficient for estimating the surface energy balance and relatively easy to implement.

The algorithm called Surface Energy Balance System (SEBS) formulated by Su (2002) is a parameterization scheme based on the concept of SEBI, which is known for its use both locally and regionally, and for any condition of atmospheric stability. The combination of remote sensing data acquired in the visible, near infrared (albedo, LAI, fc) and thermal infrared (land surface temperature) with the measurement of radiation at the surface and atmospheric variables at reference level (temperature, wind speed, specific humidity) allows to calculate the actual temperature gradients as well as the wet and dry limits, between the surface and the atmosphere for each pixel. Su (2002) also adapts the choice of stability functions depending on whether the reference level considered is located in the surface layer or in the mixing layer (Brutsaert, 1999).

Independently of the measurement errors related to the different atmospheric variables or models to retrieve surface parameters (temperature, albedo, LAI, among others), SEBS is sensitive to the parameterization of the aerodynamic resistance (r_{ah}), i.e. resistance to the heat transfer in a layer of atmosphere. The expression of resistance requires the calculation of aerodynamic roughness length for heat transfer (z_{0h}), estimated from the aerodynamic roughness length for momentum transfer (z_{0m}) through the kB^{-1} model (Massman, 1999). The roughness length for momentum, which scales the vertical wind profile, is influenced by the surface geometry and thus changes in space and time. Numerous methods for estimating aerodynamic roughness length by remote sensing have been developed. However, the roughness models for z_{0m} retrieval used in SEBS are defined from empirical relationships generally based on NDVI and for specific and uniform vegetation. Their use for the characterization of heterogeneous surfaces is outside from their domain of validity. Moreover, these models do not take into account the dynamic aspect of the roughness length : the rapid change of wind speed and direction in a local context with the presence of obstacles may result in a significant temporal variability. Su et al. (2001) then recognize that the use of models to estimate roughness length is not always appropriate in the sense that they ignore the flow history of an air mass over heterogeneous areas.

In the case of regional studies, the sampling resolution of spaceborne sensors becomes coarse (e.g. 1 km) and the grid size of atmospheric data is even larger. At this scale, we can consider that the aggregation effect of surface heterogeneity and air mass avoids to consider the local surface roughness, at least for natural land surfaces since large urban areas will not be addressed in this dissertation. Menenti et al. (1996) consider that there is a scale at a regional level from which the roughness length is independent of the wind direction, allowing the use of a

static definition of this parameter. The main obstacles to air flow are represented by the difference between bare soil (smooth) and vegetation (more or less rough), and obviously the presence of terrain relief. Roughness due to elevation remains constant over time, but that induced by vegetation will present an annual cycle, more or less important depending on vegetation type and climate.

Beyond the proper characterization of the surface geometry, which is finally rather limited at large scales, there are also some other issues that emerge. Typically, meso-scale studies rely on the combination of visible and near-infrared (VNIR) EO data with thermal infrared (TIR) data and with PBL atmospheric fields (NWPM outputs) which all have their own spatial resolution. One major difficulty is to define a proper scale (i.e. the atmospheric length scale) for computing the aerodynamic resistance to heat transfer and its associated roughness lengths (z_{0m}, z_{0h}), between an atmospheric extent and the underlying land surface.

Also, most of the energy balance algorithms using remotely sensed data produce only instantaneous evapotranspiration values. Obviously, it is necessary to convert instantaneous ET value at the overpass times of satellites to daily or longer time step, to make full use of the remote sensing data in hydrological applications. Moreover, the advantage to work with medium to low resolution EO data, is that the temporal resolution for land surface observation and heat flux monitoring can be considerably increased. In such context, surface energy balance calculations can easily reach a daily basis, or even up to an hourly frequency with geostationary satellites, which is convenient for investigating temporal integration strategies.

1.3 Objectives of the thesis

From the above discussion, some questions can be raised and the objective of this thesis is to try to answer them. These questions can be formulated as follows :

- Does the geometric characterization of the surface provide a better estimation of the variables involved in the turbulent heat exchanges ?

- Can we improve the characterization of mass and heat transfer over heterogeneous areas by taking into account the dynamic aspects of air flow ?

- Does a better characterization of surface roughness at large scale (i.e. terrain relief) have an influence on the estimation of turbulent heat fluxes ?

- Is the SEBS algorithm suitable for monitoring heat fluxes over large areas and at a high temporal frequency ?

All these questions will be addressed by exploiting a large set of various remote sensing data. Different land surface properties and processes must be characterized at the appropriate spatial resolution, but higher spatial resolution implies almost inevitably a lower temporal resolution, and thus less case studies. The complete workflow of this thesis is detailed below and is also summarized in Figure 1.1.

First, the work will consist in locally characterizing the surface geometry using a digital surface model (DSM) obtained by the acquisition from an airborne imaging LIDAR system. The introduction of the surface model in a Computational Fluid Dynamics (CFD) model will allow to generate a 3D wind field. The inversion of wind vertical profiles will enable to produce a 2D mapping of aerodynamic roughness length for momentum transfer. Two geometrical approaches which account for wind direction will also be applied to the digital surface model.

In order to evaluate the reliability and accuracy of geometrical models and the CFD-based method for roughness length retrieval, they will be compared to three other simpler formulations which correspond to a static definition of z_{0m}. The assessment will be performed through various SEBS calculations of turbulent heat fluxes integrating the respective spatialized roughness values. The performance of each method will be determined by comparing results with ground measurements of heat fluxes. Moreover, SEBS calculations require the combination of land surface properties (such as albedo, radiative temperature, emissivity, LAI and f_c) and atmospheric measurements (air temperature, wind speed and specific humidity). Land surface variables have to be retrieved from very high-resolution visible and near-infrared (VNIR) to thermal infrared (TIR) remotely sensed observations.

Also, the evaluation of z_{0m} retrieval has to be extended beyond the local context of a meteorological station since many hydrological studies aims at modeling water cycle at regional, continental or even global scales. In this way, a retrieval method which is able to take in account the influence of relief for large scale applications has to be evaluated. Moreover, since the aerodynamic resistance is sensible to both roughness lengths for heat and momentum transfer, it appears obvious to at least evaluate two different kB^{-1} models in SEBS. These two aspects lead to an interesting crossed assessment of z_{0m} and z_{0h} (through kB^{-1} model) parameterizations at different spatial scales.

The final aspect of this work will be to combine advanced land surface products, midday observations of land surface temperature (LST) and the corresponding atmospheric variables to produce an instantaneous estimate of turbulent heat fluxes at a daily frequency over the whole Tibetan Plateau. This also implies to define a length scale for computing aerodynamic resistances, which has to be consistent with both the various spatial resolutions of input data and the involved processes. From these instantaneous energy balance calculations, an integration strategy able to well reproduce the diurnal pattern of heat fluxes has to be selected,

in order to provide a daily evapotranspiration rate. The availability of hourly gap-filled LST observations and atmospheric variables for high-frequency SEBS calculations allows to explore the benefit of such daily integrations, mainly during cloudy sky conditions when radiative forcing and surface response are changing.

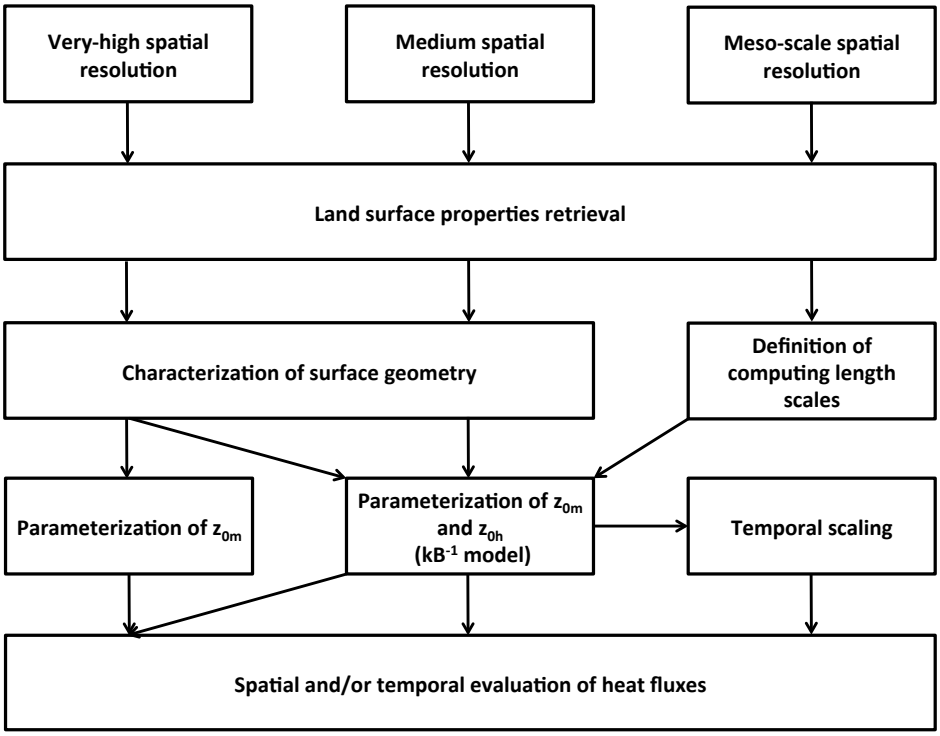

Figure 1.1: Flowchart of the data analysis addressed in the thesis.

1.4 Organization of the document

Chapter 2 is dedicated to the estimation of evapotranspiration by remote sensing. The theoretical basis of energy fluxes modeling is first described. Then, the Surface Energy Balance Index (SEBI) concept proposed by Menenti and Choudhury (1993) is explained, since it is mainly at the origin of the Surface Energy Balance System (SEBS) elaborated by Su (2002), and thus essential for understanding the conceptual approach. A rapid description of SEBS algorithm is also given.

Chapter 3 first presents all the study areas involved in this thesis : the Heihe river basin with the Yingke and A'rou experimental stations, and the Tibetan Plateau with its four observation sites. The different datasets used in this work

are also detailed : spaceborne and airborne remote sensing data, observed and simulated meteorological variables.

In Chapter 4, investigations on the roughness length for momentum transfer retrieval are described (Colin and Faivre, 2010). The exploitation of gridded LIDAR data allows to produce very-high resolution digital elevation and surface models (DEM & DSM). The DSM highlights the local surface micro-topography such as vegetation structure, and is very suitable for applying two geometrical models of roughness length retrieval proposed by Raupach (1994) and MacDonald et al. (1998) respectively, and also for experimentations about inversion of wind fields generated by a CFD model (Lopes, 2003).

Chapter 5 first addresses the production of land surface parameters from very-high resolution VNIR and TIR data. The methods proposed in Chapter 4 (geometrical and aerodynamical) for roughness length retrieval are then evaluated through respective SEBS calculations. Three other simpler formulations for z_{0m} retrieval are also included in order to assess whether taking into account dynamic aspects provides a better characterization of heat transfer, compared to static definitions. This work will be performed at the footprint scale of ground measurements (Eddy Covariance system).

In Chapter 6, both z_{0m} and kB^{-1} parameterizations will be assessed through a cross evaluation. Two promising roughness length retrieval methods and two different kB^{-1} models will be compared through a set of SEBS calculations. The same study will be performed at a larger scale with specific z_{0m} retrieval methods for taking in account relief and/or vegetation. A pre-processing for land surface parameters retrieval from medium resolution remotely sensed data is still necessary and all the specific procedure will be detailed.

Chapter 7 addresses the ability of SEBS to produce meso-scale daily evapotranspiration time-series, with a demonstration over the entire Tibetan Plateau for the period 2008-2010. The multi-scale approach proposed by Colin (2006) will be applied to SEBS for dealing with spatial resolutions. Then, from one estimation of turbulent heat fluxes per day, two methods for daily ET scaling will be evaluated. Hourly calculations, based on hourly LST observations from geostationnary satellite, will be also produced during one month in order to evaluate the benefit of daily integrations. Validations are based on the comparison with flux measurements performed at four observation stations located on the Qinghai-Tibet Plateau.

Chapter 8 presents the general conclusion of the thesis. It reminds the main objectives of this work and summarizes the results obtained and observations made respectively in each chapter. The improvements and perspectives for further studies are also addressed.

1.5 Programmatic context

This work takes benefit from the synergy between three scientific projects focused on cold and arid regions in China : CEOP-AEGIS, WATER and ESA-MOST Dragon 2 Programme. Their complementarities are summarized by the Figure 1.2. The Dragon 2 Programme, supported by the European and Chinese space agencies, acts as an important remote sensing data provider. The CEOP-AEGIS project benefits of these datasets for improving retrieval methods to produce enhanced products. The WATER project is also essential for providing a large panel of intense ground observations, required for the validation of retrieval algorithms, but takes also benefit from the remote sensing dataset availability for modeling and data assimilation purposes. Each project will be briefly detailed in the following sections.

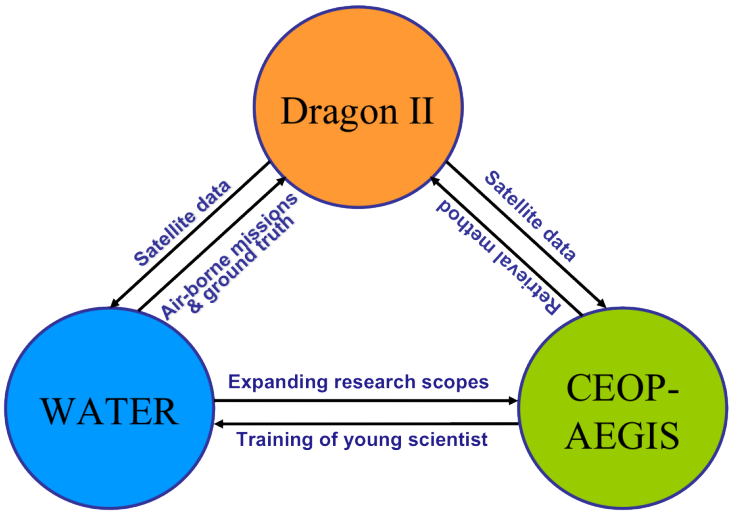

Figure 1.2: Diagram representing complementarities between Dragon 2 Programme, WATER and CEOP-AEGIS projects.

1.5.1 CEOP-AEGIS project

CEOP-AEGIS stands for *"Coordinated Asia-European long-term Observing system of Qinghai-Tibet Plateau hydro-meteorological processes and the Asian monsoon systEm with Ground satellite Image data and numerical Simulations"*. It is a Collaborative Project / Small or medium-scale focused research project - Specific International Cooperation Action financed by the European Commission under FP7 topic ENV.2007.4.1.4.2 "Improving observing systems for water resource management", and is coordinated by the Université de Strasbourg, France.

Initiated in May 2008 and with a duration of 60 months, the CEOP-AEGIS project aims at building such a long-term observing system for the Tibetan Plateau to monitor surface bio-geophysical properties, energy and water balance, and to improve the modeling of the Asian monsoon and of extreme meteorological events. Three main elements are foreseen (Figure 1.3) :

- Observations of precipitation, meltwater from snow and glaciers, changes in soil water content and evaporation for a period of three years have been generated by integrating ground and satellite measurements on daily, weekly and monthly basis. Radiative transfer models and algorithms have been developed for different regions of the electro-magnetic spectrum.

- The water balance of the Plateau has been calculated with a distributed hydrological model. Interactions of land surface hydrology with convective activity and the Asian Monsoon are being investigated by using a mesoscale atmospheric model.

- Time-series of image data have been used to demonstrate a Drought and a Flood Early Warning System.

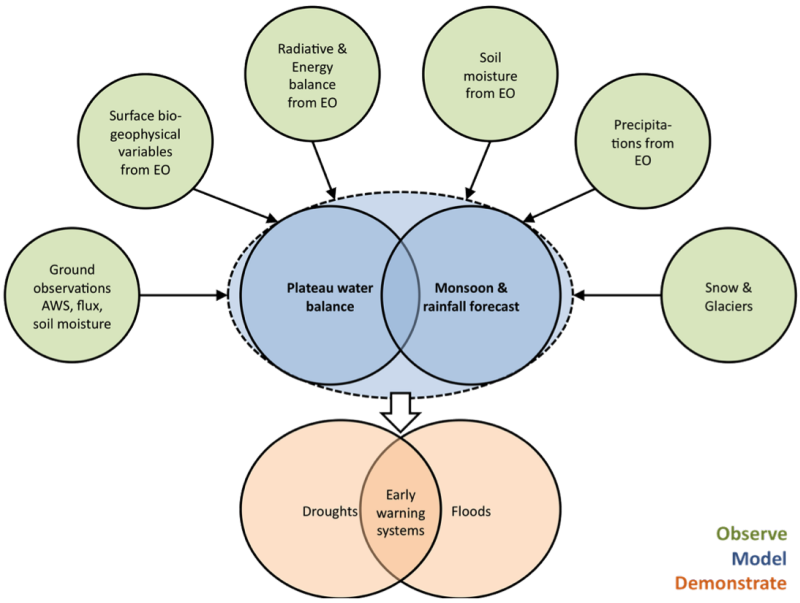

Figure 1.3: The CEOP-AEGIS project is composed of ten research work-packages that can be organized in three categories, as illustrated on the figure : Observe (in green), Model (in blue) and Demonstrate (in orange).

1.5.2 WATER project

The Watershed Allied Telemetry Experimental Research (WATER) is a simultaneous airborne, satellite-borne, and ground-based remote sensing experiment aiming to improve the observability, understanding, and predictability of hydrological and related ecological processes at a catchment scale. WATER consists of the cold region, forest, and arid region hydrological experiments as well as a hydrometeorology experiment and took place in the Heihe river basin (Figure 1.4), a typical inland river basin in the northwest of China. The field campaigns have been completed, with an intensive observation period lasting from 7 March to 12 April, from 15 May to 22 July, and from 23 August to 5 September 2008 : in total, 120 days. Twenty-five airborne missions were flown. Airborne sensors including microwave radiometers at L, K, and Ka bands, imaging spectrometer, thermal imager, CCD, and LIDAR were used. Various satellite data were collected. Ground measurements were carried out at four scales, that is, key experimental area, foci experimental area, experiment site, and elementary sampling plot, using ground-based remote sensing instruments, densified network of automatic meteorological stations, flux towers, and hydrological stations. On the basis of these measurements, the remote sensing retrieval models and algorithms of water cycle variables was developed or improved, and a catchment-scale land/hydrological data assimilation system was developed.

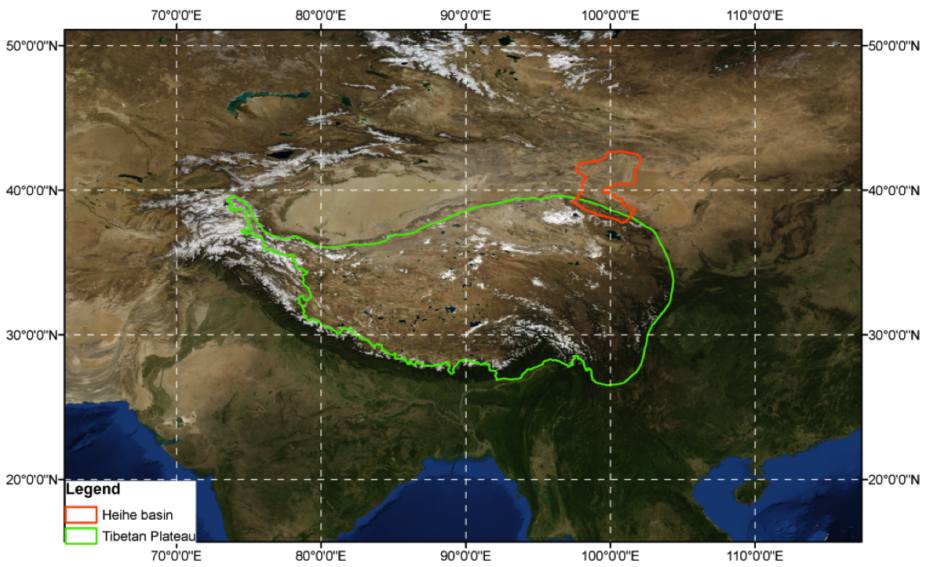

Figure 1.4: Localization of the Tibetan Plateau (green) and the Heihe River basin (red).

1.5.3 ESA-MOST Dragon 2 Programme

The Dragon Programme is a cooperation between European Space Agency (ESA) and the Ministry of Science and Technology (MOST) of the P.R. China. The first Dragon Programme commenced in 2004 and was completed in April 2008. The second Dragon Programme had a duration of four years and was formally commenced at the 2008 Beijing Symposium. Dragon 2 focused on exploitation of ESA, Third Party Mission and Chinese Earth Observation data for science and applications development in land, ocean and atmospheric applications. The Programme brought together joint Sino-European teams to investigate 25 thematic projects.

This work is part of the project id. 5322 *"Key eco-hydrological parameters retrieval and land data assimilation system development in a typical inland river basin of China's arid region"*. The goal of the project was to improve the monitoring, understanding, and predictability of hydrological and ecological processes at catchment scale, and promote the applicability of quantitative remote sensing in watershed science. Some key hydrological and ecological variables were retrieved in virtue of ESA and other satellite data and were merged into hydrological modeling for a more coherent and precise representation of water cycle at catchment scale.

Chapter 2

Estimation of evapotranspiration by remote sensing

2.1 Introduction

The relation between energy balance, heat flux density and surface temperature is long known and was investigated in many early studies and gained in interest with the larger availability of thermal remote sensing data, paving the way for remote monitoring of evapotranspiration. Figure 2.1 summarizes progress made in the last three decades for remote sensing of surface heat balance (Menenti, 2000; Li et al., 2009c), from early studies on linear relationships between surface temperature and evapotranspiration (Jackson et al., 1977), to relationships between spectral indices with evapotranspiration (Price, 1990); the Soil Vegetation Atmosphere Transfer (SVAT) model approaches (Taconet and Vidal-Madjar, 1988), sometimes combined with Planetary Boundary Layer models (Carlson et al., 1981); and more recent work on the relative position of observed surface temperature within two extreme boundaries, i.e. fully wet and completely dry surfaces, and corresponding temperature gradient (Menenti and Choudhury, 1993).

The obvious weakness of the simplified empirical regression method is that it is site specific and has limitations for applications over large heterogeneous areas. On the other hand, the large number of variables needed for SVAT models is a significant limitation for studies that usually cover large areas, although recent efforts from the community to build global databases progressively fill the gap (e.g. ECOCLIMAP, ECOCLIMAP-II, HWSD, etc.). The third concept elaborated by Menenti and Choudhury (1993) and presented hereafter, gives ground to a more general approach based on the relationship between surface temperature, surface reflectance and flux partitioning between sensible and latent heat. The former category can be further subdivided into single-source, dual-source or multi-source

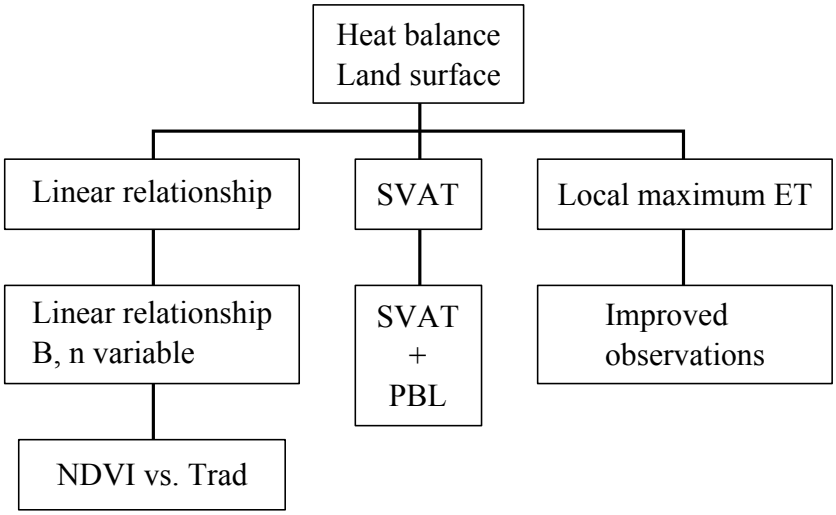

Figure 2.1: Overview of methods based on the heat balance equation, from Menenti (2000).

models corresponding with a single-, dual- or multi-layer schematization of the surface respectively.

In this chapter, the theory of energy balance modeling is first presented. Then, the Surface Energy Balance Index (SEBI) concept elaborated by Menenti and Choudhury (1993) for turbulent heat fluxes partitioning and evapotranspiration retrieval is presented. This concept is the starting point of the Surface Energy Balance System (SEBS) parameterization scheme developed by Su (2002) and which allows to first determine sensible heat flux and then the latent heat flux through the relative evaporation. The SEBS algorithm belongs to the category of single-source models since it describes a 1D system : the surface is treated as a single source of heat exchanged with the overlying atmosphere, and heat transfer is estimated on the basis of similarity theory.

2.2 Theoretical basis of energy fluxes modeling

Radiative and energy balance at the land surface

Taking the land surface as a flat and thin layer such that no heat storage exists, the surface energy balance equation at the interface between the land surface and the overlying atmosphere is written as :

$$Rn = H + \lambda E + G_0 \tag{2.1}$$

where Rn is the net radiation flux, H is the sensible heat flux, λE is the latent heat flux and G_0 is the soil heat flux. The sign convention in Equation 2.1 is that Rn is considered positive when directed towards the land surface, while H, λE and G_0 are considered positive when directed away from the land surface. For the sake of simplicity, all flux densities will be called fluxes,and the unit is W/m^2.

The net radiation is the sum of the shortwave and longwave contributions :

$$Rn = Rn_S + Rn_L \tag{2.2}$$

with Rn_S the net shortwave radiation expressed as :

$$Rn_S = (1 - \alpha) \cdot Sw \downarrow \tag{2.3}$$

$Sw \downarrow$ is the shortwave irradiance, also called the global radiation as it sums both the direct and diffuse components, and α is the broadband surface albedo.

The net longwave radiation Rn_L is expressed as :

$$Rn_L = Lw \downarrow - \epsilon\sigma T^4 \tag{2.4}$$

where $Lw \downarrow$ is the longwave atmospheric emittance, ϵ the broadband surface emissivity, σ the Stephan-Boltzmann constant, and T the land surface radiometric temperature (K).

Incoming solar radiation is mainly driven by the azimuth and zenith angle of the sun at a given position and time. However, many other factors have to be taken into account to reproduce global radiation correctly. In particular, ground elevation and relief determine the direct incoming radiation pattern in mountainous areas, cloud cover can reduce direct radiation, and atmospheric aerosols content will significantly affect the contribution of diffuse radiation to the global radiation. Atmospheric radiation is mainly driven by atmosphere temperature and column water content (and by extension cloud type and content). The vertical structure and properties of the atmosphere must be known to reproduce the surface radiative fluxes.

The soil heat flux is often parameterized proportionally to the net radiation arriving at the soil surface, therefore is function of the fractional vegetation cover (Choudhury et al., 1987; Bastiaanssen and Bandara, 2001; Murray and Verhoef, 2007). It can be expressed as :

$$G_0 = Rn \cdot (\Gamma_c + (1 - f_c) \cdot (\Gamma_s - \Gamma_c)) \tag{2.5}$$

in which it is assumed that the ratio of soil heat flux to net radiation $\Gamma_c = 0.05$ for full vegetation canopy (Monteith and Unsworth, 1973) and $\Gamma_s = 0.315$ for bare soil (Kustas and Daughtry, 1989). An interpolation is then performed between these limiting cases using the fractional vegetation cover (f_c).

Single-source parameterization of H and λE

In the context of applying remote sensing measurements to estimate heat fluxes, the latent heat flux (or evaporation when expressed in term of water depth) is calculated as the residual of energy balance (Equation 2.1) and the major concern is to calculate sensible heat flux by a proper parameterization of resistance for heat transfer r_{ah}. The sensible heat flux is related to the difference between the air temperature at a source height z_0 for heat transfer (so-called aerodynamic surface temperature, T_{aero}) and air temperature T_a at a reference height z within surface layer by a bulk transfer equation (Monteith and Unsworth, 1973) :

$$H = \rho_a c_p \frac{T_{aero}(z_0) - T_a(z)}{r_{ah}(z_0, z)} \tag{2.6}$$

where ρ_a is the air density (kg/m^3), c_p is the heat capacity of the air (J/kg/K), $r_{ah}(z_0, z)$ is the aerodynamic resistance for heat transfer (s/m) between source height (z_0) and the reference height (z) in the Atmospheric Surface Layer (ASL), usually estimated on the basis of similarity theory.

The source height is the fictive level at which the air temperature should take its "surface" value. In practice, T_{aero} is mathematically computed by extrapolating a logarithmic temperature profile to the effective source height, i.e. the roughness length for heat transfer (z_{0h}) and is usually not measurable directly. The aerodynamic resistance for heat transfer $r_{ah}(z_{0h}, z)$ is given by (Monteith and Unsworth, 1973; Brutsaert, 1999) :

$$r_{ah}(z_{0h}, z) = \frac{1}{k u_*} \left[\left(ln \frac{z - d_0}{z_{0h}} \right) - \psi_h \left(\frac{z - d_0}{L} \right) + \psi_h \left(\frac{z_{0h}}{L} \right) \right] \tag{2.7}$$

where k is the Von Karman constant (k = 0.4), d_0 is the displacement height (m), ψ_h is the Monin-Obukhov stability correction function for heat transfer, and u_* is the friction velocity (m/s) in the ASL (defined as $(\tau_0/\rho_a)^{1/2}$ with τ_0 the surface shear stress) and is expressed as :

$$u_* = \frac{k u_z}{ln \left(\frac{z - d_0}{z_{0m}} \right) - \psi_m \left(\frac{z - d_0}{L} \right) + \psi_m \left(\frac{z_{0m}}{L} \right)} \tag{2.8}$$

with z_{0m} the roughness length for momentum transfer (m), ψ_m is the Monin-Obukhov stability correction function for momentum transfer, and L in Equations 2.7 and 2.8 is the Monin-Obukhov length given as :

$$L = -\frac{\rho_a c_p u_*^3 \theta_{av}}{k g H} \tag{2.9}$$

where θ_{av} is the potential virtual air temperature near the surface (K).

The term "excess resistance" r_{ex0} has been used to identify the difference between aerodynamic resistance for momentum transfer r_{am} and aerodynamic resistance for heat transfer r_{ah} (Verma, 1989).

$$r_{ah} = r_{am} + r_{ex0} \tag{2.10}$$

This "excess resistance" r_{ex0} is expressed as a function of a non-dimensional parameter kB^{-1} (Verma, 1989) :

$$r_{ex0} = \frac{1}{ku_*} kB^{-1} \tag{2.11}$$

kB^{-1} is defined by the ratio z_{0m} over z_{0h} as (Chamberlain, 1966; Owen and Thomson, 1968) :

$$kB^{-1} = ln\left(\frac{z_{0m}}{z_{0h}}\right) \tag{2.12}$$

B is the dimensionless parameter introduced by Chamberlain (1966) and used by Owen and Thomson (1968). The definition of kB^{-1} (Equation 2.12) provides a measure of the difference in the sources and source heights determining heat and momentum transfer (Thom, 1972). By definition, the source height for heat transfer is lower than the sink height for momentum transfer. This is equivalent to say that the aerodynamic resistance for heat transfer is larger than aerodynamic resistance for momentum transfer. Therefore, the theoretical basis of the kB^{-1} parameter is strictly aerodynamic, i.e. related to the aerodynamic surface temperature.

When using remote sensing thermal infrared (TIR) measurements in classic single-source formulations (Equations 2.6, 2.7, 2.8 and 2.9), the assumption is generally made that the surface radiometric temperature (T_{rad}) measured by a radiometer is equivalent to T_{aero}. T_{rad} can be measured either by airborne or spaceborne sensors which makes regional estimation of heat fluxes possible. Over dense and wet vegetated surface, surface radiometric temperature is very close to surface aerodynamic temperature. However, as addressed in the first place by Rosenberg et al. (1983), for partially vegetated and water stressed surfaces, the radiometric and aerodynamic temperatures of the surface are not equal. Intensive studies have been carried out in the last decades in evaluating theoretically and experimentally the difference between the surface radiometric and aerodynamic temperatures. Large differences between T_{rad} and T_{aero}, ranging up to 10°C, have been observed for partial canopies (Choudhury et al., 1986; Huband and Monteith, 1986; Kustas and Norman, 1999). The difference between T_{rad} and T_{aero} can be taken into account by adding an additional term r_{ex_r} to the traditional

aerodynamic resistance r_{ah} (Equation 2.10) :

$$r'_{ah} = r_{ah} + r_{ex\_r} \tag{2.13}$$

where r_{ex_r} is the resistance to account for the difference between T_{rad} and T_{aero}. Substituting Equation 2.10 to Equation 2.13, r'_{ah} leads to :

$$\begin{aligned} r'_{ah} &= r_{am} + r_{ex0} + r_{ex\_r} \\ &= r_{am} + r'_{ex0} \end{aligned} \tag{2.14}$$

where r'_{ex0} is referred to as "aerodynamic-radiometric excess resistance", and r'_{ah} is the "aerodynamic-radiometric resistance" for heat transfer.

By analogy with Equation 2.11, this additional resistance r'_{e0} may be expressed as a supplementary correction for kB^{-1} (Equation 2.12) :

$$r'_{ex0} = \frac{1}{ku_*}(kB^{-1})' \tag{2.15}$$

Thus, the term $(kB^{-1})'$, referred to as "aerodynamic-radiometric kB^{-1}", is a parameter to determine the aerodynamic-radiometric excess resistance r'_{ex0}, which relates H to T_{rad} and differs from its theoretical definition (Equation 2.12) due to the use of T_{rad} instead of T_{aero}. For the sake of simplicity, the symbols kB^{-1} and r_{ah} will be retained, but one should note their meaning, i.e. aerodynamic and radiometric, if T_{rad} is used in a single-source model to estimate sensible heat flux. If an appropriate value of kB^{-1} is determined, H can be estimated accurately by using T_{rad}.

By analogy, latent heat flux is expressed by a bulk transfer equation as :

$$\lambda E = \frac{\rho_a c_p}{\gamma} \frac{e_0 - e_a}{r_{aw}} \tag{2.16}$$

where λ is the latent heat for vaporization of water (J/kg), E is the actual evaporation rate (mm/s), γ (Pa/K) is the psychrometric constant, e_0 (Pa) is the surface vapor pressure, e_a (Pa) is the actual water vapor pressure of the air at temperature T_a, r_{aw} is the bulk aerodynamic resistance for water vapor transfer between the source height of water vapor (z_{0w}) and reference height (z_{ref}) in the ASL.

Assuming the land surface or soil-vegetation system can be represented as a big leaf and introducing two resistances in series, aerodynamic resistance between "surface" and reference height in ASL and canopy surface resistance (r_c) which regulates the evapotranspiration from the vegetation by adjusting the stomata aperture, latent heat flux can be written as in the Penman-Monteith combination equation (Monteith, 1965) :

$$\lambda E = \frac{\Delta r_{ah}(z_{0h}, z)(Rn - G_0) + \rho_a c_p \left[e_*(T_{aero}(z_{0h})) - e_a(T_a(z))\right]}{r_{ah}(z_{0h}, z)(\gamma + \Delta) + \gamma r_c} \tag{2.17}$$

where Δ is the slope of saturated vapor pressure at the air temperature T_a. In the Penman-Monteith Equation (2.17), the following assumptions and procedure are involved :

- aerodynamic resistance for water vapor transfer r_{aw} is the same as for heat transfer r_{ah},
- the surface vapor pressure e_0 is equal to the saturation water vapor pressure e_* at temperature T_{aero},
- Equations 2.1, 2.6 and 2.16 are combined to derive Equation 2.17.

For surface fully covered by wet vegetation or open water (r_i = 0), Penman-Monteith equation is reduced to Penman equation (Penman, 1948) which deals with the potential evaporation from a surface :

$$\lambda E_p = \frac{\Delta r_{ah}(z_{0h}, z)(Rn - G_0) + \rho_a c_p \left[e_*(T_{aero}(z_{0h})) - e_a(T_a(z))\right]}{r_{ah}(z_{0h}, z)(\gamma + \Delta)} \tag{2.18}$$

Dual-source parameterization of H and λE

The dual-source models make a difference between the surface energy transfer of soil and canopy sub-systems. These models allow to distinguish radiometric and aerodynamic surface temperatures by incorporating the effects of sensor view geometry to partition surface energy and temperature into soil and vegetation sub-components. The addition of excessive resistance into aerodynamic resistance can be avoided. This approach is very convenient for heterogeneous land surface, i.e. partial canopies which are geometrically and thermally heterogeneous. For instance, in many semi-arid environments where the surfaces are partially covered by vegetation, both the soil surface and cooler foliage determine the heat exchanges. The sensible heat flux from such canopy system can be expressed as :

$$H = H_c + H_s \tag{2.19}$$

where the contributions from foliage and from the soil component are :

$$H_c = LAI \frac{2\rho_a c_p}{r_{ah,c}} \left[T_c - T_{aero}(z_0)\right] \tag{2.20}$$

$$H_s = f_s \frac{\rho_a C_p}{r_{ah,s}} \left[T_s - T_{aero}(z_0) \right] \tag{2.21}$$

where f_s is the fractional soil cover, $r_{ah,c}$ the leaf boundary layer resistance and $r_{ah,s}$ the soil boundary layer resistance.

To estimate H_c and H_s from Equations 2.20 and 2.21, one must know $r_{ah,c}$, $r_{ah,s}$ and $T_{aero}(z_0)$. T_c and T_s can be derived from bi-angular TIR radiance measurements for instance (Jia, 2004). The parameterization of $r_{ah,c}$ and $r_{ah,s}$ is also detailed by Jia (2004). Combining Equations 2.6, 2.20 and 2.21, $T_{aero}(z_0)$ is expressed as :

$$T_{aero}(z_0) = \frac{\frac{T_a(z)}{r_{ah}(z_0,z)} + 2LAI \frac{T_c}{r_{ah,c}} + f_s \frac{T_s}{r_{ah,s}}}{\frac{1}{r_{ah}(z_0,z)} + \frac{2LAI}{r_{ah,c}} + \frac{f_s}{r_{ah,s}}} \tag{2.22}$$

Equation 2.22 shows that $T_{aero}(z_0)$ is treated as an ancillary variable and can be expressed as a function of other variables. This implies that precise knowledge of the apparent heat source height z_0 in the dual-source approach is not as critical as in a single-source model and can be taken as an arbitrary height inside the canopy.

λE_c and λE_s are then respectively determined as the residuals of the sub energy balances Rn_c and Rn_s :

$$Rn_c = H_c + \lambda E_c \tag{2.23}$$

$$Rn_s = H_s + \lambda E_s \tag{2.24}$$

with Rn_c described as a function of LAI :

$$Rn_c = Rn(1 - e^{-k_a LAI}) \tag{2.25}$$

where k_a is the extinction coefficient, in the range 0.3-0.6 according to the observations. Then Rn_s can be estimated as :

$$Rn_s = Rn - Rn_c \tag{2.26}$$

The physical description of a dual-source approach is obviously more rigorous when considering heterogeneous land surfaces. However, this requires specific dual-view capabilities for remote sensing sensors, which represents an important technical limitation. Because of its use with any VNIR and TIR multi-spectral sensors, only the single-source parameterization of heat fluxes is retained in this study. Moreover, all the thermal gradients and their related resistances are now expressed between the effective source height (z_{0h}) and the reference height (z).

2.3 The Surface Energy Balance Index concept

By grouping the resistance terms into the bulk internal resistance (r_i) (or surface, or stomatal) and external resistances (i.e. the aerodynamic resistance r_{ah}), Menenti (1984) proposed another combination equation for actual evaporation which can also be applied to a soil surface with properly defined internal bulk resistance r_i :

$$\lambda E = \frac{\Delta r_{ah}(Rn - G_0) + \rho_a c_p (e_* - e_a)}{r_{ah}(\gamma + \Delta) + \gamma r_i} \tag{2.27}$$

Since the generic term of internal resistance apply for both bare soil and vegetation, it avoids to differentiate soil evaporation from plant transpiration. The difficulty of using Equation 2.27, especially at the regional scale, is the estimation of r_i which is regulated by soil water availability. Another way to obtain λE estimators is by defining theoretical pixelwise ranges for λE and T_0, and subsequently interpolating by using observed T_0 values.

By substitution of Equations 2.6 and 2.27 in Equation 2.1, the surface-to-air temperature difference is expressed as (Jackson et al., 1988) :

$$T_0 - T_a = \frac{\frac{r_i + r_{ah}}{\rho_a C_p}(Rn - G_0) - \frac{e_0 - e_a}{\gamma}}{1 + \frac{\Delta}{\gamma} + \frac{r_i}{r_{ah}}} \tag{2.28}$$

Based on energy balance and the assumption that the range of $T_0 - T_a$ corresponds with an hypothetical change in evapotranspiration from zero to potential rate at constant surface reflectance and roughness, Menenti and Choudhury (1993) proposed a general form of the Crop Water Stress Index (CWSI) but defined for an arbitrary image pixel. They have named this general form of CWSI as Surface Energy Balance Index (SEBI) in which the surface-to-air temperature differences are normalized by aerodynamic resistances. The SEBI relates to the relative evaporation Λ_r as :

$$\Lambda_r = \frac{\lambda E}{\lambda E_p} = 1 - \frac{\frac{T_0 - T_a}{r_{ah}} - \frac{(T_0 - T_a)_l}{r_{ah,l}}}{\frac{(T_0 - T_a)_u}{r_{ah,u}} - \frac{(T_0 - T_a)_l}{r_{ah,l}}} = 1 - SEBI \tag{2.29}$$

The upper limit of $T_0 - T_a$ (say the dry boundary) can be obtained by taking the limit of Equation 2.28 for $r_i \to \infty$ (no evaporation) while the limit for $r_i \to 0$ (potential evaporation) gives the lower limit (say the wet boundary) :

$$(T_0 - T_a)_u = r_{ah,u} \cdot \frac{R_n - G_0}{\rho_a \cdot C_p} \tag{2.30}$$

$$(T_0 - T_a)_l = \left(r_{ah,l} \cdot \frac{R_n - G_0}{\rho_a \cdot C_p} - \frac{e_0 - e_a}{\gamma} \right) / \left(1 + \frac{\Delta}{\gamma} \right) \tag{2.31}$$

The assumptions behind the SEBI are such that :

- the upper limit (i.e. the dry boundary) of surface-air temperature difference is a virtual temperature difference that would occur if the land surface becomes perfectly dry under the same meteorological and surface structure conditions of the actual case. That is, no water is evaporated from the surface.

- the low limit (i.e. the wet boundary) of surface-air temperature difference is another virtual temperature difference that would attain if the land surface is wet and evaporates at its potential rate under the same meteorological and surface structure conditions as the actual case.

The approach presented above (Equations 2.30 and 2.31) gives the theoretical estimate of the surface-to-air temperature difference that would be observed for a same target (e.g. a pixel) under the same available energy and atmospheric conditions in the two limiting cases of zero and potential evaporation (Figure 2.2). Such way of determining boundary values is independent of satellite image, therefore there is no requirement of existence of "extreme dry" and "extreme wet" pixels in an image of interest.

Menenti and Choudhury (1993) pointed out that in reality near-surface temperature may vary with surface temperature and therefore is not the same under the two limiting cases. They suggested to use meteorological variables at the planetary boundary layer (PBL) height instead, since the PBL air temperature is less affected by the surface and is therefore more homogeneous over large areas.

The flux-profile relationship given by Brutsaert (1982) was applied by Menenti and Choudhury (1993) to calculate aerodynamic resistance between the land surface and the PBL height, in which the roughness length for heat transfer (z_{0h}) was taken as 0.1 of the momentum roughness length (z_{0m}) :

$$r_{ah} = \frac{ln\frac{z-d_0}{z_{0h}} - C_i}{ku_*} \tag{2.32}$$

The C_i function is :

$$C_i = 2ln\frac{1+x^2}{2} \tag{2.33}$$

with $x = (1 - 16\mu_i)^{1/4}$, $\mu_i = z - d_0/L$, L is the Monin-Obukhov constant.
The values of aerodynamic resistance for the limiting cases were treated as :

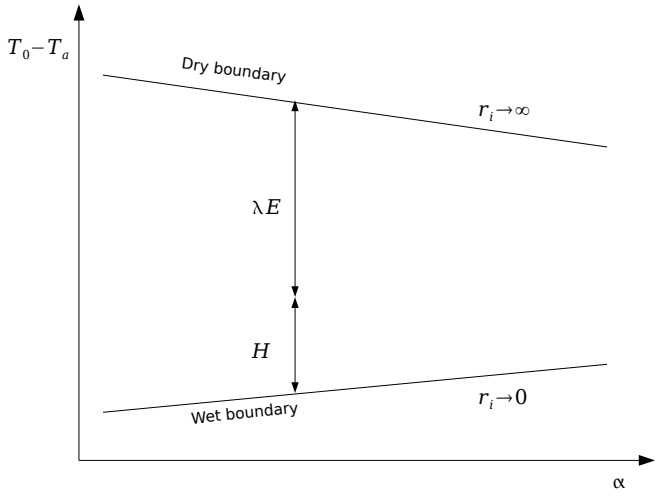

Figure 2.2: The SEBI concept, illustrated in terms of relationship between the land surface albedo and the surface-air temperature difference, from Colin (2006).

- $r_{ah,l} = r_{ah}$ (under neutral condition where $\mu_i = 0$) for potential evaporation, i.e. $C_{i,l} = 0$.

- $r_{ah,u} = r_{ah}$ (under extreme unstable condition where $\mu_i = -150$) for zero evaporation. This is equivalent to $C_{i,u} = 6.4$.

By linking SEBI with evaporative fraction Λ (the ratio between actual evapotranspiration and the available energy), Jia et al. (2001) has extended the SEBI concept to estimate evaporative fraction Λ, sensible and latent heat fluxes. Λ is defined as :

$$\Lambda = \frac{\lambda E}{Rn - G_0} \tag{2.34}$$

Λ is related to SEBI by :

$$\Lambda = \frac{\lambda E}{Rn - G_0} = \frac{\Lambda_r \cdot \lambda E_p}{Rn - G_0} = \frac{(1 - SEBI) \cdot \lambda E_p}{Rn - G_0} \tag{2.35}$$

Sensible and latent heat flux can then be obtained as :

$$H = (1 - \Lambda)(Rn - G_0) \tag{2.36}$$

$$\lambda E = (1 - SEBI) \cdot \lambda E_p \tag{2.37}$$

2.4 The Surface Energy Balance System algorithm

Su (2002) has proposed the Surface Energy Balance System (SEBS) by extending the SEBI concept with a dynamic model for thermal roughness (Su et al., 2001), the Bulk Atmospheric Similarity (BAS) theory of Brutsaert (1999) for PBL scaling and the Monin-Obukhov Atmospheric Surface Layer (ASL) similarity for surface layer scaling. This allows SEBS to be used for both local scaling and regional scaling under all atmospheric stability regimes, providing a link for radiometric measurements and atmospheric models at various scales.

In SEBS, the concept that actual evapotranspiration was regulated by its two extreme limits as used in SEBI is extended to the sensible flux. So, actual sensible heat flux H is constrained in the range set by the sensible heat flux at the wet limit H_w (the low limit in SEBI) and the sensible heat flux at the dry limit H_d (the upper limit in SEBI).

Under the dry-limit, the latent heat flux (or the evapotranspiration) becomes zero due to the limitation of soil moisture and the sensible heat flux is at its maximum value.

$$H_d = Rn - G_0 \tag{2.38}$$

Under the wet-limit, where the evapotranspiration takes place at a potential rate (λE_w), i.e. limited only by the energy available under the given surface and atmospheric conditions, the sensible heat flux takes its minimum value (H_w) :

$$\lambda E_w = Rn - G_0 - H_w \tag{2.39}$$

$$H_w = Rn - G_0 - \lambda E_w \tag{2.40}$$

The relative evaporation Λ_r is defined as the ratio of actual evaporation to its wet extreme as :

$$\Lambda_r = \frac{\lambda E}{\lambda E_w} = 1 - \frac{\lambda E_w - \lambda E}{\lambda E_w} \tag{2.41}$$

and can also be expressed by actual sensible heat flux (Equation 2.6 but using T_{rad} instead of T_{aero}) and its extremes as :

$$\Lambda_r = 1 - \frac{H - H_w}{H_d - H_w} \tag{2.42}$$

which is similar to Equation 2.29 in SEBI. The evaporative fraction is then given by :

$$\Lambda = \frac{\lambda E}{Rn - G_0} = \frac{\Lambda_r \cdot \lambda E_w}{Rn - G_0} \tag{2.43}$$

In Equation 2.43, λE_w is calculated from Equation 2.39 knowing H_w while relative evaporation Λ_r is calculated from Equation 2.42 knowing the actual and the two limiting sensible heat fluxes. By inverting Equation 2.43, the actual latent heat flux λE can be obtained.

SEBS is focused on calculating the actual sensible heat flux and its dry and wet limits. Dry limit of sensible heat flux is easy to estimate from Equation 2.38. As for the wet limit, the internal resistance $r_i = 0$ by definition. The sensible heat flux at the wet-limit is obtained as :

$$H_w = \frac{(Rn - G_0) - \frac{\rho C_p}{r_{ah,w}} \cdot \frac{e_s - e_a}{\gamma}}{1 + \frac{\Delta}{\gamma}} \tag{2.44}$$

the aerodynamic resistance at the wet-limit can be derived as :

$$r_{ah,w} = \frac{1}{ku_*}\left[ln\left(\frac{z - d_0}{z_{0h}}\right) - \psi_h\left(\frac{z - d_0}{L_w}\right) + \psi_h\left(\frac{z_{0h}}{L_w}\right)\right] \tag{2.45}$$

with the wet-limit Monin-Obukhov length as :

$$L_w = -\frac{\rho_a u_*^3}{kg\left(\frac{H_w}{T_0 c_p} + 0.61\frac{Rn - G_0}{\lambda}\right)} \tag{2.46}$$

The major modifications of SEBS over SEBI and the method of Jia et al. (2001) are (Su, 2005) :

- careful treatment in calculating sensible heat flux in the low limit as described above.

- use of Brutsaert (1999) stability functions to distinguish the interactions between land surface and the near-surface atmosphere and between land surface and the PBL. When meteorological variables at a reference height within the near-surface layer are available, SEBS uses the Monin-Obukhov Similarity (MOS) stability correction functions for momentum and sensible heat transfer. While for the case that meteorological variables at the PBL height are available, the Bulk Atmospheric Similarity (BAS) theory (Brutsaert, 1999) is used to link the surface to the atmospheric conditions at the PBL height. In both cases, the calculation is done for each pixel.

However, as indicated by Gowda et al. (2007), a potential weakness in the SEBS approach is the neglect of heat flux absorption along the temperature profile when extrapolating to and from the atmospheric reference level. The absorption over a dry surface can be large, and it disrupts the assumption of a smooth temperature gradient that conveys the sensible heat flux all the way to the reference height. This results in an overestimation of the surface temperature for the dry condition and must be accounted for somehow empirically. A further study is perhaps necessary to understand the appropriateness and conditions of using BAS theory in regional scale calculation.

Besides, though the concept of using the ASL similarity for surface layer scaling and the BAS for regional scaling proposed in SEBS, the corresponding scales are not defined by SEBS. Taking a simple ratio between the PBL reference height h and the corresponding horizontal scale L_{hori}, i.e. h/L_{hori} = 10-100, Jia et al. (2003b) have coupled model forecast fields at 25 km grid size from a large scale Numerical Weather Prediction Model (NWPM) to radiometric measurements at 1km pixel size from the Along Track Scanning Radiometer (ATSR2) onboard the European Remote Sensing Satellite (ERS-2). An improvement on resistance parameterization when using BAS in combination of PBL variables was developed in a later study by Colin et al. (2006), in which a multiple scale scheme was developed to link the PBL height to a proper horizontal scale when calculating the resistance using BAS theory.

A critical improvement in SEBS is the use of a dynamic model for thermal roughness length calculation adapted from Massman (1999) (Su et al., 2001; Su, 2002). In this model, the dimensionless kB^{-1} parameter is expressed as a function of surface conditions and of aerodynamic parameters :

$$kB^{-1} = \frac{kc_d}{4C_t \frac{u_*}{u(h_v)}(1-e^{-n/2})} f_c^2 + \frac{k\frac{u_*}{u(h_v)}\frac{z_{0m}}{h_v}}{C_t^*} 2f_c f_s + kB_s^{-1} f_s^2 \qquad (2.47)$$

where C_d is the drag coefficient of the foliage elements and is set to 0.2, f_c is the fractional vegetation coverage and f_s is its complement, C_t is the heat transfer coefficient of the leaf ranging in $0.005N \leq C_t \leq 0.0074N$ (N is number of sides of a leaf to participate in heat exchange), n is the windspeed extinction coefficient within the canopy, h_v the vegetation height, C_t^* the heat transfer coefficient of the soil and is given by $C_t^* = Pr^{-2/3}Re_*^{-1/2}$, where Pr is the Prandtl number : 0.71 (Massman, 1999) and the roughness Reynolds number $Re^{-1/2} = h_s u_*/\nu$, with h_s the roughness height of the soil, kB_s^{-1} is the value of kB^{-1} for bare soil surface (Brutsaert, 1982).

The three terms on the right hand side of Equation 2.47 represent the contributions of canopy only, canopy-soil interaction and soil only, respectively. Actually,

both the structure and the conditions of the canopy may affect the thermodynamic properties of the composite surface. This is the reason why in the parameterization of kB^{-1} surface properties such as fractional vegetation cover, leaf area index and the height of the canopy must be taken into account.

2.5 Conclusion

Physically based algorithms such as SEBS have a better physical basis and all the variables are calculated analytically though still some empirical relationships are used. When proper relations for heat and mass exchanges suitable at different scales are used, this model can be applied to any spatial scales. The disadvantage is that it needs numerous inputs and detailed canopy structure information : SEBS includes remote sensing data-based land surface parameters and ground-based meteorological measurements, such as land surface temperature, LAI, fractional vegetation cover, albedo, wind speed, humidity and air temperature. Meteorological forcing over regional scale can only be obtained from other sources, for instance from numerical forecast model outputs.

A single-source model such as SEBS is the most simplified way to represent heat transfer of an heterogeneous land surface. However, The radiometric temperature is not equivalent to the aerodynamic surface temperature which is actually needed in the single-source model, and it depends on the observation angle. A single-source model may still be useful if an appropriate parameterization of the aerodynamic resistance can be established to represent the thermal heterogeneity of soil-vegetation canopies. This can be achieved by a proper characterization of surface roughness lengths for momentum and heat transfer.

As mentioned earlier, Jia et al. (2003b) applied SEBS using remote sensing data from ATSR and ground data from a NWPM and validated the estimated sensible heat flux with Large Aperture Scintillometers (LAS) located at three sites in Spain. Also, with the surface meteorology derived from the Eta Data Assimilation System, Wood et al. (2003) applied SEBS to the Southern Great Plains region of the United States. Derived latent heat fluxes were compared with the measurements and results indicated that SEBS approach had promise in estimating surface heat flux from space. SEBS has been used to estimate daily, monthly, and annual evapotranspiration in a semi-arid environment (Su et al., 2003). Su (2002) showed that SEBS could be used for both local and regional scaling under all atmospheric stability regimes. More recently, results from Su et al. (2005) have shown that accuracy of evapotranspiration value estimated from SEBS could reach 10-15% of that in-situ measurements.

Chapter 3

Study areas and materials

3.1 Introduction

In this chapter, study areas and observations are presented. In the frame of the Dragon 2 programme, WATER and CEOP-AEGIS projects, several study areas are located in China. Because of the synergy between WATER project and Dragon 2 programme, an intensive observation period took place over the Heihe River basin. Two experimental sites with in particular surface radiative and energy balance measurements are used in this work (Li et al., 2009b). The CEOP-AEGIS project focus on the Tibetan Plateau. Surface radiative and energy balance observations were also conducted at four key stations (Babel et al., 2011). For each region of interest, ground measurements are also completed with spaceborne or airborne remote sensing observations. These observations allows to retrieve land surface parameters at various spatial resolution. Atmospheric parameters are also simulated at a larger scale over these areas by the mean of Numerical Weather Prediction Models (NWPM).

3.2 Study areas

The two main study areas are presented in this section. The first one is the Heihe river basin and particularly the Yingke Oasis, center of interest of the WATER and Dragon 2 projects. The second area is the Qinghai-Tibet Plateau, which is observed and modeled within the CEOP-AEGIS project.

3.2.1 Heihe river basin

The Heihe river basin is a typical inland river basin in the northwest of China (Figure 3.1). Second largest inland river basin of the country, it is located be-

tween 97°24' - 102°10' E and 37°41' - 42°42' N, and covers an area of approximately 130 000 km^2. Experiments conducted in the scope of the WATER project consisted in simultaneous airborne, satellite-borne and ground-based remote sensing measurements aiming at improving the observability, understanding and predictability of hydrological and ecological processes at catchment scale (Li et al., 2009b). Observations focused on six different areas with landscapes ranging from desert steppe and Gobi desert to grassland and irrigated farmland. Two stations located in two different areas are used in this study.

Figure 3.1: Location map of the Heihe river basin in China.

Yingke oasis station

The Yingke oasis, located to the south of the Zhangye city (100°25' E, 38°51' N, 1519 meters a.s.l.), is a typical irrigated farmland (Figure 3.2). The primary crops are maize and wheat, with fields often separated by tree rows. This site was selected for its interest in investigating crop evapotranspiration, bio-geophysical and structure parameters of crops, interaction between groundwater and surface water, and irrigation.

A'rou sation

A'rou station is located in the middle reaches of the Babao river basin (100°27' E, 38°03' N) and is a relatively flat area with a mean elevation of about 3000 m (Figure 3.2).

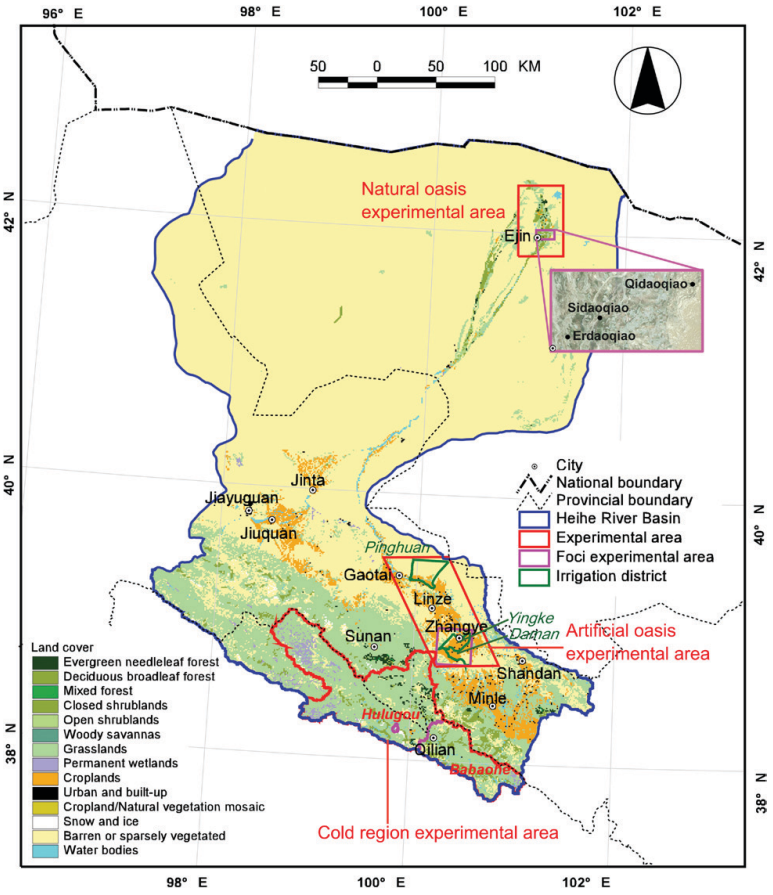

Figure 3.2: A detailed view of the Heihe river basin and the study areas, from Li et al. (2013). Yingke oasis station is located in the *artificial oasis experimental area*, and A'rou station is located in the *cold region experimental area*.

3.2.2 Tibetan Plateau

The Tibetan Plateau covers a surface of 2.5 million square kilometers with average altitude higher than 4,700 meters. It is the headwater of rivers that flow down to 47% of the Earth's population living under the influence of the monsoon system (Figure 3.3). The Yellow River and the Yangtze start in northeastern Tibet and flow across China; the Mekong originates in eastern Tibet as do the Irrawady and Salween that traverse down to Burma. The Yarlung Tsang Po starts near Lake Manasarovar and travels eastwards for nearly 2,000 km before cutting through the Himalayas to become the Brahmaputra and flowing to the Bay of Bengal. Most of the major rivers in Nepal originate in the Tibetan plateau and cut deep gorges to flow down to the Ganga. Then there are the Indus and its tributaries that also start near Lake Manasarovar and flow westwards into Pakistan and to the Arabian Sea.

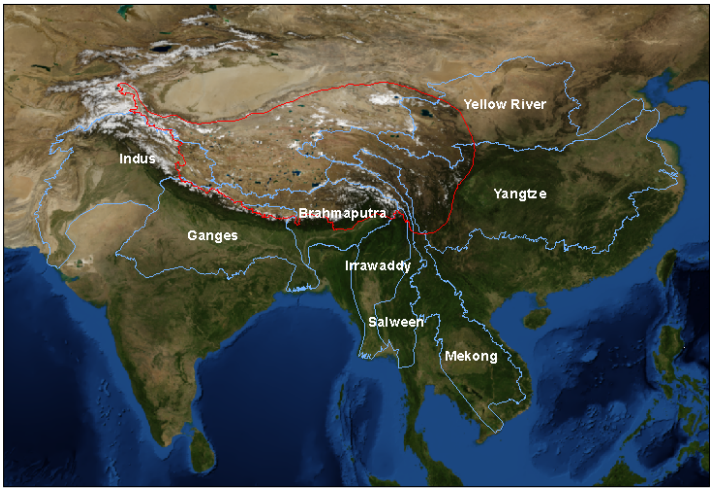

Figure 3.3: Localization of Tibetan Plateau and the related major watersheds.

Ground measurements of surface radiative and energy balance have been performed at four sites (Babel et al., 2011) : Nagqu, Linzhi, Namco and Qomolangma stations.

Nagqu station

The Nagqu station (31°22'N 91°53'E, 200 km north of Lhasa) at 4,502 m a.s.l. lies in almost flat terrain within a huge valley. The vegetation, a slightly degraded Kobresia pasture, is very low and sometimes interspersed with bare soil, but quite homogeneous at the landscape scale. The nearest hill slopes of the valley occur at approximately 1km NE of the station, with a small creek accompanied by wetland vegetation at the base point. The hill slopes in South and West direction were several tens of kilometers apart.

Linzhi station

Linzhi station (29°45'N, 94°44'E) at 3,327 m a.s.l. is located directly at the mouth of a small valley, inclined West-East into a larger valley, oriented from South to North. The surface of the station area is covered by an alpine meadow with tall grasses and herbs during the summer period, while the meadows outside are grazed intensively and thus very short. The landscape is very heterogeneous with steep slopes, covered by mixed forest in North and South direction at a distance of 150 m to the tower with the Eddy Covariance (EC) sensor. The pastures outside the fence alternate with a small creek and bushes and sparse trees.

Namco station

Namco station (30°46'N, 90°57'E) at 4,730 m a.s.l. lies in the south-eastern of the Northern Tibetan Plateau. It is located at 1km distance SE of Namco Lake, which is the second largest saline lake in the Tibetan Plateau. The Namco basin is enclosed by several mountain ranges, the most prominent being Nyenchentanglha mountain in the South, oriented WSW-ENE and peaking at 5,700 m a.s.l. near the station with its highest summit beyond 7,000 m. There is a small inner lake located 260 m NNW of the site with a station building located 90 m West, a 52 m profile tower and a container for trace gas measurements located 40 m and 80 m NE, respectively. The measurement site itself is located within flat terrain, and a gentle slope in NNW direction leads to the shoreline of the inner lake. The typical vegetation around the station is alpine steppe.

Qomolangma station

The Qomolangma (Everest) station (28°21'N, 86°56'E) at 4,293 m a.s.l. is located in a valley inclined from South to North. Its river is spring-fed by the Rongbuk glacier North of the Mount Everest summit. It is enclosed by steep slopes at a distance of 750 m E and 500 m NW and SW of the tower, while a side valley comes in from West. The crests along the valleys slopes display a height of 600-800 m above ground level. The valley is dominated by riverbed gravel, with very sparse vegetation, but also small patches of short alpine meadows and cropland (barley) occur around the nearby village.

3.3 Meteorological data

3.3.1 Ground measurements

The Yingke Oasis experimental site and A'rou station are permanently instrumented with an Automatic Meteorological Station (AMS). The stations record every ten minutes air temperature, wind speed and direction at 2 and 10 meters, air pressure, relative humidity, precipitation, net radiation, soil heat flux, soil temperature and water content. Moreover, latent heat flux, sensible heat flux and water vapor concentration are obtained from Eddy Covariance (EC) systems with an integration step of 30 minutes. Six atmospheric soundings were performed at the Yingke station during June and July 2008 with GPS-tracking balloons. The instruments onboard have measured air temperature, relative humidity, air pressure, wind horizontal component and direction, mixing ratio and informations about localization, altitude and attitude.

Surface observation of heat fluxes by EC systems captures fluxes originating from a limited source area, which depends on the observation height, atmospheric and surface conditions. The source area has to be properly located and delineated when comparing pixel-based remote sensing estimates of heat fluxes with ground measurements. The concept of footprint or source weight function is used as the contribution, per unit surface flux, of each unit element of the upwind surface area to a measured vertical flux (Schuepp et al., 1990). Wind direction, atmospheric stability, measurement height, and roughness length can be used to define the footprint location and delineation. The area contributing to ground flux observations at a specific location can be defined as the footprint of the measurement, and the various relative contributions to flux measurement within the source area can also be calculated.

Finally, the EC (or LAS) footprints applying to actual conditions can be employed in validating the sensible heat fluxes estimated with multispectral satellite data over a range of spatial resolutions. The results show that footprint modeling is necessary when validating surface heat fluxes estimated with high spatial resolution remote sensing data over heterogeneous surface. Details about the footprint model applied to the EC measurements performed at the Yingke station are given by Colin et al. (2011).

The four observation stations located through the Tibetan Plateau are also instrumented for surface radiative and energy balance with the same set of sensors. Measurements are also integrated over 30 minutes. The turbulent heat fluxes are released after correction for energy balance closure. All details concerning sensors, acquisitions, data processing and footprint model were reported by Babel et al. (2011) and Babel et al. (2012).

3.3.2 Numerical Weather Prediction Models

The properties of the atmosphere at the surface level and at the top of the PBL required for SEBS algorithm are air temperature, specific humidity, air pressure, and wind speed (Table 3.1). These variables are usually derived from local radiosoundings. Because of the natural integrator behavior of the PBL, a single radiosounding can be considered representative of an area as large as around ten times the PBL height upstream, which can be suitable for a local-scale study, but not enough to cover an area like the Tibetan Plateau or even the Heihe river basin. Therefore in this context it is required to use Numerical Weather Prediction Model gridded outputs. These models are also able to produce surface heat fluxes, but the output spatial resolution is too coarse for detailed hydrological studies. Moreover, the parameterization of aerodynamic roughness is usually approximative and rely on look-up tables following the land-cover type.

Table 3.1: Variables extracted from NWPM simulations.

Variable	Description
PBL_h	PBL height (m)
T_{pbl}	Air temperature at the PBL level (K)
q_{pbl}	Specific humidity at the PBL level (kg/kg)
u_{pbl}	u wind at the PBL level (m/s)
v_{pbl}	v wind at the PBL level (m/s)
P_{pbl}	Pressure at the PBL level (Pa)
q_2	Specific humidity at 2 meters (kg/kg)
P_s	Surface pressure (Pa)
P_{sl}	Sea level pressure (Pa)
$L_w \downarrow$	Longwave incoming radiation (W/m^{-2})
$S_w \downarrow$	Shortwave incoming radiation (W/m^{-2})

GRAPES-Meso

The Chinese Meteorological Administration (CMA) has established in the year 2000 the National Innovative Base for Meteorological Numerical Prediction at the Chinese Academy of Meteorological Sciences (CAMS), to work on developing a new generation of Numerical Weather Prediction Models. The result of this effort is the Global/Regional Assimilation and PrEdiction System GRAPES, used for both operational and research purposes (Zhang and Shen, 2008; Chen et al., 2008). The GRAPES model is designed for hydrostatic or non-hydrostatic, global or regional simulation, and include advanced data assimilation algorithms for standard meteorological observations, but also satellite based observation of surface and clouds, and Doppler weather radars (Zhuang et al., 2005; Zhu et al., 2008; Xue et al., 2008). The highly flexible design of GRAPES allows to build several sub-system for specific purposes, like GRAPES-Meso for meso-scale simulations, GRAPES-TCM for typhoon forecast, GRAPES-SDM for sand storm predictions, or the GRAPES Lightning forecast model. The GRAPES-Meso, put in operation in 2006, provides analysis and forecast products at a resolution of 30 kilometers, and proved to give even better results at a resolution of 15 kilometers. Although analysis products are available with a 6-hours time interval and simulations can be performed at a very fine time resolution, typically 30 minutes. Variables like air temperature, specific humidity, wind u and v components are given at barometric levels.

WRF-ARW

The Advanced Research WRF (ARW) modeling system has been in development for the past few years. The current release is Version 3, available since April 2008 (Skamarock et al., 2008). The ARW is designed to be a flexible, state-of-the-art atmospheric simulation system that is portable and efficient on available parallel computing platforms. The ARW is suitable for use in a broad range of applications across scales ranging from meters to thousands of kilometers. The Mesoscale and Microscale Meteorology Division of NCAR is currently maintaining and supporting a subset of the overall WRF code (Version 3.2 released in April 2010). The WRF modeling system software is in the public domain and is freely available for community use. WRF-ARW model is used in this study as a tool for generating atmospheric fields at PBL level. The simulation area is focused on the N-E part of the Tibetan Plateau and precisely the Heihe River basin, where GRAPES data are affected by edge effects due to the limits of the domain extent. Efforts has been conducted to improve the input surface data and to define the choice of physical models that better reproduce in-situ measurements.

3.4 Remote sensing data

3.4.1 Airborne VNIR & TIR sensor

The Wide-Angle Dual-mode Line/Area Array Scanner (WiDAS) is composed of two thermal imagers and four CCD cameras (Li et al., 2009b). The thermal imager has two bands (3.5-5 and 8-12 μm) with an array of 320 per 240 pixels, an 80° total field of view (FOV) divided into seven observation angles: +40°, +30°, +20°, 0°, -20°, -30°, -40° (+ as forward, - as backward). The CCD camera has four bands (centered at 550, 650, 700 and 750 nm), a detector array of 1392 per 1040 pixels, a 60° total field of view and five observation angles: +30°, +20°, 0°, -20°, -30°.

Brightness temperature of land surface is provided by the radiance measured in the 8-12 μm channel after atmospheric correction. Radiances for visible and thermal infrared domains are both corrected using MODTRAN4 (Li et al., 2009a). Spectral reflectances are used to derive land surface properties (Section 5.2.1).

3.4.2 Airborne LIDAR

The WATER field campaign included an intensive observation period. Twenty-five missions were flown in 2008 with different sensors. We used the data collected by a LiteMapper 5600 imaging LIDAR, whose major characteristics are a wavelength of 1550 nm, a pulse of 3.5 ns at 100 kHz and a scan angle range of $\pm$ 22.5°. The spatial density for a flight height of 800 m above the ground

is 4 impacts per square meter. After correction of the raw data to account for the attitude of the plane and for the precise location of the sensor, each return signal can be translated into an accurate 3D georeferenced point. The resulting point cloud is then processed to extract the minimum and maximum elevation from the points in each square meter grid. The lowest elevation point is used to derive the elevation of the ground. After removing local aberrations, the resulting map is a Digital Elevation Model (DEM), expressed in terms of altitude above mean sea level (a.m.s.l), in meters. If the surface is a solid block, or a bare soil, the minimum and maximum elevation values are equivalent. However, for sparse vegetation structures, the difference between the lowest and highest elevations reflects the height of the vegetation canopy. Therefore, it is possible to separate the land surface topography, represented by the DEM, from the elevation of the top of the vegetation canopy. The latter is called the Digital Surface Model (DSM), and is also expressed in terms of altitude a.m.s.l. Both digital models have a spatial resolution of 1 meter. The LIDAR flight was operated the 20^{th} june 2008, and the scene covers an area of 7.2 km^2 (Figure 3.4).

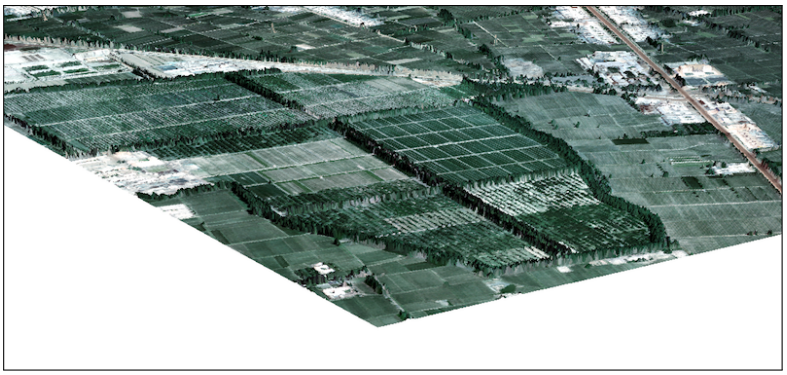

Figure 3.4: Example of 3-D rendering of the South-West part of the Yingke area obtained by combination of the LIDAR Digital Surface Model and the high resolution image simultaneously acquired by the CCD camera installed together with the LiteMapper 5600.

3.4.3 Land surface variables

The existing Earth Observation (EO) sensors constellation now offer a very significant amount of images of medium to high spatial and spectral resolution. Some sensors designed for environmental purposes are particularly well suited for regional to continental monitoring of surface conditions, and algorithms to derive surface properties from spectral data are now mature enough to provide end users with detailed information.

The first set of EO products needed to compute surface net radiation is composed of the surface albedo, brightness temperature and emissivity. Basic information about vegetation can be obtained through the use of NDVI. The latter can actually be used to estimate many surface properties related to vegetation cover with help of commonly used relations, e.g. to obtain the Land Surface Emissivity (LSE), the surface fractional vegetation cover (f_c), the Leaf Area Index (LAI).

Therefore the very minimum data requirement for algorithms like SEBS include albedo, Land Surface Temperature (LST) and NDVI. However, such kind of empirical relations are usually extensively used, including for surface conditions which were explicitly excluded by the authors. Therefore it is recommended to use sensor specific algorithms, or when already available, sensor specific products.

For an example, Table 3.2 presents the list of products used in this study. NDVI products (MOD13A2) are freely delivered by NASA and cover a time period of 16 days with a spatial resolution of 1 km^2. Albedo, f_c and LAI are enhanced kilometric products delivered in the frame of the CEOP-AEGIS project. They are based on MODIS reflectance product (MOD09) and also on MERIS land cover product for the fractional vegetation cover (Yan et al., 2011b,a). Digital Elevation Model (DEM) is provided by the global raster 30 arc-second SRTM. The LST and LSE were retrieved from radiometric data collected by the Chinese geostationary satellites Feng-Yun 2 series, with a spatial resolution of 5 km by 5 km. The LST data were generated in the frame of the CEOP-AEGIS project in order to obtain a complete gap-filled time-serie from 2008 to 2010 (Tang and Li, 2011; Ghafarian et al., 2012).

Table 3.2: Summary of the land surface variables required for SEBS, and the respective remote sensing source data following the scale considered.

Variables	Local scale	Regional scale
LST	WiDAS	FY-2 series / AATSR
LSE	WiDAS	FY-2 series / MODIS
Albedo	WiDAS	MODIS
NDVI	WiDAS	MODIS / AATSR
LAI	WiDAS	MODIS
f_c	WiDAS	MODIS + MERIS LC
DEM	LiteMapper	SRTM30 / ASTER GDEM
DSM	LiteMapper	-

A specific detailed study used land surface temperature and NDVI observed with ENVISAT/AATSR. The ATS_NR_2P product is delivered by the European

Space Agency (ESA). The AATSR dual-view (nadir and forward) top-of-atmosphere (TOA) brightness temperatures and reflectances (ATS_TOA_1P product) are also required. In order to match with the kilometric resolution of these datasets, the Terra/MODIS 8-day land surface emissivity (MOD11A2) delivered by NASA is chosen.

3.4.4 Land Surface Temperature time-serie

The hourly LST and LSE were retrieved from FY-2C/2E satellite data for the Tibetan Plateau region, with a spatial resolution of 5 km x 5 km and for the period from January 1^{st} 2008 through December 31^{st} 2010 (Tang et al., 2008; Tang and Li, 2011). The hourly LST time-series were gap-filled by Ghafarian et al. (2012) with the Multi-channel Singular Spectrum Analysis. Time series of LST often feature missing data or data with anomalous values due to cloud coverage, malfunction of sensor, atmospheric aerosols, defective cloud masking and retrieval algorithms (Figure 3.5).

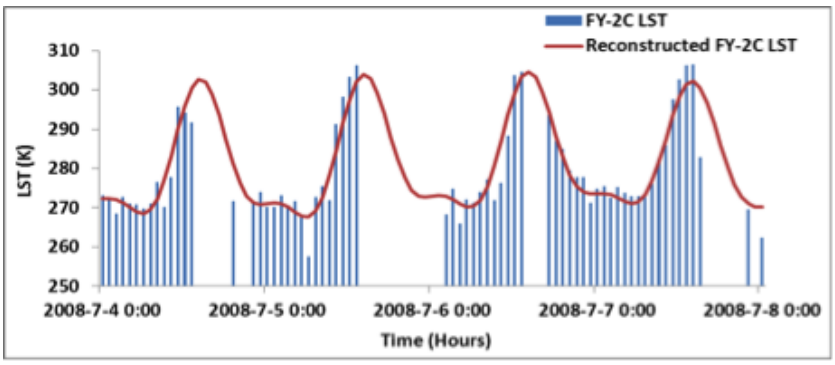

Figure 3.5: Example of LST gap-filling from the 4^{th} to the 8^{th} July 2008 for a FY-2 pixel located over the Tibetan Plateau (Jia et al., 2012a).

Preprocessing procedures are needed to identify anomalous observations resulting in gaps and outliers and then reconstruct the time-series by filling the gaps. The Singular Spectrum Analysis (SSA) was used for a single time-serie, and the Multi-channel (M-SSA) for multiple time-series. This is considered as an advanced methodology which uses both temporal (SSA) and spatio-temporal (M-SSA) correlation to fill the gaps, especially for continuous gaps in time-series data.

In a dynamic system (e.g. diurnal variation of LST), individual pixel values in time, represent the outcome of the interaction among all radiative and turbulent energy exchange processes. Therefore, the evolution of whole records in time of-

ten have both regular (cycles) and irregular (noise) components. Using this idea, this method uses Empirical Orthogonal Functions (EOFs) to extract information from short and noisy time series without initial knowledge of the dynamic processes affecting the underlying time series. As in many time series data, a few leading components capture most variance in data sets while the rest is considered as noise. The results indicated with 63% of hourly gaps in the time series, the Mean Absolute Error (MAE) reached 2.25 Kelvin (K) with r^2 = 0.83.

3.5 Conclusion

Through the three scientific projects, all the available data (measured, retrieved or simulated) cover a wide range of spatial and temporal resolutions, from a point to a sub-continent, for both meteorological and remote sensed variables. At the scale of the Tibetan Plateau, all meteorological and land surface parameters are provided as final products. However, at the local scale remote sensing data have to be processed for land surface parameters retrieval and require the selection of proper algorithms. At the scale of the Heihe river basin, meteorological observations (ground based or radiosoundings) are unidimensional and cannot be used at a large scale. However, they can be useful for the simulation of spatialized atmospheric variables.

Chapter 4

Investigations on roughness length retrieval

4.1 Introduction

Roughness length of land surfaces is an essential variable for the parameterization of momentum and heat exchanges. The growing interest in the estimation of the surface energy balance components from passive remote sensing leads to an increasing development of models, e.g. Bastiaanssen et al. (1998); Roerink et al. (2000); Su (2002); Colin (2006), some of which propose detailed parameterization of resistances to heat transfer using advanced algorithms to retrieve roughness length for heat ($z_{0\mathrm{h}}$) from kB^{-1} formulations (Massman, 1999; Blumel, 1999). However, as complex as the parameterization can be, the actual benefit from such formulations depends on an adequate estimate of the roughness length for momentum ($z_{0\mathrm{m}}$).

Numerous formulations to derive this parameter from NDVI can be found in many studies e.g. Moran (1990); Bastiaanssen (1995), but are commonly used out of recommended bounds and on highly heterogeneous land surfaces, sometimes leading to a significant degradation of turbulent flux estimates (Colin et al., 2006). These approaches would benefit from the combined use of passive remote sensing and land surface structure measurements from Light Detection And Ranging (LIDAR) techniques. Since the very early use of laser altimetry (Ketchum Jr., 1971), sensor performances have significantly improved, allowing airborne profiler to be used to derive the roughness of the surface (Menenti and Ritchie, 1994; Menenti et al., 1996; De Vries et al., 2003). More recently, satellite and airborne imaging LIDAR systems have paved the way to the mapping of vegetation properties over forest areas (Hofton et al., 2002), sometimes associated with complex topography (Dorren et al., 2007), but also on low vegetation like in salt-marshes (Wang et al.,

2009) or semi-arid steppes (Streutker and Glenn, 2006).

The objective here is to explore the use of imaging LIDAR measurements acquired over the Yingke oasis station (Heihe river basin) in the frame of the WATER project, to estimate the aerodynamic roughness length over a heterogeneous landscape. LIDAR points were used to extract a Digital Surface Model (DSM) and a Digital Elevation Model (DEM) from a seamless mosaic of three flight passes over an irrigated area covered by field crops, small trees arrays and tree rows, with a ground resolution of 1 m and a total coverage of 7.2 km^2 (see paragraph 3.4.2). As a first step, the DSM is used to estimate the plan surface density and frontal surface density of obstacles to wind flow and to compute a displacement height and roughness length following the work done by Raupach (1994) and MacDonald et al. (1998). In a second step, both the DSM and DEM are introduced in a Computational Fluid Dynamics model (CFD) to calculate wind fields from the surface to the top of the Planetary Boundary Layer (PBL), and invert wind profiles for each calculation grid and compute a roughness length. Examples of the use of these three approaches are presented for various wind directions together with a comparison of results on heterogeneous land cover and complex roughness element structures.

4.2 Theoretical background

The wind velocity profile over the land surface with a neutral atmospheric stratification is a simple logarithmic expression of the form :

$$u_{(z)} = \frac{u_*}{k} \cdot \ln\left(\frac{z - d_0}{z_{0\mathrm{m}}}\right) \tag{4.1}$$

where u_* is the friction velocity (m/s), k the von Karman constant, d_0 the displacement height (m) and $z_{0\mathrm{m}}$ the aerodynamic roughness length (m).

The latter is usually expressed as a constant ratio of the canopy height for homogeneous surfaces like continuous low vegetation canopies, with a consensus for values of around $z_{0\mathrm{m}}/h_{\mathrm{v}} \approx 0.1$ (Brutsaert, 1982). However, the homogeneity assumption is generally never met. Therefore, such kind of approximation is of limited interest for most environmental studies.

Geometry of canopy to parameterize aerodynamic roughness

It has long been demonstrated from field work and wind tunnel experiments that the drag affecting the airflow over a heterogeneous land surface is related to roughness elements density and size (Counehan, 1971; Wooding et al., 1973). This was expressed in the formulation proposed by Lettau (1969) :

$$z_{0\mathrm{m}} = 0.5 \cdot h \cdot \lambda_{\mathrm{f}} \tag{4.2}$$

where h is an effective averaged obstacle height, and λ_{f} the frontal area index defined as :

$$\lambda_{\mathrm{f}} = \frac{A_{\mathrm{f}}}{A_{\mathrm{T}}} \tag{4.3}$$

The frontal area index expresses the ratio of the frontal area A_{f} (perpendicular to the flow) over the total area covered by roughness elements A_{T}. A well-known formulation based on the combined use of h and λ_{f} was proposed by Raupach (1994) to calculate the displacement height d_0 and the roughness length $z_{0\mathrm{m}}$. Raupach's formulation of the displacement height is :

$$\frac{d_0}{h_{\mathrm{v}}} = 1 - \frac{1 - \exp\left[-\left(C_{\mathrm{dl}} 2\lambda_{\mathrm{f}}\right)^{0.5}\right]}{\left(C_{\mathrm{dl}} 2\lambda_{\mathrm{f}}\right)^{0.5}} \tag{4.4}$$

and the formulation of the roughness length is :

$$\frac{z_{0\mathrm{m}}}{h_{\mathrm{v}}} = \left(1 - \frac{d_0}{h_{\mathrm{v}}}\right) \cdot \exp\left(-k\frac{U}{u_*} + \psi_{\mathrm{h}}\right) \tag{4.5}$$

with

$$\frac{u_*}{U} = \min\left[\left(C_{\mathrm{s}} + C_{\mathrm{R}}\lambda_{\mathrm{f}}\right)^{0.5}; \left(\frac{u_*}{U}\right)_{\max}\right] \tag{4.6}$$

where ψ_h expresses the influence of the roughness sublayer, C_{s} is the drag coefficient for an obstacle free surface, C_{R} the drag coefficient for an isolated obstacle, and C_{dl} a free parameter (Raupach, 1994). In this study, we used values recommended by Raupach, i.e. the values of $\psi_{\mathrm{h}} = 0.193$, $C_{\mathrm{s}} = 0.003$, $C_{\mathrm{R}} = 0.3$, $C_{\mathrm{dl}} = 7.5$ and $(u_*/U)_{\max} = 0.3$.

These analytic expressions of the displacement height and of the roughness length normalized by the averaged obstacle height were derived from numerous field and wind tunnel experiments, and gave a good fit with experimental data (Raupach, 1994).

Theurer (1993), quoted by MacDonald et al. (1998), noted that $z_{0\mathrm{m}}$ and d_0 could be estimated by combining the frontal area index with the plan area index defined as :

$$\lambda_{\mathrm{p}} = \frac{A_{\mathrm{p}}}{A_{\mathrm{T}}} \tag{4.7}$$

where A_{p} is the plan area of the roughness elements within the same total area A_{T}. The plan area index λ_{p} is related to the intervening spaces between roughness

elements. For an array of roughness elements of equivalent height, an increase of the plan area index will lead to an increase of the displacement height, and a decrease of the roughness of the obstacle array. When the plan area index tends to 1, the top elements of the obstacles, forming an obstacle canopy, tend to form a homogeneous surface with a very limited resistance to airflow. This explains the non-monotonic dependence of $z_{0\mathrm{m}}$ on λ_{f}. For a given value of the frontal area index, an increase of λ_{p} leads to a decrease of the drag effect of the roughness elements. Therefore the Lettau's formulation of $z_{0\mathrm{m}}$ is known to fail for plan area index values higher than 0.2–0.3 because of mutual effects of high frontal area index and limited intervening spaces (MacDonald et al., 1998).

This was expressed by MacDonald et al. (1998), who proposed formulations for $z_{0\mathrm{m}}$ and d_0 based on Lettau's concept to account for a larger variety of geometrical configurations of roughness elements, and show an appropriate behaviour over the entire range of density indexes. The ratio of the displacement height over the roughness element height is expressed as :

$$\frac{d_0}{h_{\mathrm{v}}} = 1 + \alpha^{-\lambda_{\mathrm{p}}} \left(\lambda_{\mathrm{p}} - 1\right) \tag{4.8}$$

The convexity can be controlled by α. Experiments led to recommend a value $\alpha = 4.43$ for staggered arrays of roughness elements and $\alpha = 3.59$ for squared arrays (MacDonald et al., 1998). This ratio is then incorporated in the calculation of the ratio of the roughness length over the roughness element height following :

$$\frac{z_{0\mathrm{m}}}{h_{\mathrm{v}}} = \left(1 - \frac{d_0}{h_{\mathrm{v}}}\right) \exp\left[-\left(0.5\beta \frac{C_{\mathrm{D}}}{k^2}\left(1 - \frac{d_0}{h_{\mathrm{v}}}\right)\lambda_{\mathrm{f}}\right)^{-0.5}\right] \tag{4.9}$$

The expression includes the obstacle drag coefficient $C_{\mathrm{D}} = 1.2$, and an extra β coefficient to best fit the experimental data. In this study $\beta = 1$. This formulation reproduces the peak value of $z_{0\mathrm{m}}/h_{\mathrm{v}}$ for $\lambda_{\mathrm{f}} = 0.15$–$0.30$, which is consistent with wind tunnel experiments.

Modeling air flow

Beside the use of the plan area and frontal area indexes, the direct use of both the DEM and DSM in a Computational Fluid Dynamics (CFD) solver is explored. The CFD solver called Canyon, embedded in the WindStation software (Lopes, 2003), allows for numerical simulations of turbulent flows over complex topography, and can account for the geometry of surface roughness elements through the Digital Surface Model, as obtained from LIDAR data. The solver follows a control-volume approach, and solves for mass conservation, momentum conservation following Navier-Stokes equations, and also energy conservation for

non-neutral situations. 3D wind fields obtained by CFD modeling express the combined effect of topography and roughness elements on the airflow, and result from the solution of the transport equation. Values of wind speed of a given profile not only characterize local effects of the vegetation structure, but the total surface stress resulting from the upstream roughness elements on a distance called the length scale (Menenti and Ritchie, 1994). This length scale is usually considered to be of 1-2 order of magnitude of the height of the measurement of the wind speed. Therefore an aerodynamic roughness length can be obtained from the wind profile of each computation grid by inverting Equation 4.1 with values within the ground and a given elevation. As mentioned earlier, this is only true under neutral atmospheric stability conditions.

4.3 Design of the experiment

4.3.1 Implementation of the approach from MacDonald et al. (1998)

The canopy height obtained by difference between the DSM and DEM gives the distribution of roughness elements over the entire area (Figure 4.1). Considering a subset grid of this area with an area A_{T}, and the total area of roughness elements A_{p} within this subset, it is possible to compute a plan area index for the grid. The separation of pixels between roughness elements and intervening space was performed by estimating a height threshold from the vertical distribution of pixels. It should be noted that a $\Delta h \approx 0$ within a LIDAR grid can either mean that there is no vegetation within this grid, or that the canopy is homogeneous and dense enough to prevent impulses to reach the soil underneath. However, in both cases it was considered that such grids belong to intervening spaces in between bigger roughness elements. In the following calculations, the threshold was estimated as 12 cm. In the same way, pixels in the same subset grid of area A_{T} can be projected on a plan surface orthogonal to the airflow, giving a total integrated frontal area A_{f} to compute the frontal area index.

We developed a specific tool for these purposes. Considering a given grid size, a number of wind direction (2, 4, 8...) and an input pixel size, the tool will sequentially compute the plan area index, the frontal area indexes for each wind directions, and the associated displacement heights and roughness lengths following the two formulations of Raupach (1994) and MacDonald et al. (1998). The tool can optionally generate views of frontal surfaces for various wind configurations, with associated roughness elements view within a grid, as illustrated in Figure 4.2. In this figure, a view of the obstacles (top) is associated with a view of the frontal profile of all the obstacles inside a grid of 100 by 100 m (bottom).

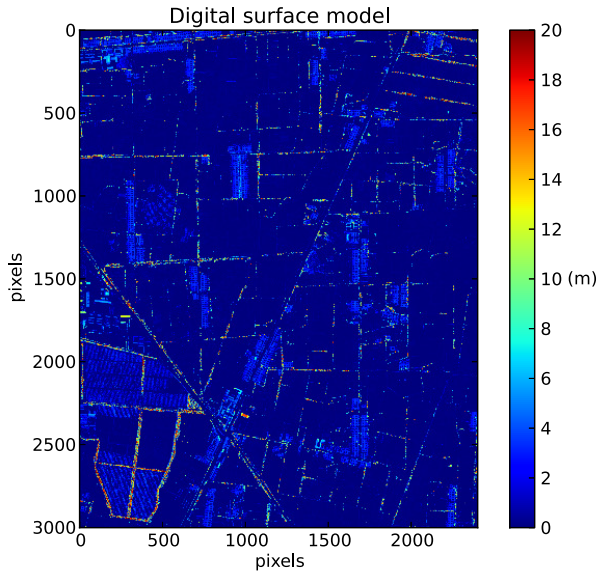

Figure 4.1: Digital Surface Model over the Yingke Oasis obtained from LIDAR data.

The integral of this profile gives the total area for the wind orientation considered. In the Figure 4.2, we present the results for four different wind orientations. For such an area, covered with field crops and tree hedges, the variation of the frontal area with the wind orientation is significant.

Depending of wind direction, the shape of the frontal area opposed to wind flow can change significantly, as illustrated on Figure 4.2, with frontal area index ranging from 0.078 to 0.108. In this particular example, the orientation of the airflow relative to the orientation of the tree rows explains most of the variation, with high values when the wind is perpendicular to the wind flow (45° and 90°), and lower ones when it becomes nearly parallel (0° and 135°).

4.3.2 Configuration of the Computational Fluid Dynamics model

The Canyon CFD requires the input of a Digital Elevation Model and at least one local wind profile for initialization, i.e. wind speed and direction at two levels, and the height of the top of the Planetary Boundary Layer (PBL). As mentioned earlier, the latter parameter is mostly required in non-neutral atmospheric conditions (Lopes, 2003), which are never considered here. It can use a roughness element height map whenever available, or assumes this height constant on the

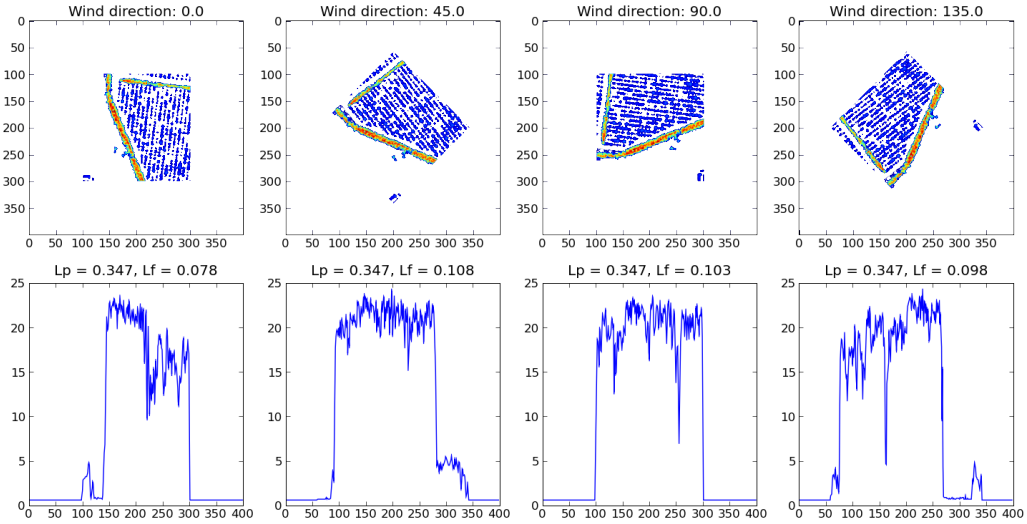

Figure 4.2: A 100×100 m subset covered with field crops and tree rows is presented to illustrate the results of a geometrical processing. The four images at the top present the scene considered from four different view angles, corresponding to wind directions of 0°, 45°, 90° and 135° (from North). The colors express the vegetation height from 60 cm (blue) to 25 m (red). The four bottom images illustrate the frontal area of this subset from each of the four orientations of the wind. Abscissa marks are pixel coordinates, while the ordinate marks represent the obstacle height in meters. L_p refers to the plan area index, and L_f to the frontal area index.

entire scene. In this study, the Digital Surface Model is used to document the height of the elements on the entire scene. Therefore the model can account for both the topography and the surface stress from roughness elements. It should be noted that the Yingke area is almost flat, with a very slight slope from West to East leading to an altitude difference of nearly 30 m over the 2400 m swath of the LIDAR path. The AMS wind speed and direction measurements at 2 and 10 m are used to initialize the profile, together with the PBL height obtained from nearly simultaneous atmospheric soundings. In the following experiments, meteorological contexts are limited to neutrally stratified PBL conditions, leading to the selection of five simulation periods listed in Table 4.1. In each of these five simulation periods, the top of the PBL was identified at 700 m above ground.

Table 4.1: Wind speed and direction measured at Yingke AMS for the selected neutrally stratified Planetary Boundary Layer conditions. The height of the top of the PBL was identified at 700 m in each case.

Date	Wind speed (m/s)		Wind
	2 m	10 m	direction (°)
30 June 2008–15:30 LT	1.11	1.41	251
30 June 2008–16:00 LT	1.01	1.36	295
30 June 2008–16:10 LT	1.17	1.60	277
30 June 2008–16:30 LT	0.95	1.53	270
14 July 2008–16:30 LT	2.44	3.99	51

4.4 Results and discussion

4.4.1 Wind field computation

Wind fields were computed with a ground resolution of 25 m and 15 levels from 5 to 870 m above ground. A control of the computed wind speed at 2 and 10 m with original values from the AMS reveals that speeds can significantly vary. Table 4.2 shows differences between measured and simulated wind speed values. The differences are more important near the surface, with a mean underestimation of 40% for CFD wind speeds at 2 meters, and smaller at 10 m, with a mean underestimation of 10% and mean overestimation of 20%. As quoted in Section 4.2, this is due to the fact that the wind speed provided in input is used as an initial guess for an iterative solving of the transport equation in the three dimensions (Lopes, 2003). The use of lower resolution wind fields from a numerical weather prediction model to define a 3D forcing of the wind speed should give better results, but could not be experimented in this case due to a lack of such data in the period of LIDAR acquisition.

Output wind fields are affected by a border effect on the upstream boundaries of the scene (e.g. on the lower left image of Figure 4.3). This imposes to discard results within the first 150 m north and east of the fields. It could however be overcome following a nested scale approach, with use of a lower resolution regional DEM to compute a first initialization field to be used in place of the AMS initialization measurements. This could not be performed at this stage of the study.

Table 4.2: Comparison between wind speed measured at the AMS and simulated wind speed values obtained with the CFD model.

Date	Wind speed measured (m/s)		Wind speed computed (m/s)	
	2 m	10 m	2 m	10 m
30 June 2008–15:30 LT	1.11	1.41	0.42	1.18
30 June 2008–16:00 LT	1.01	1.36	0.46	1.27
30 June 2008–16:10 LT	1.17	1.60	0.54	1.49
30 June 2008–16:30 LT	0.95	1.52	0.63	1.72
14 July 2008–16:30 LT	2.43	3.99	1.90	5.13

4.4.2 Roughness length processing

LIDAR data were processed to compute the plan area index of the scene, the frontal area indexes for each wind directions, and associated displacement height following both the approaches from Raupach (1994) and MacDonald et al. (1998). The average height of roughness elements within the scene leads to choose a grid size of 100 m, i.e. ten times the height of most of the obstacles to airflow, also tree rows usually reach 30 m, and up to 38 m for some trees. However, the following calculations stick to the 100 m grid to preserve some granularity. Values of λ_p were found to range between 0.08 to 0.64 for tree arrays and some building groups. This leads to $d_{0(Raupach)}/h_v$ values mainly between 0.35 and 0.45, while $d_{0(MacDonald)}/h_v$ values range from 0.2 for bare soil, and up to 0.7 for dense low tree arrays. The lowest λ_f values are of 0.025, but can reach 0.2 for grids containing tree rows. These values are globally rather low since the area does not contain regular arrays of high elements, but rather one-line obstacles like the alignments of trees. Values of z_{0m} are very similar from one orientation to the other, e.g. with a variation of the order of $\pm 8.10^{-3}$ m between values obtained with a 51° and 270° airflow. However, significant variations with wind direction in frontal area index, and as a consequence in roughness length, can be obtained for grids containing tree line structures, as illustrated on Figure 4.2. The difference of values of z_{0m} between the formulations of Raupach (1994) and MacDonald et al. (1998) are more significant, and related to the larger values of displacement height obtained over densely vegetated surface from the MacDonald's formulation. Indeed, $z_{0m(Raupach)}$ ranges from 0.015 to nearly 0.51, with a maximum $z_{0m(Raupach)}/h_v$ of 0.142, while $z_{0m(MacDonald)}$ from 0.015 to 0.195, maximum $z_{0m(MacDonald)}/h_v$ of 0.120.

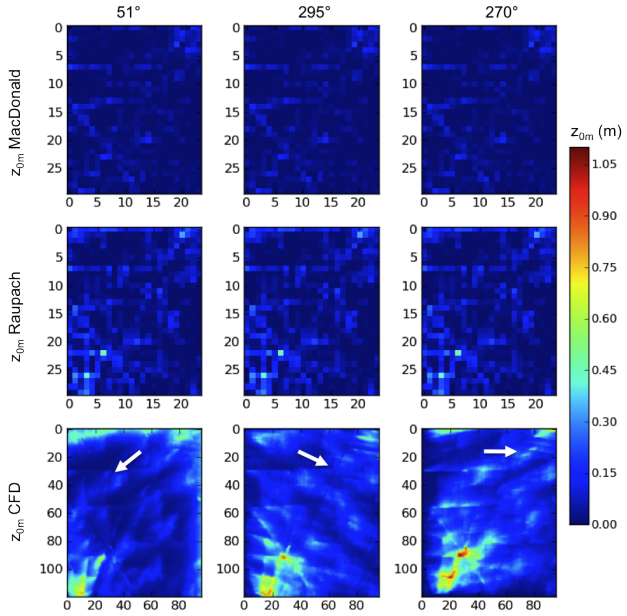

Figure 4.3: Roughness length maps derived from the LIDAR data over the Yingke area (7.2 km^2) for wind flows from N-E (51°), W-NW (295°) and W (270°), presented from left to right, and related results following the approaches from Raupach (1994), MacDonald et al. (1998), and from the CFD, from top to bottom. Arrows represent wind directions accounted in both geometrical and CFD based calculations.

CFD based roughness obtained from the inversion of Equation 4.1 using wind fields give a rather different view of the surface drag effect. Although computations are made at a 25 m ground resolution, a grid value expresses the effect of surface stress upstream on the entire footprint of the profile used in the inversion, while the geometrical approach can only account for the frontal density of obstacles within the calculation grid. Here it is assumed that the footprint for the selected neutral conditions is ten times the height of the profile. To obtain results at local scale, the wind field levels from the ground up to 30 m are used to compute the roughness length, for an assumed footprint size of 300 m. Results presented in Figure 4.3 illustrate very well in particular the shelter effect of tree rows, and simulations differ significantly from one wind direction to the other. Here z_{0m} values are of the order of 0.02-0.03 for low vegetation areas, 0.12-0.2 for corn fields, but can reach values as high as 0.8 and even 1.1 nearby tree hedges areas, depending of the orientation of the airflow as compared to the orientation of the hedges.

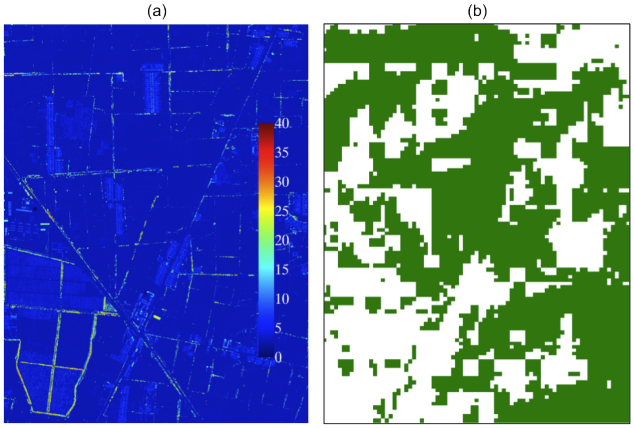

Figure 4.4: **(a)** Roughness element height from the DSM (in meters); **(b)** areas where both $z_{0m(Raupach)}$ and $z_{0m(CFD)}$ match at ± 0.05 m for the calculation with a N-E wind are represented in green. Both figures cover the 7.2 km^2 area of interest.

4.4.3 Discussion

A strict gridwise comparison between geometrical and CFD based results may not be relevant. Indeed geometrical approaches account for airflow orientation, but they cannot reproduce the footprint effect of upstream roughness elements. These approaches are designed for regular arrays of roughness elements. It can very well account for heterogeneity in terms of grassland with staggered arrays of trees, or any configuration where local heterogeneity tends to a meso-scale homogeneity. However, in such a complex land cover context, the CFD approach proves to give a much finer view of interactions between the airflow of the structure and orientations of roughness elements of significant height. That said, geometrical and CFD based z_{0m} tend to converge on large, open areas covered either by bare soil, grassland, low field crops, and even to some extent on some corn fields. For instance, Figure 4.4b shows in green output grids where $z_{0m(Raupach)}$ match $z_{0m(CFD)}$ within a range of ± 0.05 m. Compared to the Digital Surface Model presented on Figure 4.4a, and considering that the wind direction is 51°, it appears rather clearly that beside areas affected by a significant shelter effect, both approaches tend to give comparable results. This suggests that geometrical formulation could give more similar results on natural heterogeneous land covers present in the region, like the sparse grassland and low trees land covers.

It should be mentioned that the values obtained from the CFD wind fields for grids containing tall trees might not be correct. In these calculations, it was decided to use the levels of wind fields within the first 30 m to stick to the 300 m footprint, while in some areas some trees can reach up to 38 m. Further investi-

gations are needed to check the quality of the wind speed estimates in the lower part of the boundary, but it seems clear that in cases where roughness elements can reach such a height, the footprint size should be reconsidered, e.g. by using the first 60 m of wind profiles.

It should also be noted that results from the two approaches could only be compared because of the very low variation of the topography over the scene. The use of the difference between the Digital Surface Model and the Digital Elevation Model in the computation of the frontal area index cannot account for a more significant variation of the elevation, while the combined use of the DEM and DSM in the CFD could still give consistent results.

Finally, it must be emphasized that both the geometrical and CFD approaches assume roughness elements to be solid blocks. In both cases, the Digital Surface Model is used to derive an obstacle height that is used either to estimate a frontal area and intervening spaces, or as a first assumption on local roughness. None of these approaches accounts for the porosity of vegetation canopies. In particular, it is obvious that such a representation of obstacles like the tree rows will lead to overestimate their effect on the flow, while these trees will mainly oppose a resistance to the airflow on levels with the highest foliage density. Therefore, the computation of the roughness length over complex land cover would require accounting for the vertical structure of the canopy. This could be achieved by use of the full waveform of the LIDAR measurements, instead of statistics on points used here.

4.5 Conclusion

Hydrological and micro-meteorological studies based on the modeling of surface heat exchanges from radiometric observations can benefit from the contribution of very high-resolution LIDAR digital elevation and digital surface models over a complex land cover. The geometrical characterization of the surface topography but also the structure of the roughness elements paves the way for a more accurate modeling of aerodynamic processes, and in particular a detailed estimate of the surface roughness.

The implementation of the geometrical approaches to compute the plan area index and the frontal area index, together with the formulations from Raupach (1994) and MacDonald et al. (1998) in a single tool is of very general purpose and could be used either on vegetated or urban areas, provided that the local heterogeneity tends to some homogeneity at the fetch scale. On the other hand, the combined used of the DEM and the DSM in a CFD model proves to account for the complexity of the land cover, in particular for staggered structures of tall roughness elements. However, the spatial meaning of the values is different from

the gridded geometrical approaches, as a 25 m resolution grid actually accounts for the upstream surface stress within its own footprint. It is also emphasized that both the geometrical and CFD based approaches rely on a simple representation of the roughness elements, and do not account for the porosity of foliage structures to the airflow. The definition of the exact footprint of such computations still needs to be investigated. And a cross comparison of results from the CFD based approach with ground measurements at footprint scale could provide a first validation of the results.

Moreover, a general analysis of the structure of the landscape along the airflow should allow for an adequate definition of the footprint size and related wind fields levels to be used in the inversion. Results would also benefit from a nested scale computation of the wind fields. The use of coarser DEM over a larger area for the initialization of the high-resolution computations should remove any border effects. Finally, the use of such approaches over other land cover types, but also more accentuated topographies within the Heihe river basin, could give an extended view of the adequacy of both approaches in various contexts.

Chapter 5

Evaluation of methods for roughness length retrieval

5.1 Introduction

In this chapter, a geometrical (Raupach, 1994) and CFD-based methods for roughness length to parameterize the momentum transfer will be evaluated and compared with other simpler formulations, through the estimation of surface turbulent heat fluxes using the SEBS algorithm. First, it is necessary to produce a complete dataset of required land surface variables, retrieved from WiDAS image data acquired on 7^{th} July 2008. At the scale of the Yingke station surroundings, SEBS simulations are then performed with five different methods for roughness length retrieval. The comparison of estimated heat fluxes with ground measurements corresponding to the acquisition time, will provide an indication about which method is the more accurate in this context.

5.2 Characterization of the land surface

The parameterization of turbulent heat fluxes at the local scale involves the preparation of the radiometric data acquired by the WiDAS sensor, following the SEBS algorithm requirements. A single input dataset of land surface variables is produced, and only the surface geometrical characterization will vary in the different calculations, in order to evaluate the various roughness length parameterization methods, including some empirical relationships.

5.2.1 Land surface parameters retrieval

Land surface properties such as albedo, Normalized Difference Vegetation Index (NDVI), Leaf Area Index (LAI), fractional vegetation cover (f_c), and Land Surface Temperature & Emissivity (LST, LSE) were retrieved from the WiDAS sensor following the methods and formulations detailed below. These land surface variables will remain constant in each experiment.

Albedo

Albedo corresponds to the spectral and hemispheric integral of spectral and directional reflectances over the useful solar spectrum (from 0.3 to 3 μm). As spectral bands of the WiDAS camera do not completely cover this spectrum, a weighting coefficient for incoming solar radiation has to be calculated for each spectral band of the sensor (Figure 5.1). The portion of albedo recorded by the camera (weighted sum of the spectral reflectances) has to be fitted with an integral albedo in order to determine a linear relationship. Using spectral signatures of several surfaces from ASTER libraries, and corresponding to the land cover of the study area, a total albedo is computed for each of them (integrated on the entire useful solar spectrum) and normalised by the incoming solar radiation. Then for each surface, spectral reflectances are computed using the filter functions of the camera, and weighted by the corresponding solar spectrum interval. A linear regression provides the fitting function for total albedo retrieval ($y = 1.11x - 0.02$, $r^2 = 0.96$).

Normalized Difference Vegetation Index

The Normalized Difference Vegetation Index (NDVI) is given by :

$$NDVI = \frac{\rho_{nir} - \rho_{red}}{\rho_{nir} + \rho_{red}} \tag{5.1}$$

where ρ_{nir} and ρ_{red} are the at-surface reflectances obtained from sensor bands located respectively in the near infrared (NIR) and red spectral regions. WiDAS bands 4 (0.75 μm, NIR) and 2 (0.65 μm, red) can be then used to obtain the NDVI. From NDVI, other surface parameters such as Leaf Area Index and fractional vegetation cover are derived.

Leaf Area Index

The Leaf Area Index (LAI) is the leaf area per unit ground area (m^2/m^2). This variable is required for kB^{-1} computation with the Massman's model (Equation 2.47), and can be estimated as :

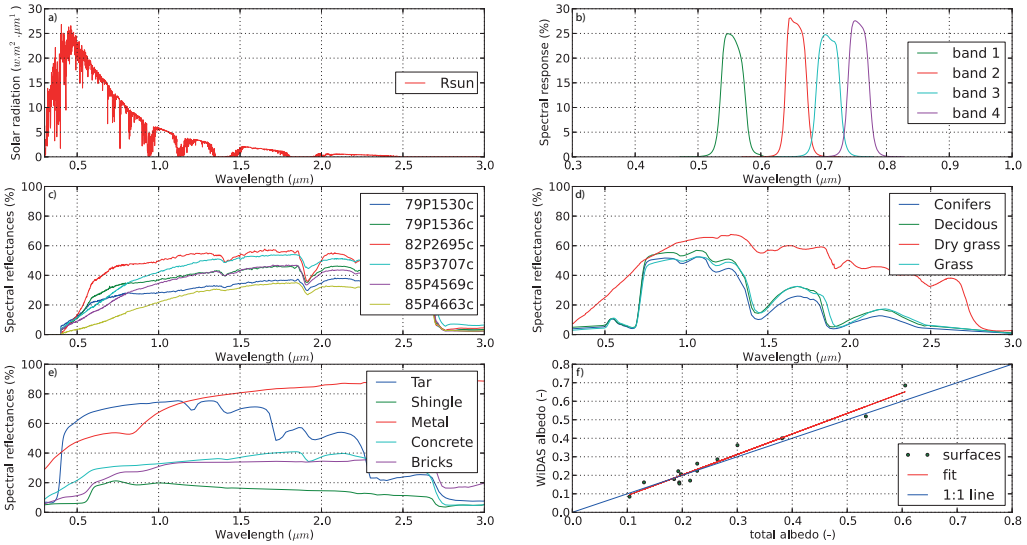

Figure 5.1: Illustration of the computation of the "camera albedo" and global albedo for each type of surface. (a) Incoming solar radiation. (b) WiDAS filter functions. Spectral signatures for soil (c), vegetation (d) and for artificial materials (e). (f) Scatter plot proving relationship to retrieve global albedo from discrete values (WiDAS).

$$LAI = \left(NDVI \times \frac{1 + NDVI}{1 - NDVI} \right)^{0.5} \tag{5.2}$$

Fractional vegetation cover

The fractional vegetation cover (f_c) is defined as the part of ground surface covered by vegetation. It is also required for the computation of kB^{-1} (Equation 2.47), and for ground heat flux estimation (Equation 2.5). f_c has been traditionally estimated from remote sensing data using empirical relations with vegetation indices, as for example the NDVI. It has been demonstrated that f_c depends linearly on NDVI, e.g. as :

$$f_c = \frac{NDVI - NDVI_s}{NDVI_v - NDVI_s} \tag{5.3}$$

where $NDVI_s$ and $NDVI_v$ correspond to representative values of NDVI for bare soil ($f_c \to 0$) and vegetation ($f_c \to 1$), respectively. Other relationships, such as quadratic expressions have also been proposed (Baret et al., 1995; Carlson and Ripley, 1997), but they do not improve the results as discussed by Wittich and Hansing (1995). The main problem when applying Equation 5.3 is the correct estimation of $NDVI_s$ and $NDVI_v$ values. This is a critical task, since these values are region- and season-specific. Here we use the local minimum and maximum values of NDVI, as the landscape ensure the presence of roads, buildings and dense green vegetation.

Land Surface Temperature and Emissivity

Land surface brightness temperature is provided by the radiance measured in the 8-12 μm channel after atmospheric correction using MODTRAN4 (Li et al., 2009a) and Land Surface Temperature (LST) is retrieved from brightness temperature by the separation of emissivity. This latter is estimated from NDVI using the formulation of Van de Griend and Owe (1993) :

$$\epsilon = 1.009 + 0.047 \times ln(NDVI) \tag{5.4}$$

5.2.2 Models for roughness length retrieval

The surface geometry will be characterized following five methods, and results of each are presented below. Besides the geometrical (Raupach, 1994) and the CFD-based methods for roughness length retrieval (Chapter 4), two commonly used

empirical relationships are proposed. An alternate method to exploit the digital surface model is also developed.

Roughness length from NDVI

Some empirical formulations have been proposed to estimate roughness length for momentum transfer (z_{0m}) from vegetation indices such as NDVI. They are generally established for a specific cover and under specific conditions, e.g. a given growing stage. Moran (1990) proposed this relationship :

$$z_{0m} = e^{-5.2+5.3\times NDVI} \tag{5.5}$$

with the displacement height d_0 :

$$d_0 = z_{0m} \times 4.9 \tag{5.6}$$

and the vegetation height h_v :

$$h_v = z_{0m}/0.136 \tag{5.7}$$

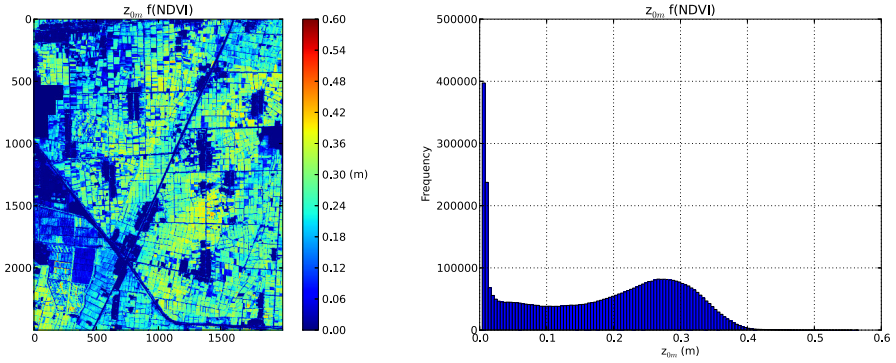

(a) Map of roughness length

(b) Distribution of roughness length values

Figure 5.2: Roughness length for momentum transfer values over the Yingke Oasis station following Moran's formulation.

Figure 5.2 reveals that where the surface presents high NDVI values, roughness length is larger. Using this formulation, where crops are green and dense but low, roughness values are large and on contrary where vegetation is more sparse but high, values are low. Buildings, which presents negative NDVI values, are not considered as obstacles for momentum transfer. It clearly appears that this kind of formulation is not reliable in this context.

Roughness length as a fraction of vegetation height

Roughness length for momentum transfer can also be estimated as a simple fraction of vegetation height. In this study, taking benefits from the LIDAR digital surface model, we know the height of each obstacle around the Yingke Oasis station with an horizontal resolution of 1 m. Following Brutsaert (1982), we consider that :

$$z_{0m} = 0.136 \times h_v \tag{5.8}$$

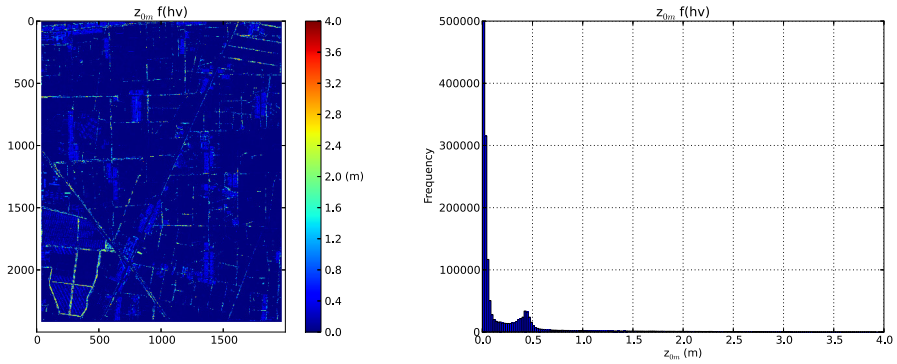

(a) Map of roughness length

(b) Distribution of roughness length values

Figure 5.3: Roughness length for momentum transfer values over the Yingke Oasis station following Brutsaert (1982) formulation.

Figure 5.3 illustrates z_{0m} values obtained by the application of this simple formula (Equation 5.8). The range of values is limited to 4 m in Figure 5.3a since the occurrence of higher values is marginal. Also the frequency range in Figure 5.3b is limited to 500,000 in order to show the distribution of z_{0m} values. As roughness length is simply proportional to the vegetation height, lowest values (from 0 to 0.05 m) are retrieved for the crops (i.e. low vegetation) and highest ones are found for the trees (from 1 to 4 m). Buildings and some crops show generally mean values of roughness length. Displacement height is retrieved in the same manner as in Equation 5.6.

Roughness length as a function of the standard deviation of vegetation height

Another measure of the geometrical regularity of a vegetation canopy is the standard deviation of vegetation height taken as an objective measurement of surface roughness (Menenti and Ritchie, 1994; Menenti et al., 1996). Menenti and Ritchie (1994) applied Equation 5.9 to estimate the local aerodynamics length (z_{0m}) due

to the intervening complete and partial canopies from segments of laser measurements. The original expression proposed by the authors is adapted here for a two-dimensional array, i.e. the digital surface model. Roughness length is derived from the DSM grid using a j by j kernel, where j is an odd number, scanned over all pixels of the grid :

$$z_{0m} = \frac{1}{n} \sum_{i=1}^{n} \left[\frac{(\sigma_{h_i} - \sigma_0)}{h_i} \right] \bar{h} \tag{5.9}$$

with $n = 9$ since $j = 3$, σ_{h_i} the standard deviation of the i^{th} pixel of the kernel, σ_0 the instrument noise ($\sigma_0 = 0.03$), h_i the elevation of the i^{th} pixel located inside the kernel and $\bar{h}$ the mean elevation in the kernel.

This formulation is the first in a sequence of equations proposed by Menenti and Ritchie (1994) to estimate the effective aerodynamic roughness length of a composite landscape. The local z_{0m} calculated above is then used to estimate the effective aerodynamic roughness of the mixture of herbaceous vegetation with taller and sparse shrubs and trees (Z_{0m}), using the following equation (Arya, 1975) :

$$\begin{aligned} ln\left(\frac{Z_{0m}}{z_{0m}}\right) =& \frac{4}{5}\left[ln\frac{h}{z_{0m}} + ln\left(\frac{1}{\lambda} - \frac{b}{h} - \frac{B}{h}\right)\right] \\ & \times \left\{1 - \left[1 - m\lambda - \frac{C_{dh}\lambda}{2k^2} ln\left(\frac{h}{z_{0m}}\right)^2\right]^{-1/2}\right\} \end{aligned} \tag{5.10}$$

where k is the Von Karman's constant, $m = (b/h) + (B/h) + (L/2h)$, b is the base width of shrubs (m), h is the height of shrubs (m), B is the base width of the region with separated airflow behind obstacles (m), $\lambda = h/s$, s is the spacing of shrubs (m), and L is the restoration length of the logarithmic profile in the surface layer behind obstacles.

To estimate an effective aerodynamic roughness length (Z'_{0m}) which includes the effects of topography, besides low vegetation and shrubs, the formula given by Taylor et al. (1989) has to be applied :

$$ln\left(\frac{Z'_{0m}}{Z_{0m}}\right) = 3.5\left(a\frac{2\pi}{\lambda}\right)^2 ln\left(\frac{\lambda}{Z_{0m}}\right) \tag{5.11}$$

with a the amplitude of relief (described as periodic) and λ the wavelength of periodic relief.

The Z'_{0m} values apply to larger length scales and higher air levels than the Z_{0m} values obtained with Equation 5.10. Considering the local scale and the relatively

flat terrain of the Yingke area, this formulation is not appropriated in this study and thus not used.

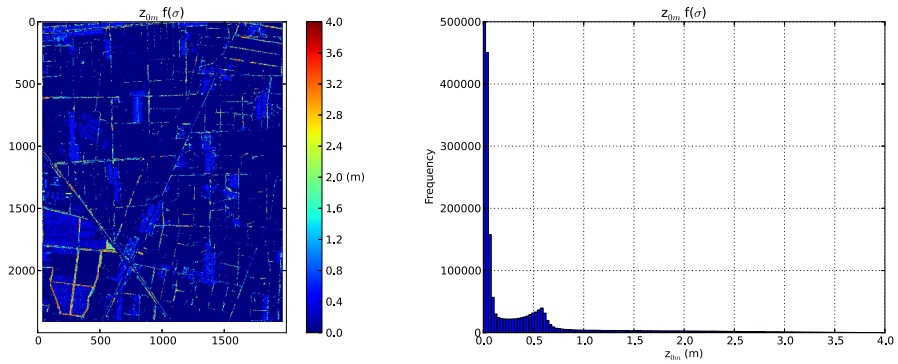

(a) Map of roughness length

(b) Distribution of roughness length values

Figure 5.4: Roughness length for momentum transfer values over the Yingke Oasis station retrieved from σ_h.

Figure 5.4 presents the map and distribution of Z_{0m} values obtained with the sequence of Equations 5.9 and 5.10. The range and the distribution of roughness values is very similar to the results obtained with Equation 5.8 (cf. Figure 5.3). Some very high values are also located in the range 1-5 m.

Roughness length from Raupach's formulations and CFD model

Figure 5.5 presents the roughness length values obtained using respectively CFD and Raupach's models. The two computation were performed with the wind characteristics measured at the Yingke AMS station. The distribution of values retrieved from CFD model is ranging from 0 to 1 m, with a peak around 0.05 m. Lowest values are never equal to 0, since with this method "everything is roughness". The spatial distribution of roughness values using Raupach's model is obviously very similar to Brutsaert's (Figure 5.3a) and Menenti and Ritchie's (Figure 5.4a) methods since they are directly linked to the digital surface model (DSM). Due to the computing resolution, this process provides an aggregation of rough elements. The interesting point is that the range of z_{0m} values is more reasonable and consistent with the local landscape.

Design of the different experiments

Following the different methods proposed for the geometrical characterization of the land surface, a set of five scenarii for surface energy balance estimation is cre-

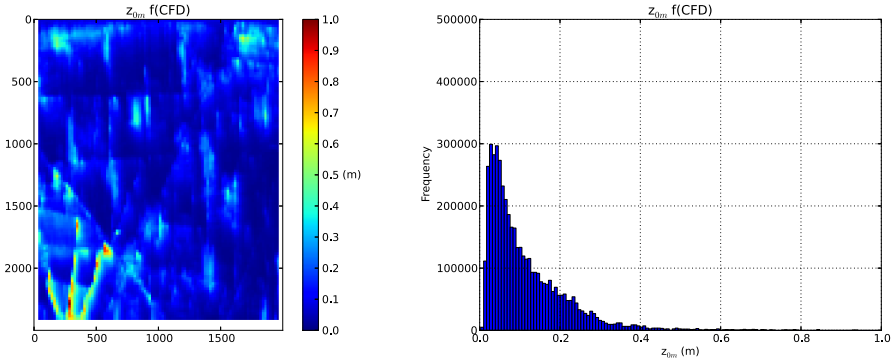

(a) Map of roughness length

(b) Distribution of roughness length values

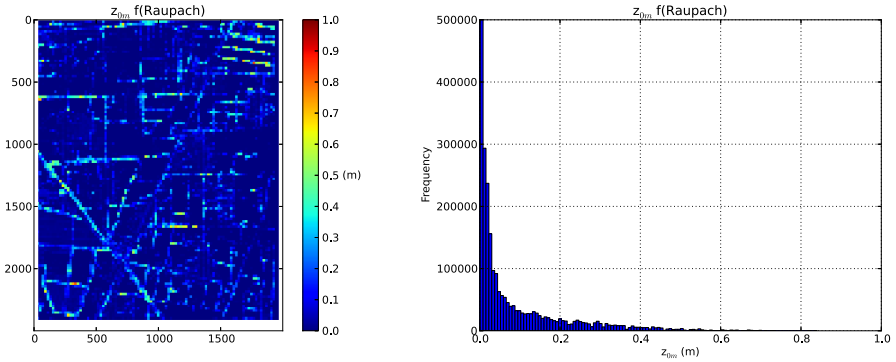

(c) Map of roughness length

(d) Distribution of roughness length values

Figure 5.5: Roughness length for momentum transfer values over the Yingke Oasis station retrieved from CFD and Raupach's model.

ated and results will be compared with ground measurements at the EC footprint scale. Considering the lack of usable WIDAS acquisitions, the evaluation has also to be considered in a temporal perspective. For each numerical experiment, input data are the same but only the vegetation height, zero-plane displacement height and aerodynamic roughness length for momentum are modified. The exact content of the experiments is described below and summarized in Table 5.1 :

- the first experiment is considered as the "by default" case for a SEBS calculation, with z_{0m} assumed to be function of NDVI, and h_v and d_0 to be a fraction of roughness length.

- the second experiment is a kind of improved "by default" configuration. The vegetation height is provided by the LIDAR data and d_0 and z_{0m} formulations remain the same as before.

- the third one integrates the effective aerodynamic roughness length retrieved following Menenti and Ritchie (1994). The vegetation height is provided by the LIDAR data and d_0 is still considered proportional to z_{0m}.

- the fourth one includes z_{0m} values retrieved from the inversion of the CFD windfield over the Yingke area. The resolution of roughness data is 25 m, resampled to 1.25 m in order to match with VNIR data. h_v is also derived from LIDAR data and d_0 proportional to z_{0m}.

- the last experiment integrates z_{0m} and d_0 values computed using Raupach's formulations. Here again the initial computing resolution is 25 m, resampled to the VNIR data resolution. The vegetation height is provided by the LIDAR data.

Table 5.1: Summary of methods used for the surface geometrical characterization in each experiment performed over the Yinke area.

	METHODS				
	$NDVI$	$LIDAR$	$M\&R$	CFD	$Raupach$
1.	h_v - z_{0m} - d_0				
2.		h_v - z_{0m} - d_0			
3.		h_v	z_{0m} - d_0		
4.		h_v		z_{0m} - d_0	
5.		h_v			z_{0m} - d_0

5.3 Spatial evaluation of estimated turbulent heat flux densities at the footprint scale

In this section, the reliability of geometrical-based and CFD-based roughness values retrieved in Chapter 4 is evaluated with their use with the SEBS algorithm. Five experiments are performed in order to compare the benefit of each method presented above in Section 5.2, in the estimation of turbulent heat fluxes. Atmospheric input data such as longwave and shortwave radiation, wind speed, air temperature, air pressure and specific humidity measured at 10 m above ground level by the AMS are input data applied in all the experiments.

5.3.1 Surface radiative balance

SEBS first resolves surface radiative balance based on WiDAS surface albedo, temperature and emissivity combined with measured incoming longwave and shortwave radiation. Ground heat flux is assumed to be a fraction of net radiation weighted by the fractional vegetation cover (Equation 2.5). Surface radiative balance is common for the five experiments since atmospheric and land surface parameters given as input remain the same.

As it is impossible to identify accurately the target seen by the instruments and its corresponding pixel(s), the estimated radiative terms are averaged at the scale of the heat flux footprint. The comparison between measurements and estimates of brightness temperature, ground heat flux and net radiation is given in Table 5.2.

Table 5.2: Measurements of radiative terms at the Yingke station for the 7^{th} July 2008 at 11h30 am (Beijing time).

Variables	Measurements	Estimations
Rn (W/m^2)	637.38	699.40
G_0 (W/m^2)	8.96	107.54
$Rn - G_0$ (W/m^2)	628.42	591.86
T_b (°C)	26.54	25.38

Net radiation for the source area located upstream of the station is overestimated about 9.7% (+62 W/m^2), while brightness temperature is around 1°C less (Table 5.2). It means that the error comes from the estimation of albedo or emissivity, but it remains acceptable under 10%. The soil heat flux G_0 is largely overestimated by SEBS, while the measured value is extremely low considering the surface temperature and the time of measurement (around noon). At this period of the day, considering the season and latitude, the soil heat thermal admittance should be higher. But the estimated at-surface available energy $Rn - G_0$ is finally close to measurements with an underestimation of -5.8% (-37 W/m^2), since the initial difference is reduced due to an important value of G_0.

5.3.2 Surface energy balance

Ground measurements of turbulent heat fluxes provided by the eddy covariance system are listed in Table 5.3. The footprint of the source area of land surface which contributes to the measured heat fluxes has a total area of 17 600 m^2 and is represented on Figure 5.6. Since the measured soil heat flux is very low, the at-surface available energy ($Rn - G_0$) is large and exceeds the sum of latent and

sensible heat flux (+244 W/m^2). A method which preserves the Bowen ratio is applied to correct for the unclosed energy balance (Twine et al., 2000). The residuum is divided up according the Bowen ratio ($Bo = H/\lambda E$) and distributed to sensible and latent heat accordingly. The Bowen ratio after correction is the same as before.

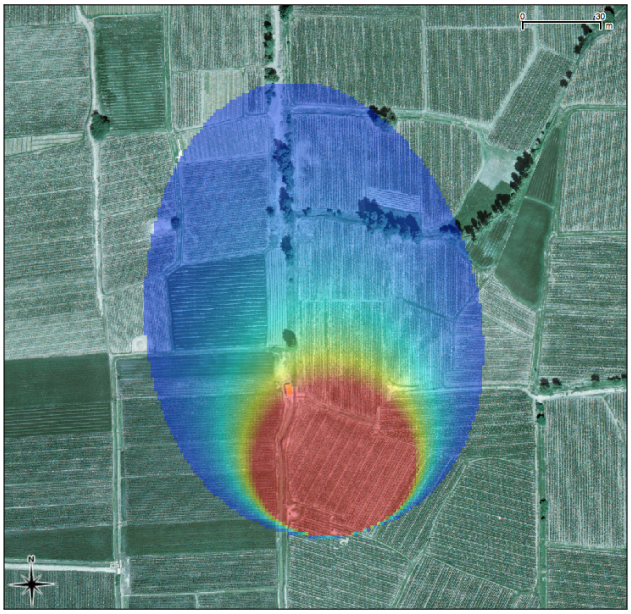

Figure 5.6: Footprint corresponding to the source area of turbulent heat flux densities measured by the eddy covariance system. Color represents the importance of the contribution.

Table 5.3: Measured and corrected heat flux densities at the Yingke station for the 7^{th} July 2008 at 11h30 am (Beijing time).

Variables	Measured	Corrected	Variation
λE (W/m^2)	340.11	556.13	+216.02
H (W/m^2)	44.21	72.29	+28.08
Λ (-)	0.88	0.88	

Heat fluxes are spatially integrated by applying the footprint weighted coefficients and results are presented in Table 5.4 for each experiment. Values of spatially integrated roughness lengths and kB^{-1} are also given. Experiments 2 and 4 are able to estimate H respectively with a difference of +4.9% and -10.6%, λE

of -7.3% and -5.2%, and the partitioning over fluxes is very close to the observed value of evaporative fraction (0.88). It appears clearly that experiment 1, based on Moran (1990) for z_{0m} retrieval, is the least able to estimate sensible heat fluxes with a large underestimation of about -76.1% since roughness values for momentum and heat transfer are both extremely high for this situation. It confirms the first appreciation about the distribution of roughness values in Section 5.2.2.

Table 5.4: Results of simulated heat fluxes densities and roughness length at the EC footprint scale for the five experiments.

Experiment	λE (W/m^2)	H (W/m^2)	Λ (-)	z_{0m} (m)	kB^{-1} (-)	z_{0h} (m)
1.	589.91	18.14	0.97	0.288	3.85	0.0058
2.	512.03	79.67	0.87	0.014	3.59	0.0004
3.	467.70	124.08	0.79	0.017	3.49	0.0001
4.	523.71	67.84	0.89	0.026	6.15	0.0005
5.	500.68	91.18	0.85	0.008	3.99	0.0001

Considering not only the strict footprint area, it has to be noticed that there is no result for pixels where $h_{ref} > d_0$, since the negative value of $h_{ref} - d_0$ returns computing errors in the sequences concerning kB^{-1}, friction velocity (u^*), stability functions (ψ_m and ψ_h) and external resistances (r_{ah}). It typically occurs where h_v is very high in experiments 2 and 3. Also, kB^{-1} values are consistent in experiments 1 and 2 since they keep proportionality between h_v, d_0 and z_{0m}. But when d_0 and z_{0m} are not directly related to h_v as it is the case in experiments 3, 4 and 5, kB^{-1} values are sometimes huge due to the ratio z_{0m}/h_v in Equation 2.47 proposed by Massman (1999), which yields calculation errors for some pixels. The consequence is that results of kB^{-1} and z_{0h} in Table 5.4 are not consistent with z_{0m} following the Equation 2.12.

In experiment 5 this problem is explained by the spatial computing resolution of z_{0m} (25 m) which can give high roughness values for pixels where h_v is low. Concerning experiment 4, this point is particularly important since the roughness propagates downstream of obstacles following the wind flow, for instance over crops with low vegetation located after high tree rows. A solution could be to set an upper bound on kB^{-1}, e.g. 25. For experiment 5, this problem could be avoided or reduced by also aggregating h_v values. In experiment 4, an other solution could be to remove h_v provided by LIDAR data and to use Equation 5.7 in order to restore proportionality between geometrical terms and to keep consistency in kB^{-1} values.

Table 5.5 presents the results for experiments 3, 4 and 5 after modification of the h_v values which are now proportional to z_{0m} and d_0 as in experiments 1 and

2. This correction does not really affect results of flux densities and related kB^{-1} and z_{0h} in experiments 3 and 5. It means that the deviation in the ratio z_{0m}/h_v was not so important. However it has a more significant impact in experiment 4 with a sharp decrease of kB^{-1} from 6.15 to 3.66 and a resulting increase of z_{0h} which leads to an underestimation of H (-22.9%) but reduces the error for λE (-3.6%).

Table 5.5: Results of simulated heat fluxes densities and roughness length at the EC footprint scale after kB^{-1} correction.

Experiment	λE (W/m^2)	H (W/m^2)	Λ (-)	z_{0m} (m)	kB^{-1} (-)	z_{0h} (m)
3.	466.61	123.67	0.79	0.017	3.39	0.0001
4.	532.22	58.64	0.90	0.026	3.66	0.0007
5.	502.33	89.60	0.85	0.008	3.56	0.0003

The difference between roughness values is very interesting. For instance, the value estimated with the model proposed by Raupach (1994) is very low. According to the Davenport-Wieringa roughness-length classification (Wieringa, 1998; Wieringa et al., 2001) reported in Table 5.6, this range of values around 0.005 m, corresponds to a 'smooth' surface, such as a featureless landscape equivalent to a flat beach or snow-covered land. The value of 0.288 m estimated by Moran's formulation is expected for a 'rough' surface, as an area with high crops of varying heights and scattered obstacles. This description is not consistent with the station surroundings, but could be consistent with the dense cultivated area located in the south-west part of the scene. The value retrieved from the CFD (0.026 m) is very coherent, according to the same classification it corresponds to an 'open' surface like low vegetation with isolated obstacles. In this area z_{0m} values from CFD are moderate due the absence of huge obstacle and the relative distance from high tree rows. Values retrieved from Brutsaert (1982) and Menenti and Ritchie (1994) are very similar and in between 'smooth' and 'open'.

Finally, considering the errors in the estimation of both sensible and latent heat fluxes, and also the ability to preserve the partitioning provided by the evaporative fraction (Λ), experiments 2 and 4 prove to be the most suitable to estimate heat flux densities. However, a validation based on a single case study can not be considered as sufficient and must be repeated several times. Since there is only one WiDAS dataset available over the Yingke area, a temporal evaluation was performed at the scale of the meteorological station.

Table 5.6: Davenport classification of effective terrain roughness (Wieringa et al., 2001).

Class name	z_{0m} (m)	Landscape features
1. Sea	0.0002	Open sea or lake (irrespective of wave size), tidal flat, snow-covered flat plain, featureless desert, tarmac and concrete, with a free fetch of several kilometers.
2. Smooth	0.005	Featureless land, without any noticeable obstacles and with negligible vegetation, e.g. beaches, peak ice without large ridges, marsh and snow-covered or fallow open country.
3. Open	0.03	Level country with low vegetation (e.g. grass) and isolated obstacles with separations of at least 50 obstacles heights, e.g. grazing land without windbreaks, heather, moor and tundra, runway area of airports. Ice with ridges across-wind.
4. Roughly open	0.10	Cultivated or natural area with low crops or plant covers, or moderately open country with occasional obstacles (e.g. low hedges, isolated low buildings or trees) at relative horizontal distances of at least 20 obstacles heights.
5. Rough	0.25	Cultivated or natural area with high crops or crops of varying height, and scattered obstacles at relative distances of 12 to 15 obstacles heights for porous objects (e.g. shelterbelts) or 8 to 12 obstacle heights for solid objects (e.g. buildings).
6. Very rough	0.5	Intensively cultivated landscape with many rather large obstacle groups (large farms, clumps of forest) separated by open spaces of about 8 obstacle heights. Low densely-planted major vegetation like bushland, orchards, young forest. Also, area moderately covered by low buildings with interspaces of 3 to 7 buildings heights and no high trees.
7. Closed	1.0	Landscape regularly covered with similar-size large obstacles, with open spaces of the same order of magnitude as obstacle heights, e.g. mature regular forests, densely built-up area without much building height variation.
8. Chaotic	> 2.0	City centers with mixture of low-rise and high-rise buildings, or large forests of irregular height with many clearings.

5.4 Temporal evaluation of estimated turbulent heat flux densities at the AMS scale

5.4.1 Production of a time-serie

In this section, a short time-serie of heat fluxes is produced at the scale of the AMS (one-dimension) in order to perform an evaluation of roughness length retrieval methods based on several occurrences. Considering that the land cover and its associated properties remain slightly constant during few days, the evaluation covers a period of two weeks ranging from the 30^{th} June to the 14^{th} July with a time step of 30 minutes, for a total of 721 calculations.

Land surface parameters such as albedo, NDVI, LAI, fractional vegetation cover, emissivity, vegetation height and roughness length are averaged over an area corresponding to 100 by 100 pixels (15 000 m^2) and centered on the AMS. This subset allows to capture the heterogeneity of the surrounding landscape, but also includes changes in wind direction and the related source area of heat fluxes.

As noticed previously in Section 5.3, Equation 2.5 is not really able to estimate accurately soil heat flux in this context. Since the radiative budget is common for all experiments, it is chosen to provide the measured G_0 to SEBS in order to limit errors in the determination of the at-surface available energy $Rn - G_0$. Also, the energy balance is corrected once again using Bowen ratio in order to compensate large differences between $Rn - G_0$ and $H + \lambda E$ as testifies Figure 5.7.

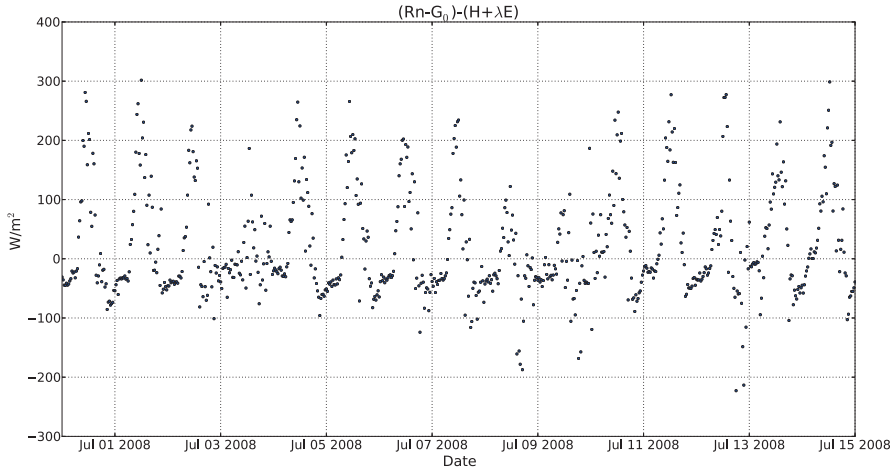

Figure 5.7: Time-serie of energy balance deficit from the 30^{th} June to the 14^{th} July 2008 at the Yingke station.

The correction is only applied when both H and λE exceed 10 W/m^2 and $Bo > 0$, which limits to 253 the number of occurrences, mainly during daytime.

Then, only wind profiles corresponding to near-neutral condition are selected. Stability conditions are estimated using the gradient Richardson number (R_i) :

$$R_i = \frac{g}{T_a}\frac{\partial\theta}{\partial z} \Big/ \left(\frac{\partial u}{\partial z}\right)^2 \tag{5.12}$$

where θ is the potential temperature. When $R_i \to 0$ the stratification is neutral and the profile is generally accepted to be logarithmic (Equation 4.1). Here the threshold is set to $\pm$ 0.1, which limits to 161 occurrences for validation. RMSE on estimated Rn is 23.38 W/m^2 for the entire period and 31.97 W/m^2 for the retained cases (Figure 5.8).

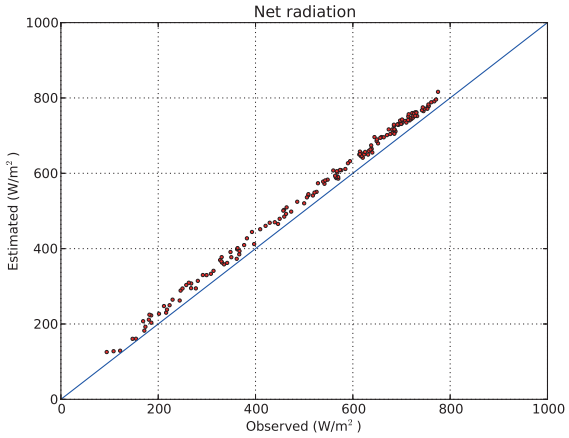

Figure 5.8: Scatter plot of measured and estimated net radiation from the 30^{th} June to the 14^{th} July 2008 at the Yingke station. RMSE = 31.97 W/m^2.

5.4.2 Results

Table 5.7 presents RMSE in the estimation of latent and sensible heat fluxes and corresponding roughness length values for each experiment, except experiment 4 for which z_{0m} varies following wind measurements. Figure 5.9 shows the distribution of the 161 roughness length values, with an important frequency in the range 0.025 - 0.05 m and a secondary peak around 0.1 m. In experiment 5, z_{0m} value is considered constant since the variation of wind direction does not induce sensible changes in this context. The scatter plots between measurements and estimations for sensible and latent heat flux are respectively presented in Figures 5.10 and 5.11.

This temporal evaluation of estimated heat flux densities reveals that experiments 2 and 4 are the most able to estimate sensible heat flux with respectively RMSE of 33.88 W/m^2 and 30.26 W/m^2. Experiments 3 and 5 present very close

Table 5.7: RMSE of simulated heat flux densities and associated roughness length at the AMS scale.

Experiment	λE (W/m^2)	H (W/m^2)	Λ (-)	z_{0m} (m)
1.	76.16	47.11	0.114	0.2535
2.	35.66	33.88	0.076	0.0128
3.	33.71	45.02	0.084	0.0027
4.	44.78	30.26	0.081	-
5.	33.55	43.87	0.084	0.0032

errors since z_{0m} values are almost similar. Also, experiment 1 is definitively based on the worst formulation for roughness length retrieval in this context. These results confirm what was observed in Section 5.3 with the spatial evaluation at the footprint scale.

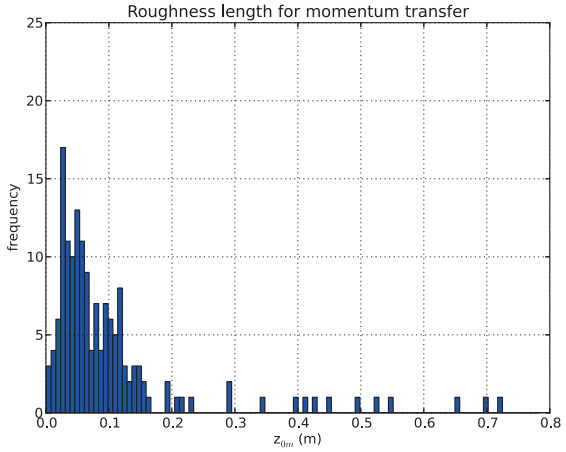

Figure 5.9: Distribution of z_{0m} values retrieved from wind profiles measured at the AMS (mean : 0.13 m, std dev. : 0.20 m).

5.4.3 Discussion

This evaluation proves that, in the context of the Yingke oasis station, experiments 2 to 4 gave reliable estimations of sensible heat flux and a consistent partitioning between turbulent heat fluxes, at least in the context of a 1D time-serie at the station scale. However, at the footprint scale only experiments 2, 4 and 5 are considered reliable. The absence of other datasets over the Yingke area does not allow to draw rigorous conclusions.

However, results of calculations show that a better estimation of H leads to larger errors on λE. But, usually the main interest by solving the energy balance in hydrological studies is to obtain a good determination of λE and, by extension, of the actual evaporation rate. In this sense, experiment 2 gives the smallest errors on H and λE and keeps the correct partitioning of heat fluxes.

This evaluation also reveals that the estimation of sensible heat flux and partitioning, at the footprint scale, is more consistent in experiment 4 when vegetation height is not corrected with respect to kB^{-1}. The absence of correction can lead to extreme values of kB^{-1} in some context and for few pixels, but at the scale of the station it is very appropriate as seen in Table 5.4. This raises the question about the absolute necessity to keep a linkage between h_v, d_0 and z_{0m}, whereas the roughness length retrieved from CFD is purely based on an aerodynamic consideration : for a same place, various z_{0m} and d_0 values can be observed for a same vegetation shape, since an infinity of wind speed, direction and upstream history are possible.

Linearity between these geometrical parameters (h_v, d_0 and z_{0m}) is always retrieved in the formulations given by Moran (1990) and Brutsaert (1982), or also by Su et al. (2001), among others (Covey, 1963; Kustas et al., 1989a; De Vries et al., 2003). Moreover, Su et al. (2001) demonstrated that the Massman (1999) kB^{-1} model is particularly sensitive to the vegetation height, with a relative error up to 46% of the mean measured H when using 150% of the h_v reference value. Thus, if h_v is systematically calculated from the retrieved z_{0m} values, it increases errors in the parameterization of kB^{-1} parameter in experiments 3, 4 and 5. This also explain why experiment 2 gives accurate estimates of heat fluxes, since d_0 and z_{0m} are derived from the measured h_v in a simple and apparently efficient way. It is difficult to determine which are both the good parameterization for z_{0m} and kB^{-1}. The use of another kB^{-1} model, which allows for any roughness length retrieval method, could be relevant.

Also, the representativeness and accuracy of ground measurements should be assessed. The surface energy balance is corrected using the measured radiative budget, but the footprint for SRB and SEB measurements is not the same. There is a considerable difference between the surface covered by the narrow field of view of a pyranometer, and the source area that contributes in EC measurements. Considering an extended homogeneous area (bare soil or fully vegetated), this may not have a large impact. However, this correction is partially biased in a context of heterogeneous landscape such as an irrigated farmland. The meaning of the measured ground heat flux is also a key point. Values of G_0 observed at the Yingke station are very low, and the simple model usually used in SEBS already proved its reliability, but in this context there is a huge deviation. The incapacity to identify the origin of error makes more difficult the correction of measured turbulent heat fluxes using Bowen ratio.

5.5 Conclusion

This study evaluated the difference between experiments 2 and 4 in the estimation of turbulent heat fluxes and so, the ability of the methods for roughness length retrieval proposed by Brutsaert (1982) and Colin and Faivre (2010). However, the formulation used in experiment 2 allows to minimize errors in both latent and sensible heat flux, and to preserve a good partitioning. This formulation is also easier to implement in an operational context. Meanwhile, an additional evaluation of these two methods based on an other kB^{-1} model is necessary, to avoid the need of proportionality between geometrical terms ($h_v > d_0 > z_{0m}$) which is not always compatible with CFD-based retrieval method.

The methods used in this evaluation are suitable for local studies (except experiment 1), and when LIDAR datasets can be available, which is rather unusual. Considering investigations on roughness length retrieval at larger scales, literature often advocates the use of empirical relationships based on vegetations indices, with all the limitations that were demonstrated here by applying the method from Moran (1990). For regional applications, the likely uncertainty of the roughness information will be significant. For instance, most of the Numerical Weather Prediction Models use a detailed land cover classification combined with phenological data for acting as a surrogate.

During the WATER intensive observation period, only one LIDAR acquisition was operated over the Yingke oasis station. In the perspective of an extended study on the seasonality of the land surface roughness, a flight frequency of once every month or two months could be interesting to characterize the annual variation of z_{0m} in the Yingke area. The vegetation growth, but also seasonal changes in the regional wind flow, should be key factors in the roughness variation of land surface.

An other perspective could be to perform this evaluation again for a place more affected by the surrounding obstacles. In this study, the AMS is located in an open area as it is required for ground measurements. But, considering the investigations for roughness length retrieval, it would be interesting to have a station located downstream to major obstacles, as the area of crops bounded by tree rows on the south-west part of the scene.

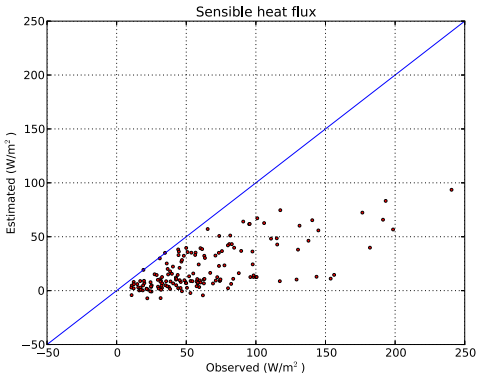

(a) Experiment 1

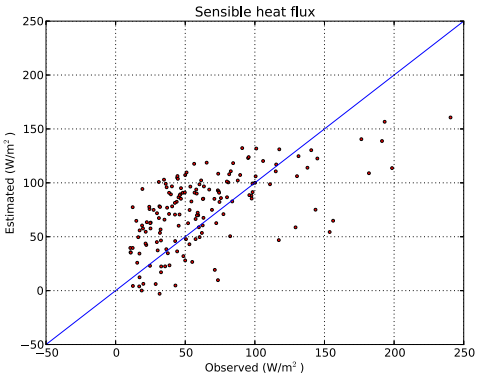

(b) Experiment 2

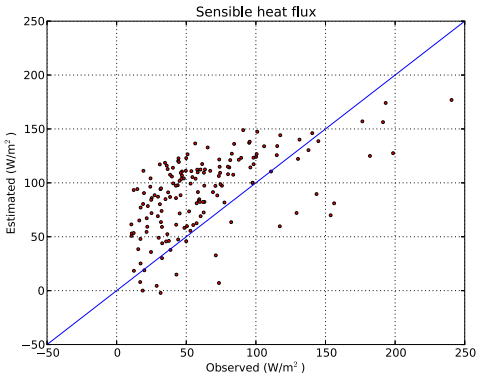

(c) Experiment 3

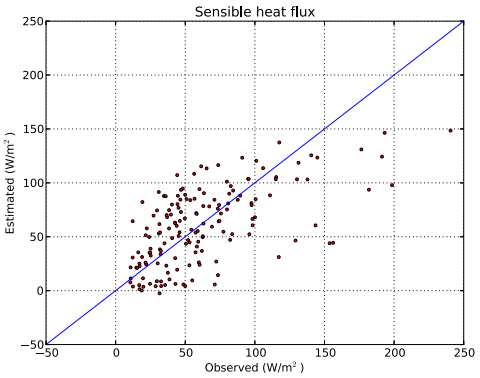

(d) Experiment 4

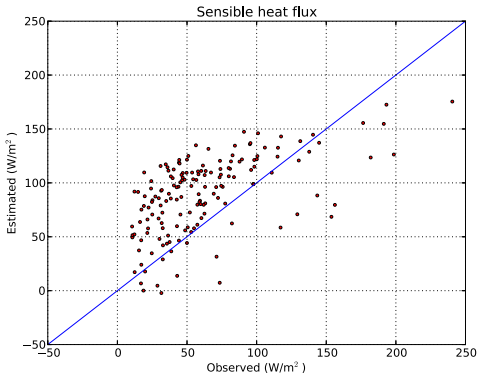

(e) Experiment 5

Figure 5.10: Scatter plots of measured and estimated sensible heat flux for each experiment.

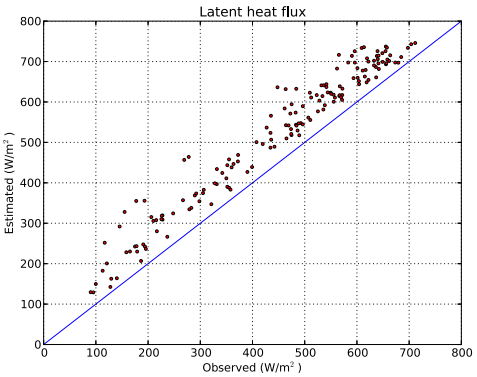

(a) Experiment 1

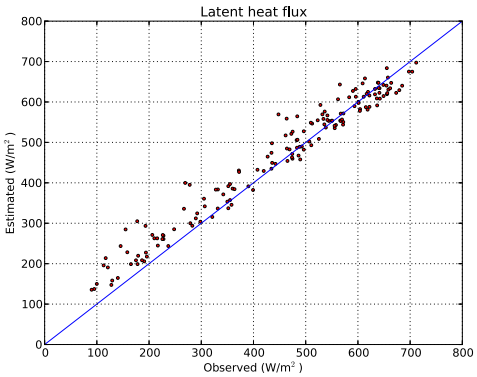

(b) Experiment 2

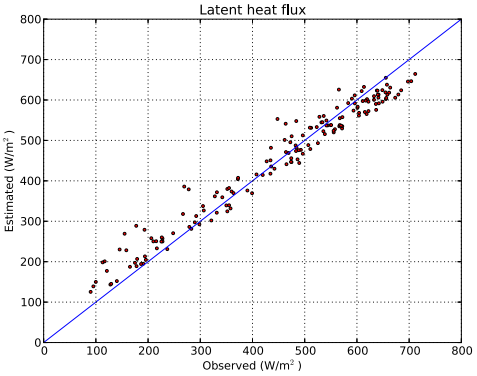

(c) Experiment 3

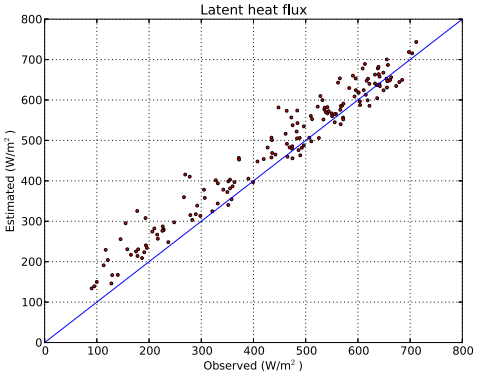

(d) Experiment 4

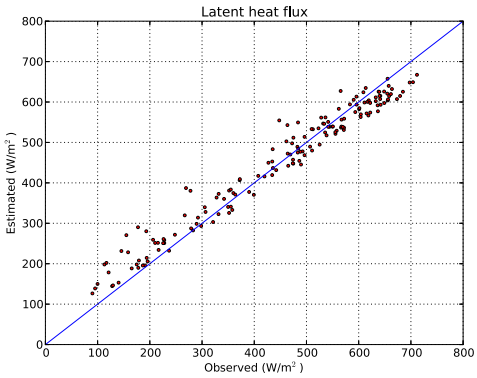

(e) Experiment 5

Figure 5.11: Scatter plots of measured and estimated latent heat flux for each experiment.

Chapter 6

Exploitation of multi-angular data for the characterization of heat transfer

6.1 Introduction

As demonstrated in Chapter 5, the parameterization of turbulent heat fluxes requires a good estimation of aerodynamic roughness length for momentum (z_{0m}) intervening in the calculation of roughness length for heat transfer (z_{0h}) and so, of external resistances (r_{ah}). Thus, an appropriate parameterization of kB^{-1} is also a key aspect in this retrieval for accurately relate z_{0m} to z_{0h}.

Since the 1930's, scientists have been studying the kB^{-1} parameter for all kind of natural and artificial surfaces, ranging from aerodynamically smooth to rough. These studies led to a number of formulations for kB^{-1} retrieval, partly reviewed and evaluated by Verhoef et al. (1997). During the last three decades, the interest in the topic of kB^{-1} has been revived by the remote sensing community (Kustas et al., 1989b; Sugita and Brutsaert, 1990; Stewart, 1995; Su, 2002) who used the bulk transfer theory (Equation 2.6) to calculate sensible heat flux from remotely sensed land surface temperature.

Su et al. (2001) evaluated two advanced kB^{-1} models in the perspective of remote sensing and numerical weather prediction applications. The first one is adapted from Massman (1999) and currently implemented in SEBS (Equation 2.47), and the second one has been proposed by Blumel (1999). These models provided reliable estimates of sensible heat flux over heterogenous land surfaces such as cotton fields, shrubs and grass. However, they also suffer from a limitation in the strict requirement on the proportionality of parameters for describing the vegetation geometry (h_v, d_0 and z_{0m}).

It is necessary to maintain a rather simple kB^{-1} model in SEBS, in the sense that it has to be easy to implement and to operate with remote sensing observations. Also, the parameterization has to be suitable for describing heat transfer at any scale in the perspective of estimating turbulent heat fluxes over large areas for hydrological and climatological purposes. Taking benefits from the availability of multi-angular remote sensing data at various spatial resolutions, a kB^{-1} model formulated by Jia (2004) is evaluated in this chapter for trying to better characterize the heat transfer.

6.2 Theoretical background

The structure and the conditions of the vegetation have an influence on the thermodynamic properties of heterogeneous land surfaces and their thermal heterogeneity. This is why many kB^{-1} models take in account land surface parameters such as LAI, fractional vegetation cover or even the vegetation height. kB^{-1} parameter is considered as an effective parameter accounting for the distribution of heat sources in a 3D canopy, and the thermal heterogeneity of the canopy has an influence on it (Jia, 2004). It has been demonstrated that kB^{-1} values were strongly related to LAI and the difference of temperature between soil and foliage (Prévot et al., 1994). It is tempting to estimate kB^{-1} from directional radiometric temperature measurements because component temperatures are related to the directional signature of thermal infrared radiance as discussed in Jia (2004).

The simulation study using the SVAT model CUPID presented by Jia (2004), showed that kB^{-1} has a strong dependence on the difference of land surface temperature measured at two zenith view angles θ_v, i.e. nadir ($\theta_v = 0°$) and off-nadir ($\theta_v = 53°$), and on the difference of fractional vegetation cover between the two angles. The simulation study suggested a multiple linear regression that relates kB^{-1} to the anisotropy of a canopy by means of bi-angular observations of surface radiometric temperature and fractional vegetation cover (Jia, 2004) :

$$kB^{-1} = b_1 \frac{T_{rad}(0) - T_{rad}(53)}{f_c(0) - f_c(53)} + b_2 T_{rad}(0) + b_3 f_c(0) + b_0 \qquad (6.1)$$

where b_1, b_2 and b_3 are the regression coefficients, b_0 is the intercept. The simulation data yield : $b_1 = -0.07913$, $b_2 = 0.23193$, $b_3 = -13.07048$, $b_0 = 6.79439$ with $r^2 = 0.98$ for a wide range of Leaf Area Index (LAI), canopy structure, soil water content and meteorological conditions.

Initially, Equation 6.1 was designed by Jia (2004) in order to use the bi-angular observations (nadir and forward) provided by ATSR2. Multi-angular measurements of VNIR reflectances and brightness temperature (T_b) are also provided at the local scale over the Yingke station by the WiDAS sensor. However, its wide-

angle does not reach $\pm 53^{\circ}$ and the viewing angle has to be extrapolated in order to simulate the corresponding values for fractional vegetation cover and brightness temperature. This could be an opportunity for applying Equation 6.1 in the kB^{-1} sequence, in order to perform a new spatial evaluation of experiments 2 and 4 defined in Chapter 5. Unfortunately, no direct ground-based bi- or multi-angular TIR observations were performed at the Yingke station, which will make difficult the temporal evaluation at the AMS scale.

Considering investigations at a larger scale based on remote sensing observations, the kB^{-1} model formulated by Jia (2004) is still applicable, since the recently retired AATSR sensor has specifications and capabilities almost similar to ATSR2. The images acquired by AATSR sensor onboard the former ENVISAT satellite have a swath width of 500 km, which provide 555 pixels across the nadir (0° zenith angle) swath and 371 pixels across the forward (53° zenith angle) swath. The nominal pixel size of an AATSR image is 1×1 km at the center of the nadir swath and 1.5×2 km at the center of the forward swath.

6.3 Evaluation over the Yingke area

In this section, the objective is to adapt experiments 2 and 4 developed in Chapter 5 to apply and evaluate the kB^{-1} parameterization proposed by Jia (2004). Both spatial and temporal validation, respectively at the footprint and at the station scale, are carried out to determine which z_{0m}, and also kB^{-1}, parameterization is the most reliable for estimating turbulent heat fluxes (at least under the conditions of our study area). Procedures to retrieve angular fractional vegetation cover and radiometric temperature retrieval are also detailed.

6.3.1 Characterization of the thermal anisotropy

Soil and vegetation temperature components at the Yingke AMS

Measurements of brightness temperature (T_b) of targets corresponding to 100% soil and 100% vegetation were performed at the Yingke AMS. The radiometric temperature (T_{rad}) of the two components is retrieved from T_b as follow :

$$B(T_b) = \epsilon B(T_{rad}) + (1 - \epsilon) L_w \downarrow \tag{6.2}$$

with B the Planck function :

$$B(T_b) = \sigma T_b^4 \tag{6.3}$$

and ϵ the emissivity, respectively taken as 0.95 for soil and 0.98 for vegetation.

Following Norman et al. (1995), the ensemble directional surface radiometric temperature $T_{rad}(\theta_v)$ is determined by the fraction of the radiometer field of view that is occupied by soil versus vegetation, expressed as :

$$T_{rad}(\theta_v) = \left[f_c(\theta_v)T_c^4 + (1 - f_c(\theta_v))T_s^4\right]^{1/4} \tag{6.4}$$

with T_c and T_s for respectively vegetation canopy temperature and soil temperature. θ_v is the zenith view angle. $f_c(\theta_v)$ is the directional fractional vegetation cover.

The fraction of the field of view of the VNIR sensor occupied by canopy can be related to zenith view angle θ_v and canopy type (Norman et al., 1995; Menenti et al., 2001). Assuming a random canopy with a spherical leaf angle distribution :

$$f_c(\theta_v) = 1 - exp\left[-0.5\frac{LAI}{cos(\theta_v)}\right] \tag{6.5}$$

Considering a 100 by 100 pixel area centered on the Yingke meteorological station, the average LAI value is 2.2. The directional f_c computed with Equation 6.5 gives $f_c(0) = 0.67$ and $f_c(53) = 0.84$.

Figure 6.1 presents the measured soil (T_s) and vegetation (T_c) temperatures and the retrieved $T_{rad}(0)$ and $T_{rad}(53)$. Soil temperature (green curve) presents the highest values and vegetation temperature (blue curve) the lowest ones. The directional radiometric temperature retrieved for nadir (red curve) is located in between these two extremes, and $T_{rad}(53)$ is always in between $T_{rad}(0)$ and T_c since the fraction of vegetation seen at 53° is more higher.

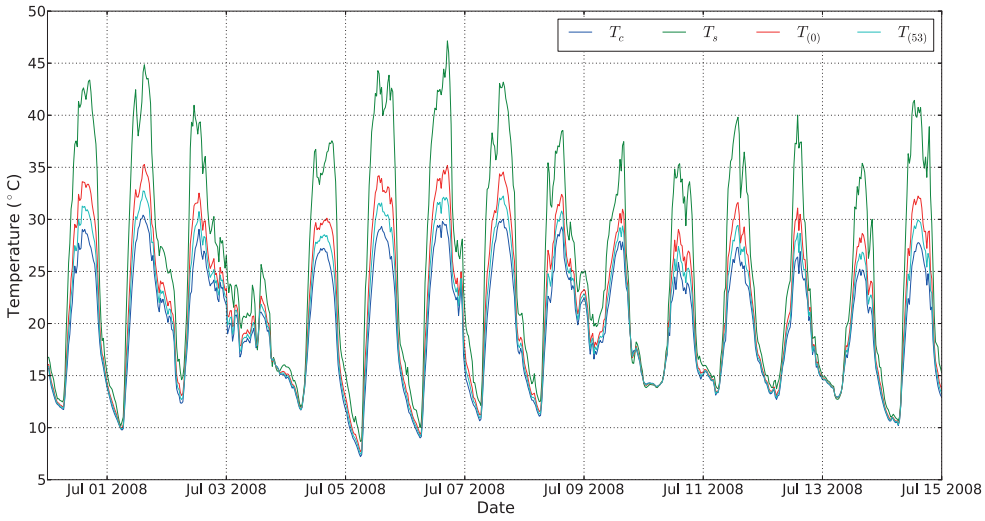

Figure 6.1: Measured vegetation (T_c), soil (T_s), and retrieved $T_{rad}(0)$ and $T_{rad}(53)$ temperatures at the Yingke station from the 30^{th} June to the 14^{th} July 2008.

The WiDAS multi-angular observations

WiDAS instrument is a set of two wide-angle cameras (VNIR & TIR). The VNIR sensor has a field of view of 60°, resulting in maximum zenith view angle of about ±30°. TIR sensor has a FOV of 80°, resulting in maximum zenith view angle of about ±40°. Multi-angular observations of brightness temperature and spectral reflectances are retrieved from the successive wide-angle images acquired by the WiDAS sensor. Usually, five to seven observations of an object with different view angles can be extracted from multiple images acquired over few seconds.

Several targets were identified over the Yingke area: buildings, bare soil, crops (typically corn), orchards, tree rows, and dense crops. For each kind of surface a subset corresponding to 20 by 20 pixels is created in order to compute a mean directional f_c, brightness temperature and zenith view angle. Since some targets such as tree rows or buildings are small or narrow, for these objects a subset of only 10 by 10 pixels is considered.

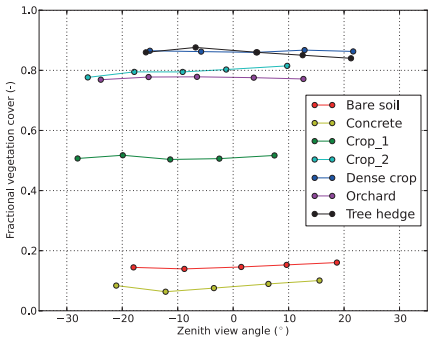

(a) Variation of f_c with θ_v

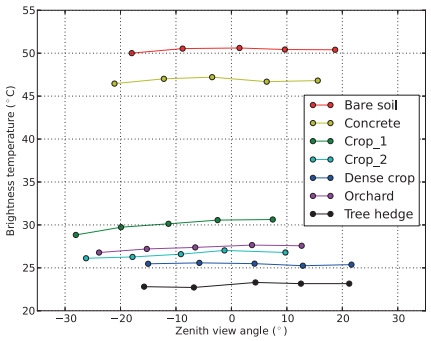

(b) Variation of T_b with θ_v

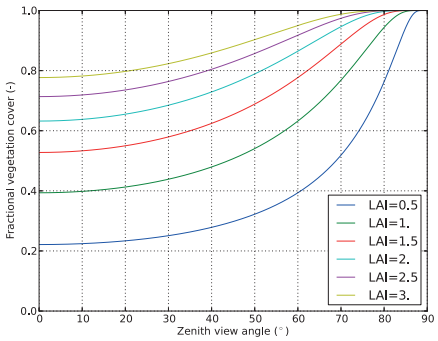

(c) Theoretical variation of f_c with θ_v

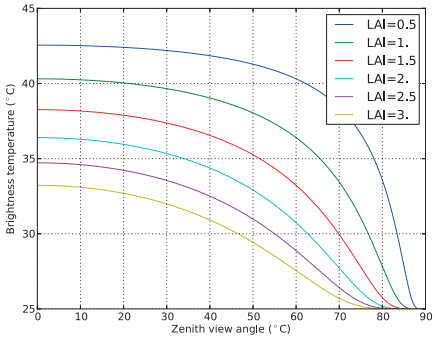

(d) Theoretical variation of T_b with θ_v

Figure 6.2: Observed variation of (WiDAS) fractional vegetation cover (a) and brightness temperature (b) with zenith view angle over the Yingke area and their theoretical behavior (c, d).

Figures 6.2a and 6.2b show that f_c and T_b stay almost constant whatever the view-angle. It is logical for homogeneous targets such as dense crop, bare soil or tree rows, but it is more surprising for mixed surfaces (orchard, crops). In order to explain this observation, fractional vegetation cover is first simulated using Equation 6.5 for different theoretical surfaces with various values of LAI, and then introduced in Equation 6.4 by arbitrarily setting T_c = 25°C and T_s = 45°C. Theoretical curves plotted on Figures 6.2c and 6.2d reveal that in the range 0° to ±30° the variation of fractional vegetation cover and brightness temperature is very weak.

We can conclude that the wide-angle sampled by WiDAS sensor is not sufficient for characterizing the angular variation of f_c and T_b and for extrapolating it to 53°. Also, the first method applied to the station scale can not be applied here, since the TIR sensor resolution does not allow to identify pure pixels for retrieving T_c and T_s. Evaluation of the characterization of anisotropic heat transfer for turbulent heat flux retrieval can only be performed at the AMS scale using synthetic angular radiometric temperatures.

6.3.2 Evaluation of turbulent heat fluxes

Experiments 2 and 4 elaborated in Section 5.4 are adapted here with the substitution of Equation 2.47 with Equation 6.1. The behavior of kB^{-1} parameter with time is represented in Figure 6.3. Contrary to the former kB^{-1} which was forced by the wind variation, the latter kB^{-1} is now forced by the daily fluctuation of land surface temperature. This induces a huge amplitude in values, from nearly 1 to 8 for the 6^{th} July during the daily cycle for instance. Table 6.1 shows the mean and standard deviation calculated for the three kB^{-1} time-series presented in Figure 6.3 but for only the 161 retained occurrences. As expected, the model proposed by Jia (2004) gives higher kB^{-1} values and with clearly more dispersion.

Table 6.1: Mean and standard deviation of kB^{-1} at the Yingke station, following the different scenarii and models.

Model	Mean	Std dev.
kB^{-1} (Su) S_2	5.05	0.17
kB^{-1} (Su) S_4	5.56	0.28
kB^{-1} (Jia)	5.94	1.23

Table 6.2 presents the errors in experiments 2 and 4 for the estimation of turbulent heat fluxes over the 161 occurrences retained in Section 5.4. Experiment

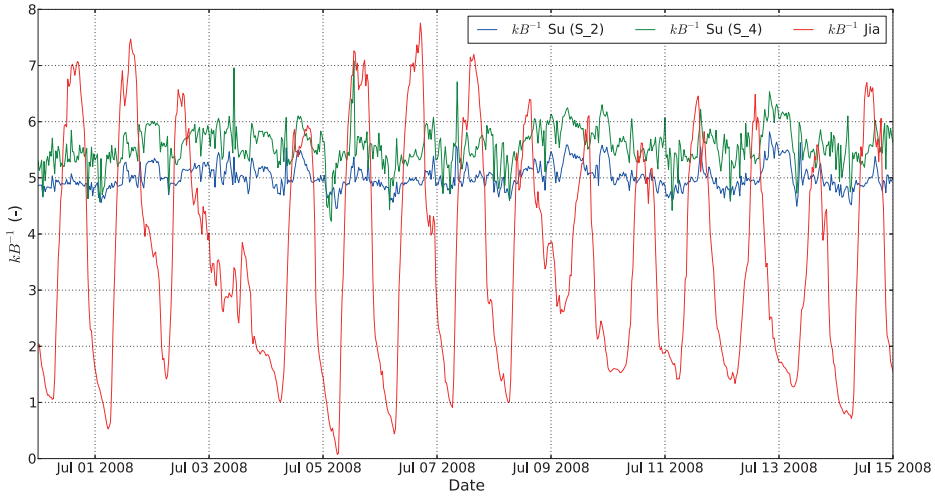

Figure 6.3: Evolution of kB^{-1} from the 30^{th} June to the 14^{th} July 2008 at the Yingke AMS.

4 still slightly gives smaller errors of 2 W/m^2 on H. But results are less precise than these obtained in Section 5.4 with the use of Equation 2.47, since the loss of precision is about 8 W/m^2, except for λE in experiment 2 (4 W/m^2). Error in the partitioning (i.e. Λ) is similar in both experiments. However, experiment 2 still provides similar errors in both sensible and latent heat flux retrieval.

As the new kB^{-1} model presents a large amplitude in its daily evolution, it is interesting to investigate results in more detail. In Table 6.2 a differentiation is made between heat fluxes obtained with a greater and with a lower kB^{-1} value than the original experiments performed in Section 5.4. For both experiments 2 and 4, RMSE decreases to about 4-5 W/m^2 for the retrieval of H and become almost close to the overall errors obtained in Chapter 5 when only greater kB^{-1} are retained. Also the partitioning becomes better and experiment 4 gives the lowest errors. When only lower kB^{-1} are considered, it appears clearly that the most errors in turbulent heat flux retrieval come from these situations. It mainly occurs at the beginning and at the end of the diurnal period when the thermal heterogeneity is reduced or under cloudy sky conditions, as visible in Figure 6.3. This proves that the kB^{-1} model proposed by Jia (2004) is not suitable when soil and vegetation have not really contrasted thermal conditions.

However, when the same occurrences are compared with the initial experiments (Table 6.3), errors still remain smaller with the use of the model proposed by Su et al. (2001). The estimation of turbulent heat fluxes partitioning becomes difficult in the early morning, late evening and under cloud conditions.

It is very difficult to draw conclusions about the real capability of this new kB^{-1} model, given that several surface parameters are synthetically reconstructed,

Table 6.2: RMSE of heat flux densities at the AMS scale with the kB^{-1} model from Jia (2004).

Experiment	λE (W/m^2)	H (W/m^2)	Λ (-)	Nb. of obs.
All occurrences				
2.	38.95	41.60	0.08	161
4.	54.24	39.36	0.09	161
kB^{-1} (Jia) > kB^{-1} (Su)				
2.	45.24	36.26	0.06	126
4.	39.75	35.84	0.05	108
kB^{-1} (Jia) < kB^{-1} (Su)				
2.	77.69	48.93	0.17	35
4.	75.61	45.70	0.15	53

Table 6.3: RMSE of heat flux densities at the AMS scale with the kB^{-1} model from Su et al. (2001).

Experiment	λE (W/m^2)	H (W/m^2)	Λ (-)	Nb. of obs.
kB^{-1} (Jia) > kB^{-1} (Su)				
2.	29.39	35.06	0.05	126
4.	32.50	28.23	0.04	108
kB^{-1} (Jia) < kB^{-1} (Su)				
2.	52.34	29.24	0.13	35
4.	62.77	34.03	0.13	53

in particular $T_{rad}(\theta_v)$. The repetition of a spatial validation at the EC footprint could be the best option, but unfortunately it is impossible to do so at the scale of the Yingke AMS since only one usable flight is available through the WATER project. Nevertheless, this can be easily achieved at a larger scale using AASTR dual-view capabilities.

6.4 Application to the Heihe river basin

The same study was conducted here at the scale of the Heihe river basin. Bi-angular observations are based on an AATSR acquisition performed the 7^{th} July 2008 during an ENVISAT overpass which occurred at 11h51 am (Beijing Time), close to the WiDAS acquisitions. Other cloud-free acquisitions performed in 2008 are also used in order to increase the observations usable for validation. To carry out this study, adequate datasets have to be selected for retrieving land surface parameters and for describing the atmospheric state at the watershed scale. Then several experiments are presented to evaluate alternate kB^{-1} and roughness parameterizations for large scale studies.

6.4.1 Description of datasets

Land surface parameters

The Advanced Along-Track Scanning Radiometer (AATSR) sensor, onboard the former european ENVISAT satellite, was able to provide calibrated and geolocated images of brightness temperature (for the three infrared channels) or reflectance (for the near-visible and visible channels), for a forward and nadir view and with cloud and land identification (Level 1B product ATS_TOA_1P). These data are essential to determine the required variables in Equation 6.1.

Land surface temperature and NDVI are provided by the AATSR Level 2 product (ATS_NR_2P), and released by the European Space Agency (ESA). The definition of the LST algorithm selected for AATSR is based on the work of Prata (2002), who developed algorithms to retrieve land surface temperature from ATSR and AVHRR data. These algorithms are based on radiative transfer theory applied to the exchange of radiation between the surface and atmosphere, and have been subjected to extensive validation using a network of ground-truth sites across Australia.

Other required land surface parameters such as LAI, fractional vegetation cover and albedo correspond to the enhanced products provided by the CEOP-AEGIS project (see Section 3.4). Land surface emissivity is extracted from the

8-day Terra/MODIS product (MOD11A2) delivered by NASA. The ground elevation is given by the global raster 30 arc-second SRTM.

Atmospheric variables

At large scales, SEBS algorithm requires the spatialization of surface and PBL atmospheric variables, since the representativeness of a local measurement over an area such as the Heihe river basin is limited, as discussed in Section 3.3.2. In this study, the Numerical Weather Prediction Model WRF-ARW is used to generate 3D atmospheric fields over the whole watershed, and is fed with NCEP Final Analysis[1] data (1° by 1° grids prepared operationally every six hours). The configuration of two nested domains allows to simulate the surface and atmosphere state at a scale reaching 10 kilometers with a 30 minutes time-step over a 48 hours period, and covering the N-E part of the Tibetan Plateau. Calculations were conducted in two-way nesting between the sectors. The first 24 hours before the targeted date correspond to the spin-up. The grid size of WRF-ARW outputs is consistent with the length scale discussed in Section 2.4, and the time frequency is relatively high in order to better match with AATSR overpasses.

WRF-ARW relies on the execution of several physics models describing surface, atmosphere and interactions between them. A simulation can run up to seven physics models: a model of microphysics, a cumulus parameterization, a surface layer scheme, a land surface model, a planetary boundary layer model and two radiative transfer models (long and shortwave). For each, WRF-ARW allows the choice among several models. The selection of land surface, radiative and PBL models was done according to the validation with ground measurements and radiosoundings. The selected physics models are listed in Table 6.4.

6.4.2 Retrieval procedures

Bi-angular land surface temperature and fractional vegetation cover are extracted from the dual-view images (nadir and forward) acquired by the AATSR sensor. The following procedures are applied to the selected AATSR images acquired the 25^{th} April, 2^{nd} June, 7^{th} July, 24^{th} August and 9^{th} September 2008. These acquisitions were chosen in order to cover different growing stages of the vegetation during cloud-free conditions.

[1]National Centers for Environmental Prediction/National Weather Service/NOAA/U.S. Department of Commerce. 2000, updated daily. NCEP FNL Operational Model Global Tropospheric Analyses, continuing from July 1999. Research Data Archive at the National Center for Atmospheric Research, Computational and Information Systems Laboratory. `http://rda.ucar.edu/datasets/ds083.2`

Table 6.4: List of physics models for WRF-ARW simulations.

Physics	Models
Microphysics	Purdue Lin scheme (Chen and Sun, 2002)
Cumulus Parameterization	Kain-Fritsch (Kain and Fritsch, 1990)
Surface Layer	PX surface layer scheme (Pleim, 2006)
Land Surface Model	Noah LSM (Chen et al., 1996; Chen and Dudhia, 2001; Ek, 2003)
Planetary Boundary Layer	Yonsei University PBL (Hong et al., 2005)
Longwave Radiation	Rapid Radiative Transfer Model (Mlawer et al., 1997)
Shortwave Radiation	MM5 (Dudhia, 1989)

Directional fractional vegetation cover

Jia (2004) proposed to retrieve the directional fractional vegetation cover $f_c(\theta_v)$ from the ATSR2 top of canopy (TOC) reflectances using a stepwise multiple linear regression, as follow :

$$f_c(\theta_v) = a_0(\theta_{s0}, \theta_v) + \sum_{i=1}^{n} a_i(\theta_{s0}, \theta_v)\rho_i(\theta_{s0}, \theta_v, \Delta\varphi) \tag{6.6}$$

where n is the number of channels used, θ_{s0} the solar zenith angle, θ_v the zenith view angle and $\Delta\varphi$ is the relative azimuth angle between sun and satellite direction.

Since ATSR2 and AATSR sensor are identical, both the procedure for atmospheric corrections and $a_0 - a_3$ coefficients in Equation 6.6 are the same in this study as these proposed by Jia (2004).

Directional land surface temperature

Since AATSR brightness temperature delivered by the European Space Agency are top-of-atmosphere (TOA) measurements, it is therefore necessary to correct data from atmospheric effects. An algorithm proposed by Jia et al. (2003b) allows for cloud screening and water vapor column W retrieval from TOA brightness temperatures measured in two thermal infrared channels, centered at 11 and 12 μm. The Split Window (SW) method is then used to retrieve the surface brightness temperature T_b. Following the procedure developed by Becker and Li (1995), Jia (2004) derived a general SW algorithm for ATSR2 (onboard ERS-2) nadir and forward views using the simulation data from MODTRAN4 :

$$T_b(\theta_v) = [a(\theta_v) + b(\theta_v)W] + [c(\theta_v) + d(\theta_v)W]\, T_{b11}(\theta_v) + [e(\theta_v) + f(\theta_v)W]\, [T_{b11}(\theta_v) - T_{b12}(\theta_v)] \tag{6.7}$$

where W is the column water vapor content in the atmosphere retrieved following Li et al. (2003), T_{b11} and T_{b12} are the TOA brightness temperatures measured respectively in channel centered at 11 and 12 μm. The coefficients a to f were determined by a multi-linear regression analysis, separately for ATSR-2 nadir and forward views (Jia, 2004). As sensor specifications of ATSR2 and AATSR are very similar, the same coefficients are used in this study.

The directional radiometric temperatures are then retrieved from $T_b(\theta_v)$ by applying in sequence Equations 6.3 and 6.2. However, the directional top-of-canopy (TOC) emissivity has to be considered and is expressed as follow (Jia, 2004) :

$$\epsilon_c(\theta_v) = f_c(\theta_v)\epsilon_f + [1 - f_c(\theta_v)]\, \epsilon_s + \frac{f_c(\theta_v)\, [1 - f_c(\theta_v)]\, [1 - \epsilon_s]\, [\epsilon_f + \epsilon_s - \epsilon_f \epsilon_s]}{1 - f_c(\theta_v)\, [1 - \epsilon_f - \epsilon_s + \epsilon_f \epsilon_s]} \tag{6.8}$$

with ϵ_s the soil and ϵ_f the vegetation emissivities, still taken as 0.95 and 0.98 respectively.

Roughness length for momentum transfer

Two methods for roughness length retrieval are also applied to the Heihe river basin. The formulation proposed by Moran (1990) based on NDVI (Equation 5.5), commonly implemented in SEBS since it is easily applicable, will be used as a first. The sequence of Equations 5.9, 5.10 and 5.11 formulated by Menenti and Ritchie (1994) is then adapted to compute z_{0m} at the watershed scale. Since it is not possible to characterize precisely the local roughness over large areas, and considering the arid context, Z_{0m} retrieved from Equation 5.10 is replaced by Equation 5.5 in order to take in account the role of vegetation. The terms a and λ in Equation 5.11 are respectively replaced by the amplitude calculated for each DEM pixel in a k by k kernel ($k = 3$) and the width of the kernel (k).

As it was mentioned earlier (see Section 5.3), in order to keep consistency between roughness length, displacement height and vegetation height, Equations 5.6 and 5.7 are used in both cases to compute d_0 and h_v. Figure 6.4 presents the digital elevation model of the Heihe watershed and maps of z_{0m} retrieved following the two methods and their associated distribution of values. Following Moran (1990), rough areas correspond only to irrigated lowlands and vegetated

slopes, which is not consistent with the presence of high mountains in the south of the basin (up to 5,000 m). The adapted formulation of Menenti and Ritchie (1994) allows to combine roughness of vegetated areas with the influence of relief.

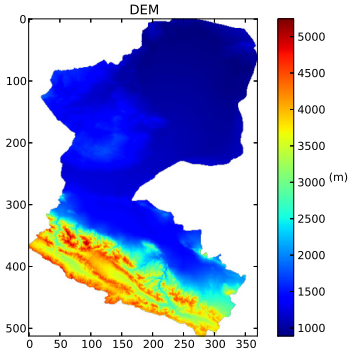

(a) Digital elevation model

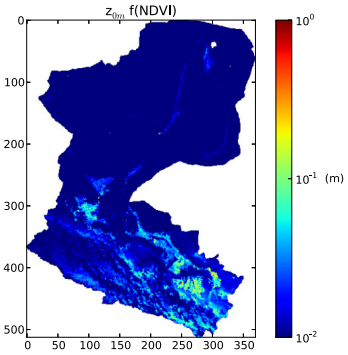

(b) Map of roughness length

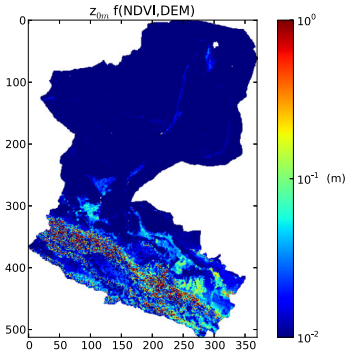

(c) Map of roughness length

Figure 6.4: Digital Elevation Model of the Heihe river basin (a). z_{0m} values retrieved (b) from Moran (1990), and (c) from the adapted formulation of Menenti and Ritchie (1994) for June 2^{nd} 2008.

6.4.3 Evaluation of turbulent heat fluxes

The two methods for kB^{-1} parameterization, and the two for z_{0m} retrieval, are evaluated by comparing EC measurements performed at the Yingke station with estimated heat fluxes for the corresponding AATSR pixel. Several experiments are defined in order to compare all cases.

Design of the different experiments

Following the different methods proposed for z_{0m} retrieval and kB^{-1} parameterization, a set of four experiments for surface energy balance estimation is created. This ensemble of four experiments is applied to five case studies over the Heihe river basin, which are all based on AATSR data. The design of the different experiments is listed below and summarized in Table 6.5 :

- the first experiment is still considered as the "by default" configuration, with z_{0m} assumed to be function of NDVI (Equation 5.5). h_v and d_0 are proportional to roughness length, following Equations 5.6 and 5.7.
- the second experiment is the same as the previous one, but uses the kB^{-1} formulation proposed by Jia (2004) (Equation 6.1).
- the third experiment is based on the effective aerodynamic roughness length estimated following Menenti and Ritchie (1994). Vegetation height and displacement height are still considered as a fraction of z_{0m}.
- the fourth experiment includes kB^{-1} parameterization from Jia (2004) and z_{0m} from Menenti and Ritchie (1994).

Table 6.5: Summary of methods used for the parameterization of z_{0m} and kB^{-1} over the Heihe river basin.

	z_{0m}		kB^{-1}	
	NDVI	*NDVI+DEM*	*Su et al. (2001)*	*Jia (2004)*
1.	✓		✓	
2.	✓			✓
3.		✓	✓	
4.		✓		✓

Results at the Yingke station

Table 6.6 presents the measured and estimated values of net radiation and ground heat flux at the Yingke station for the five dates selected. It has to be noticed that for the 25^{th} April no Rn data is available during ENVISAT overpass, and for the 24^{th} August no Rn and G_0 data were recorded. For the three remaining dates, the relative error in the estimation of net radiation never exceeded $\pm 13\%$ of ground

measurements (+13%, -8.5% and -7.8% respectively). However, the estimation of ground heat flux is still complicated with a systematic overestimation (+79.38 W/m^2, +100.40 W/m^2 and +76.67 W/m^2). For each experiment, this large overestimation of G_0 leads to a large deficit in the at-surface available energy (Rn-G_0) for turbulent heat flux partitioning compared to ground measurements. The overall RMSE for Rn retrieval is 56.83 W/m^2 (over three occurrences) and 92.16 W/m^2 for G_0 (over four occurrences).

Table 6.6: Measured and estimated net radiation (Rn) and ground heat flux (G_0) at the Yingke station.

Date	Variables	Measurements	Estimations
25^{th} April 2008	Rn (W/m^2)	-	499.43
	G_0 (W/m^2)	18.95	127.20
2^{nd} June 2008	Rn (W/m^2)	537.21	606.93
	G_0 (W/m^2)	27.94	107.32
7^{th} July 2008	Rn (W/m^2)	670.14	613.52
	G_0 (W/m^2)	11.00	111.40
24^{th} August 2008	Rn (W/m^2)	-	550.61
	G_0 (W/m^2)	-	102.79
28^{th} September 2008	Rn (W/m^2)	517.40	477.11
	G_0 (W/m^2)	1.17	77.84

Table 6.7 presents the measured values of latent and sensible heat fluxes by the EC system at the Yingke station for the five dates selected. These values are still corrected for the unclosed energy balance according to the Bowen ratio method. Since no Rn data are available for the 25^{th} April and the 24^{th} August, heat flux values are obviously not corrected but the evaporative fraction remains a reliable criteria for evaluation. The correction respectively add +82.5%, +55.1% and +40.4% of the initial sum of turbulent heat fluxes (H+λE) for the 2^{nd} June, 7^{th} July 2008 and 28^{th} September. The first percentage represents a large correction. Also, flux densities measured the 25^{th} April 2008 appear very low when sky conditions are supposed to be rather clear, at least in the line of sight between the sensor and the target. Rn measurements on this date would have been very useful for verifying the origin of such low values.

Table 6.8 presents the estimated values of latent and sensible heat fluxes, evaporative fraction, roughness length for momentum and heat transfer and their related kB^{-1} parameter at the Yingke station for the five dates selected.

The 25^{th} April 2008, the heat flux density corresponding to $H + \lambda E$ is largely

Table 6.7: Measured and corrected heat flux densities at the Yingke station at the time corresponding to AATSR acquisitions.

Date	Variables	Measured	Corrected	Variation
25^{th} April 2008	λE (W/m^2)	97.15	-	-
	H (W/m^2)	124.31	-	-
	Λ (-)	0.44	-	
2^{nd} June 2008	λE (W/m^2)	126.73	231.45	+104.72
	H (W/m^2)	152.40	277.78	+125.38
	Λ (-)	0.45	0.45	
7^{th} July 2008	λE (W/m^2)	388.53	602.78	+214.25
	H (W/m^2)	36.33	56.36	+20.03
	Λ (-)	0.91	0.91	
24^{th} August 2008	λE (W/m^2)	414.63	-	-
	H (W/m^2)	61.52	-	-
	Λ (-)	0.87	-	
28^{th} September 2008	λE (W/m^2)	155.12	217.81	+62.69
	H (W/m^2)	212.62	298.41	+85.79
	Λ (-)	0.42	0.42	

overestimated since no energy balance closure (EBC) correction was applied to measurements (+150.77 W/m^2). The partitioning is overestimated by respectively +0.30 and +0.29 in experiments 1 and 2, but H is only underestimated by -28.39 W/m^2 and -23.91 W/m^2, with obviously most of the errors transferred to λE. Concerning experiments 3 and 4, it is clear that the proposed formulation for z_{0m} based on Menenti and Ritchie (1994) does not affect roughness values due to the terrain flatness and estimated fluxes are identical. Also, the estimated kB^{-1} in experiments 2 and 4 is nearly 8 times greater than the value retrieved from Equation 2.47, but resulting turbulent heat fluxes and partitioning are similar. In this case, the estimation of sensible heat flux is less sensitive to the particular kB^{-1} value. This is the result of a particular combination between the reference height (i.e. PBL level), the roughness length for momentum, the roughness length for heat transfer and the stability corrections.

The 2^{nd} June 2008, experiment 1 overestimates the evaporative fraction (+0.20), which induces large errors in H (-104.94 W/m^2) and λE retrieval (-95.33 W/m^2), while experiment 2 is getting worse with a Λ = 0.79 and its associated errors.

The 7^{th} July 2008, the evaporative fraction is well captured by experiment 1 (-0.03) and H is also well estimated (+4.11 W/m^2), when λE is clearly underestimated (-161.13 W/m^2) due to the difference between estimated and measured at-surface available energy. The increase of kB^{-1} in experiment 2 (4 times) is too important an leads to a decrease of z_{0h} and consequently to a raise of H (+37.2 W/m^2).

The 24^{th} August 2008, experiment 2 is very effective to retrieve a fair partitioning with a Λ equal to 0.85 (-0.02). Sensible heat flux is also well estimated (+7.94 W/m^2), like λE (-36.29 W/m^2) since the measured and estimated at-surface available energy are in a good agreement (about 40 W/m^2 of difference), even without closure correction. With an evaporative fraction estimated at 0.73, experiment 1 nearly overestimates two times H (+59.14 W/m^2).

On 28^{th} September 2008, no experiment captures the observed partitioning (+0.39 and +0.33). As a consequence, the estimation of sensible heat flux is erratic (-222.91 W/m^2 and -200.52 W/m^2), as for latent heat flux (+105.96 W/m^2 and +83.57 W/m^2).

It appears clearly that the use of the modified Equation 5.11 to retrieve z_{0m} has no influence on results for the estimation of turbulent heat fluxes. Values are rigorously equivalent since the Yingke area corresponds to an open flat terrain and roughness is only due to vegetation. Results might be different if the station had been located in a steep area, but usually these landscapes are avoided for heat flux measurements, while they are important in this region.

During the WATER intensive observation period, different hydrological systems were studied and in particular the mountainous Babao river basin with the A'rou station. This station located in an open valley, but maybe be sufficiently

Table 6.8: Results of estimated heat flux densities and roughness length at the AATSR pixel scale corresponding to Yingke station.

Exp.	λE (W/m^2)	H (W/m^2)	Λ (-)	z_{0m} (m)	kB^{-1} (-)	z_{0h} (m)
			25^{th} April 2008			
1.	276.31	95.92	0.74	0.013	2.41	0.0012
2.	271.83	100.40	0.73	0.013	18.69	$9.8{\cdot}10^{-11}$
3.	276.32	95.92	0.74	0.013	2.41	0.0012
4.	272.83	100.40	0.73	0.013	18.69	$9.8{\cdot}10^{-11}$
			2^{nd} June 2008			
1.	326.78	172.84	0.65	0.122	5.82	0.0004
2.	397.47	102.15	0.79	0.122	15.83	$1.6{\cdot}10^{-8}$
3.	326.62	173.00	0.65	0.123	5.82	0.0004
4.	397.39	102.23	0.79	0.123	15.83	$1.6{\cdot}10^{-8}$
			7^{th} July 2008			
1.	441.65	60.47	0.88	0.136	3.50	0.0041
2.	408.46	93.66	0.81	0.136	13.69	$1.5{\cdot}10^{-7}$
3.	441.67	60.45	0.88	0.136	3.50	0.0041
4.	408.47	93.65	0.81	0.136	13.69	$1.5{\cdot}10^{-7}$
			24^{th} August 2008			
1.	327.16	120.66	0.73	0.108	3.79	0.0024
2.	378.34	69.48	0.85	0.108	12.84	$2.8{\cdot}10^{-7}$
3.	327.12	120.70	0.73	0.108	3.79	0.0024
4.	378.32	69.50	0.85	0.108	12.84	$2.8{\cdot}10^{-7}$
			28^{th} September 2008			
1.	323.77	75.50	0.81	0.085	5.21	0.0005
2.	301.38	97.89	0.75	0.085	12.23	$4.1{\cdot}10^{-7}$
3.	323.79	75.48	0.81	0.085	5.21	0.0005
4.	301.39	97.88	0.75	0.085	12.23	$4.1{\cdot}10^{-7}$

influenced by the surrounding mountains, can be an ideal candidate for further investigations about large scale z_{0m} parameterization.

Results at the A'rou station

Table 6.9 presents the net radiation and ground heat flux measured and estimated at the A'rou station. The two first dates initially selected had to be removed because of some gaps in the recorded data and to only retain SEBS experiments on the 7^{th} July, 24^{th} August and 28^{th} September 2008. It is particularly interesting to see how the solution of SRB is accurate for the A'rou station, with a relative error of -6.9% the 7^{th} July and only +1.2% and +0.6% the 24^{th} August and 28^{th} September respectively. Also, an error of +72 W/m^2 in the estimation of ground heat flux is observed for the first date, which then decreases to +21 W/m^2 and +11 W/m^2 for the two other dates. The overall RMSE for Rn retrieval is 25.28 W/m^2 and 41.66 W/m^2 for G_0.

Results of estimated net radiation for A'rou station remain extremely impressive taking into account the scales which are compared here, e.g. the field of view of a pyranometer face to the resolution of a radiative balance obtained by merging kilometric VNIR/TIR observations with NWPM outputs. It also raises the question about the ability of Equation 2.5 to retrieve a reliable ground heat flux.

Table 6.9: Measured and estimated net radiation (Rn) and ground heat flux (G_0) at the A'rou station.

Date	Variables	Measurements	Estimations
7^{th} July 2008	Rn (W/m^2)	628.00	584.88
	G_0 (W/m^2)	24.42	96.32
24^{th} August 2008	Rn (W/m^2)	567.00	574.03
	G_0 (W/m^2)	32.17	53.92
28^{th} September 2008	Rn (W/m^2)	480.87	483.82
	G_0 (W/m^2)	61.19	72.31

Table 6.10 presents the measured and corrected values of latent and sensible heat fluxes for the three dates retained at the A'rou station. The sum of measured turbulent heat fluxes is always stable and ranging between 401.83 and 447.21 W/m^2. However, the theoretically available energy by subtracting the measured G_0 to Rn is always higher than the sum of EC flux measurements, with a relative correction of +36.1%, +19.6% and +4.4% respectively. This latter percentage is interesting and shows that the closure of energy budget sometimes nearly occurs in ground measurement.

Table 6.10: Measured and corrected heat flux densities at the A'rou station for the time corresponding to AATSR acquisitions.

Date	Variables	Measured	Corrected	Variation
7^{th} July 2008	λE (W/m^2)	346.57	471.55	+124.98
	H (W/m^2)	97.05	132.03	+34.98
	Λ (-)	0.78	0.78	
24^{th} August 2008	λE (W/m^2)	306.61	366.32	+59.71
	H (W/m^2)	140.60	168.51	+27.91
	Λ (-)	0.69	0.69	
28^{th} September 2008	λE (W/m^2)	201.09	210.05	+8.96
	H (W/m^2)	200.74	209.63	+8.89
	Λ (-)	0.50	0.50	

Table 6.11 presents the estimated values of latent and sensible heat fluxes, evaporative fraction, roughness length for momentum and heat transfer and their related kB^{-1} parameter at the A'rou station for the three dates selected.

The 7^{th} July 2008, experiment 1 slightly underestimates the evaporative fraction (-0.08 with +13.49 W/m^2 for H) and the increase of z_{0m} in experiment 3 leads to a larger underestimation of Λ (-0.11 with +31.08 W/m^2 for H). Experiments 2 and 4 have larger ovrestimations of H (+44.86 W/m^2 and +41.95 W/m^2) with a lower Λ (-0.14). The change in z_{0m} does not affect the portioning since the variation in z_{0h} is vey weak. This is explained by the high value of kB^{-1} and its stability face to z_{0m}. As it is not the case in experiments 1 and 3, a change of roughness length for momentum induces larger variations in the partitioning.

The 24^{th} August 2008, despite the large increase of kB^{-1} parameter between experiments 1 and 2 (nearly 5 times greater), the overestimation in sensible heat flux falls from +143.91 W/m^2 to + 35.45 W/m^2. The change in z_{0m} increases this gap by +186.46 W/m^2 in experiment 3 and only +23.28 W/m^2. Experiment 4 is very close to the corrected measurement with an evaporative fraction of 0.63 (-0.06) and flux densities are in a good agreement due to a weak error in Rn estimation (+7 W/m^2).

On 28^{th} September 2008, despite the increase of z_{0m} between experiments 1 and 3, the evaporative fraction also increases from 0.60 to 0.62 (+0.1 and +0.12). The estimated H goes from -45.59 W/m^2 compared to the corrected measurement, to -50.77 W/m^2. Between experiments 2 and 4, Λ also increases slightly from 0.55 (+0.5) to 0.56 (+0.6). However, the deviation in H remains good : -25.44 W/m^2 and -27.73 W/m^2 respectively. Once again, the weak difference in the net radiation (+3 W/m^2) gives good agreements for both latent and sensible heat flux

estimation.

Table 6.11: Results of estimated heat flux densities and roughness length at the AATSR pixel scale corresponding to A'rou station.

Exp.	λE (W/m^2)	H (W/m^2)	Λ (-)	z_{0m} (m)	kB^{-1} (-)	z_{0h} (m)
			7^{th} July 2008			
1.	343.04	145.52	0.70	0.178	3.31	0.0065
2.	311.67	176.89	0.64	0.178	21.95	$5.3{\cdot}10^{-11}$
3.	325.45	163.11	0.67	0.282	3.33	0.0101
4.	314.58	173.98	0.64	0.282	21.95	$8.3{\cdot}10^{-11}$
			24^{th} August 2008			
1.	207.69	312.42	0.40	0.296	5.70	0.0009
2.	316.14	203.97	0.61	0.296	27.80	$2.5{\cdot}10^{-13}$
3.	165.15	354.97	0.31	0.457	5.71	0.0015
4.	328.32	191.79	0.63	0.457	27.80	$3.8{\cdot}10^{-13}$
			28^{th} September 2008			
1.	248.31	163.20	0.60	0.098	6.18	0.0002
2.	228.16	183.35	0.55	0.098	22.48	$1.7{\cdot}10^{-11}$
3.	253.49	158.02	0.62	0.160	6.19	0.0003
4.	230.45	181.06	0.56	0.160	22.48	$2.7{\cdot}10^{-11}$

6.4.4 Discussion

In order to have a better vision of the accuracy of each scenario for estimating turbulent heat fluxes, Table 6.12 presents RMSE between observed and estimated flux densities at the Yingke station. Only errors for experiments 1 and 2 are presented since there is no sensible difference in results with experiments 3 and 4. However, a distinction is done between RMSE computed before and after EBC correction for the ground measurements due to the large imbalance.

Considering the three dates for which the EBC correction was performed, Table 6.12 reveals that RMSE are globally very large (up to 100 W/m^2). For scenario 1, errors in H retrieval reach 142.27 W/m^2 and a little bit less for λE with 124.20 W/m^2, while errors are similar for H (155.40 W/m^2) and λE (155.25 W/m^2) when applying scenario 2. Due to the low recorded values of G_0 and the great difference

Table 6.12: RMSE of estimated heat fluxes using AATSR data at the pixel corresponding to the Yingke station.

	Corrected		Uncorrected	
Variables	Experiment 1	Experiment 2	Experiment 1	Experiment 2
λE (W/m^2)	124.20	155.25	149.02	159.32
H (W/m^2)	142.27	155.40	69.43	62.63
Λ (-)	0.254	0.280	0.246	0.252

between $Rn - G_0$ and $H + \lambda E$, the correction distributed to heat fluxes is large.

If only the non-corrected measurements are considered for the five dates, RMSE in H is 69.43 W/m^2 and 62 W/m^2 respectively for experiments 1 and 2. From this point of view, the use of kB^{-1} proposed by Jia (2004) becomes the best solution to parameterize sensible heat flux. However, large errors still remain on latent heat flux with 149.02 W/m^2 and 159 W/m^2, explained by the large uncertainty in partitioning (0.246 and 0.252).

Table 6.13 presents RMSE between observed and estimated turbulent heat fluxes at the A'rou station. Errors are here presented following the four experiments since the z_{0m} retrieval based on Menenti and Ritchie (1994) provides significant changes in this mountainous region. A separate comparison is still conducted between before (Table 6.13a) and after (Table 6.13b) the correction for the non-closure of the SEB.

Table 6.13: RMSE of estimated heat fluxes using AATSR data at the pixel corresponding to the A'rou station. Tables 6.13a and 6.13b present respectively errors before and after correction of energy balance closure for ground measurements.

(a)

Variables	Experiment 1	Experiment 2	Experiment 3	Experiment 4
λE (W/m^2)	63.32	26.09	87.94	28.03
H (W/m^2)	105.33	59.70	131.84	54.55
Λ (-)	0.183	0.097	0.238	0.095

(b)

Variables	Experiment 1	Experiment 2	Experiment 3	Experiment 4
λE (W/m^2)	119.92	97.31	145.72	93.98
H (W/m^2)	87.65	36.33	113.13	32.24
Λ (-)	0.183	0.097	0.238	0.095

Without corrections, errors in estimating λE for experiments 2 and 4 are very low (26.09 W/m^2 and 28.09 W/m^2). RMSE slightly increases with the raise of z_{0m} but it is beneficial for H since errors reduce from 59.70 W/m^2 to 54.55 W/m^2 with a better flux partitioning. For experiments 1 and 3, it is the opposite situation with larger initial errors for λE (63.32 W/m^2) and H (105.33 W/m^2) retrieval, which then increase to 87.94 W/m^2 and 131.84 W/m^2 respectively.

When EBC correction is applied at the A'rou station, RMSE in λE retrieval becomes for each scenario larger than H retrieval. The transition from experiment to experiment 3 still increases errors (87.65 W/m^2 to 113.13 W/m^2 for H), while they decrease from experiment 2 to experiment 4 (36.33 W/m^2 to 32.24 W/m^2 for H).

In both cases, the increase in of z_{0m} improves heat flux retrieval from experiment 2 to 4, and degrades it from experiment 1 to 3. This can be explained by the fact that Equation 2.47 provides relatively low kB^{-1} values and thus z_{0h} ones are rather high. Therefore, the reverse reasoning applies for Equation 6.1. So, a change in z_{0m} will affect the calculation of external resistances and stability functions in experiments 1 and 3. The kB^{-1} model presented by Jia (2004) allows SEBS to be less sensitive to variations of roughness length for momentum. This aspect is interesting because the formulation based on Moran (1990) is suspected to overestimate z_{0m}, as seen in Chapter 5. The adapted roughness length retrieval presented in this study provides a rough basis as a function of the surrounding relief, which will seasonally increase following the vegetation activity. In this sense, this formulation will also obviously sometimes overestimate the local roughness (i.e. for low and dense vegetation).

Also, the accuracy of measurement has to be taken into consideration. At the A'rou station, RMSE in G_0 retrieval is 41.66 W/m^2 when it reaches 92.16 W/m^2 at the Yingke station. Since fractional vegetation coverage is higher at the A'rou station, the estimated ground heat flux is obviously reduced. However, the difference in measured ground heat fluxes is large and values observed at the Yingke station are still low around noon, while higher flux densities like these measured at A'rou are expected. This has also an impact the EBC correction in the validation procedure as demonstrated before. This problem was raised in Chapter 5 already. For large scale studies, the estimation of ground heat flux cannot be specifically adjusted for every land cover type, and is already interpolated following the fraction of green vegetation in Equation 2.5.

A validation based on LAS measurements could be more consistent in terms of flux footprint compared to the area of an AATSR pixel. In terms of energy balance closure, however it is more hazardous to perform a correction such as what was done on EC measurements, since the contributing area is more extended for LAS systems compared to the footprint of radiative balance measurements. Beyond ground measurement representativeness and quality, there is also the real diffi-

culty to parameterize kB^{-1} for any circumstances. It remains a purely theoretical parameter since z_{0h} is not a physically based quantity. But its parameterization is necessary because inherent to the single-source bulk transfer approach.

6.5 Conclusion

The evaluation attempted over the Yingke station proved that the WiDAS sensor is not suitable for the application of Equation 6.1 to parameterize kB^{-1}. Thermal anisotropy of heterogeneous land surface is by definition difficult to be observed, and this evaluation should be performed with a real two-angle VNIR and TIR sensor. At the scale of the AMS, the synthetic retrieval of the directional temperature and fractional vegetation cover does not allow to precisely evaluate the characterization of heat transfer by this kB^{-1} model. However, the CFD-based roughness length for momentum transfer (experiment 4) proved again to be the most suitable for the estimation at least of sensible heat flux, but not for a correct partitioning between turbulent heat fluxes.

At a lager scale, and for relatively flat terrain, the proposed z_{0m} formulation does not affect estimation of turbulent heat fluxes but improves accuracy in calculations when used jointly with the kB^{-1} parameterization formulated by Jia (2004) over rough areas. On the other hand, the combination of a such roughness retrieval with the kB^{-1} model proposed by Su et al. (2001) does not allow to characterize heat transfer better. However, the different experiments were applied on a limited number of case studies. A long-term comparison may provide sufficient occurrences for a strict evaluation.

Nevertheless, some limitations remain with the use of kB^{-1} model formulated by Jia (2004). i) This model is only valid for sparse canopy structure and contrasted thermal conditions, and does not apply for bare soils and for homogeneous canopies. ii) It requires dual-view capabilities which represents a technical limitation. iii) The difference of nominal pixel resolution and so of footprint leads to the introduction of errors by resampling. Otherwise, in the case of less thermal heterogenous land surfaces and/or absence of such bi-angular data, the kB^{-1} model developed by Su et al. (2001) remain a good method for the parameterization of heat transfer. Also, due to the absence of DSM, variables such as d_0 and h_v are necessarily calculated from z_{0m} and the linearity required for kB^{-1} is kept even if this concept is rather wrong for heterogeneous land surfaces as seen in Chapter 5.

Currently, such regional studies based on AATSR dual-view capabilities are no longer possible in an operational context. ENVISAT satellite is retired since 2012 and only archives are usable, but considerably extended due to ATSR and ATSR2. The coming next ESA mission Sentinel-3, in the frame of the Copernicus

programme, will launch a pair of satellite which comprise each the Sea and Land Surface Temperature Radiometer (SLSTR) sensor, the successor of AATSR with the same bi-angular capability. This mission will enable a short revisit time of less than one day for SLSTR at the equator with a near-realtime data service, which will paves the way to operational applications.

Chapter 7

Meso-scale surface energy balance calculation

7.1 Introduction

In the perspective of large scale studies, the land surface geometrical and thermal properties for momentum and heat transfer cannot be characterized in detail at the (at least) 1 km^2 spatial resolution, and the SEBS-based parameterization of turbulent heat fluxes necessarily relies on rough approximations. However, while the change of scale leads to a decreasing spatial resolution, it allows to increase the temporal resolution for estimates of turbulent heat fluxes. This is a significant advantage when considering an operational context for the production of evapotranspiration time-series. In this chapter, the ability of parameterization schemes such as SEBS to estimate actual evapotranspiration up to a daily basis, and despite the absence of detailed and reliable geometrical surface characterization, will be evaluated.

As presented in the previous chapters, the parameterization of the surface energy balance requires to integrate several key bio-geophysical and atmospheric variables, whose spatial and temporal scales may be different. Therefore, it is required to not only implement the algorithms themselves, but also a set of tools that allows to manage such a heterogeneity of data (i.e. file formats, projections, resampling). The processing chain consists of several components as illustrated in Figure 7.1. Atmospherical fields, land surface parameters and LST gap-filled are datasets provided in the frame of the CEOP-AEGIS project and they are described in Sections 3.3 and 3.4. The availability of such products thus allows to compute a daily evapotranspiration rate over the entire Tibetan Plateau, spatially and temporally continuous on a daily basis over the period 2008-2010.

Beyond the technical considerations, SEBS algorithm itself has also to deal

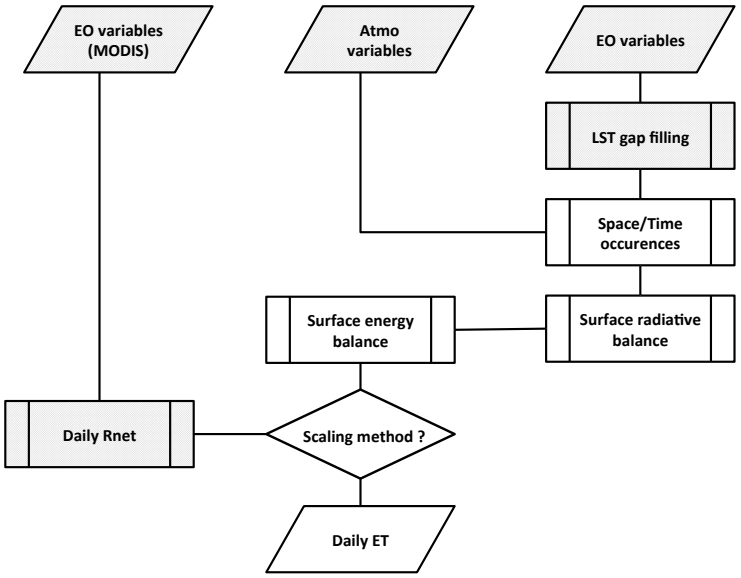

Figure 7.1: Processing overview of the daily ET estimation. Shaded boxes correspond to the input data or intermediate products provided in the frame of the CEOP-AEGIS project.

with the spatial and temporal heterogeneities. As discussed in Section 2.4, the horizontal length scale for applying the Bulk Atmospheric Similarity (BAS) theory to regional studies with NWPM outputs was never considered in the initial design of SEBS. An attempt for filling this gap was presented by Jia et al. (2003b), but this issue was deeply treated by Colin (2006). In this study, considering both the scale of the involved processes and the optimization of computing time, it has been decided to follow this latter work. Moreover, for practical reasons only one turbulent heat flux estimation is performed for each day of the 3-years period. It implies to implement a temporal scaling strategy for extrapolating instantaneous flux densities to a daily evapotranspiration rate.

7.2 From SEBS to Multi-Scale SEBS

The concept of using the Atmospheric Surface Layer (ASL) similarity for surface layer scaling and the Bulk Atmospheric Similarity (BAS) for regional scaling was proposed in SEBS, but the corresponding horizontal scales are not defined. The Monin-Obukhov Similarity (MOS) stability correction functions applies for momentum and heat transfer between the land surface and a reference height in the atmospheric surface layer, which is often the case when very-high spatial reso-

lution images are available for local estimate of heat fluxes in combination with meteorological variables measured in the near-surface layer. When using satellite images with a coarser resolution in which the pixel-wise extent is usually larger, the land surface characterized by effective land surface parameters is interacting and in equilibrium with air flow. Such interaction is linked by bulk similarity theory (Brutsaert, 1999) and meteorological variables measured (or modeled) at a higher level (i.e. PBL height) are therefore required. The variables related to the state of the PBL are representative of a large area on the ground, that is assumed to be at least ten times the PBL height (Jia et al., 2003b). A calculation grid size corresponding only to the pixel size of the highest resolution remote sensing data is therefore irrelevant for the solution of surface energy balance, considering the scale of atmospheric processes.

The Multi-Scale Surface Energy Balance System (MSSEBS) proposed by Colin (2006) was developed to preserve consistency of physical variables with corresponding characteristic spatial scale (Table 7.1). As illustrated on the Figure 7.2, MSSEBS combines VNIR and TIR images (with various spatial resolution depending on the sensor) for the surface radiative budget calculation, and atmospheric variables for stability corrections calculations, to provide scale consistent aerodynamic resistances and turbulent heat flux values. Each step of calculation uses the adequate scale. The highest resolution available is used for surface vegetation variables estimates (e.g. 1 km for MODIS). The radiative balance combines both medium resolution of VNIR products and lower resolution of the TIR data (e.g. 5 km for FY-2). Net radiation and roughness length for momentum can be aggregated to a new grid size relevant for atmospheric stability calculations, following the flux conservation principle. The obtained low resolution stability parameters are then downscaled to the initial high resolution, with either linear or cubic convolution extrapolation methods, and introduced in the calculation of aerodynamic resistances. Considering that daily MSSEBS calculations are performed around noon, a mean PBL height of about 2,000 m was determined from GRAPES data, which sets the grid size for atmospheric stability calculations to 20 km.

Initially, the MSSEBS algorithm proposed by Colin (2006) is purely based on the SEBI concept presented in Section 2.3, which aims at first estimating latent heat flux and at retrieving sensible heat flux as a residual of energy balance equation. MSSEBS is implemented here following the approach of Su (2002) detailed in Section 2.4 for the calculation of sensible heat flux. Considering the difficulty to accurately retrieve z_{0m}, kB^{-1} parameter and thus z_{0h} as demonstrated in Chapters 5 and 6, this method minimizes errors by avoiding to compute a dry external resistance $r_{ah,d}$.

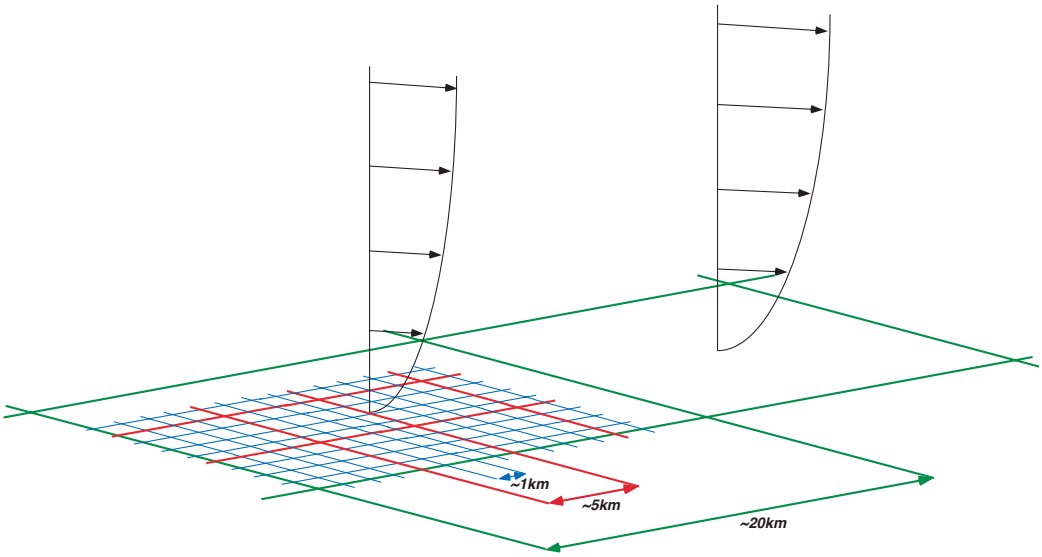

Figure 7.2: The MSSEBS approach consists in mixing calculation grid scales from the finest resolution available to typical TIR band resolution, and atmospheric length scale for atmospheric processes. In our case, this leads to a grid size of 1, 5 and 20 kilometers (adapted from Colin et al. (2006)).

Table 7.1: Summary of the respective temporal and spatial scales for input variables.

Variables	Temporal scale	Spatial scale
GRAPES vars.	Half-hourly	30 km
LST	Hourly	5 km
LSE	Daily	5 km
Albedo	8-days	1 km
NDVI	8-days	1 km
LAI	8-days	1 km
f_c	Daily	1 km
DEM	-	1 km

7.3 Temporal scaling of daily evapotranspiration

A fundamental problem in using remote sensing to estimate local or regional evapotranspiration (ET) involves the scaling of instantaneous latent heat flux (derived from remotely sensed surface temperature at a single time of day) to daily ET (the 24h total). Several scaling methods have been proposed that essentially rely on a ratio of latent heat flux and some other component that is available on an hourly basis, such as incoming energy or reference ET (Colaizzi et al., 2006; Li et al., 2009c). During clear skies and in the absence of significant advected energy, daytime plots of these components will be nearly sinusoidal, and their ratio have been observed to remain fairly constant (Crago, 1996b). This would allow estimation of daily ET (ET_d) considering that the contribution of nighttime ET is relatively small. In this way, Jackson et al. (1983) related the ratio between instantaneous ET and its daily value ET_d, to the diurnal trend of solar irradiance with the following equation :

$$\frac{ET_d}{ET_i} = \frac{R_{sd}}{R_{si}} = 2\,\frac{N}{\pi \cdot \sin(\pi \frac{t}{N})} \tag{7.1}$$

where subscripts d and i respectively indicate the daily total and instantaneous values, R_s the incoming solar radiation, N is the total time from sunrise to sunset (h) and t is the time elapsed from sunrise to the calculation timestamp (h). ET_d is expressed in mm/day and ET_i in mm/hour.

Also, studies have shown that due to a relative constant G_0/Rn ratio and evaporative fraction during the diurnal period, daily overall evapotranspiration (ET_d) can be expressed as (Suttleworth et al., 1989; Sugita and Brutsaert, 1991; Brutsaert and Sugita, 1992; Crago and Brutsaert, 1996; Crago, 1996a,b) :

$$ET_d = \Lambda\,[Rn_a(1 - G_0/Rn)]\,\frac{3600\ N}{2.4 \cdot 10^6} \tag{7.2}$$

where Λ is the evaporative fraction, Rn and G_0 are respectively the instantaneous net radiation and soil heat flux and Rn_a the diurnal mean net radiation.

This latter term is provided as an enhanced product in the frame of the CEOP-AEGIS project (Menenti et al., 2010). The main guidelines of the underlying net radiation model are based on the work of Iqbal (1983). Shortwave and longwave net radiation are estimated for clear sky as well as for cloudy conditions. In the computation of solar radiation, a digital elevation model and broadband atmospheric radiative transmittance factors are used in order to account for the topographic and atmospheric transmissivity effects. The model provides images, at a square kilometer spatial resolution and on a daily basis, of the instantaneous net radiation and its four components for all skies over Tibet. The sinusoidal model to estimate the diurnal cycle of net radiation proposed by Bisht and Bras (2010) is

used to estimate the daily mean net radiation (Rn_a) from the instantaneous value, exactly in the same manner as in Equation 7.1. In this model, the daily mean net radiation, in terms of the instantaneous all skies net radiation (Rn) can be obtained using the local satellite overpass time as well as local sunrise and sunset time. The estimation is expressed as :

$$Rn_a = 2\,\frac{Rn}{\pi \cdot \sin(\pi \frac{t}{N})} \tag{7.3}$$

The model has been implemented using MODIS products and data coming from other sources. The data used to estimate the radiative transmittance factors for the net solar radiation estimation are derived from daily atmospheric Terra/MODIS products, as well as the clouds parameters used for all skies conditions computations. The albedo, land surface temperature and emissivity used in the upward shortwave and longwave computations respectively comes from MCD43B3 combined MODIS product and from the FY-2 gap-filled data (Ghafarian et al., 2012). The near-surface air temperature, and air humidity data used to compute the downwelling longwave radiation are measurements extracted from specific databases, e.g. the National Climatic Data Center (NCDC) of the NOAA (Bastiaanssen et al., 2012). Then, the meteorological distribution model described by Thornton et al. (1997) is used to convert point data to spatial meteorological data. Some missing data can be found within MODIS products, especially in the atmospheric optical depth product. A gap-filling plan based on spatial and temporal filling was applied before providing the data as input for the net radiation computation.

7.4 Evaluation of heat flux time-series

The 3-years time-series of daily heat fluxes has been evaluated for the pixels corresponding to the Nagqu, Namco, Linzhi and Qomolangma stations. More details about the acquisition and evaluation of SRB and SEB ground measurements performed at these four stations are available in Babel et al. (2011). The complete dataset (2008-2010) represents 1,097 calculations performed at a timestamp corresponding more or less to the local solar noon (2 pm Beijing Time). Table 7.2 presents RMSE between observed and estimated net radiation (Rn), ground heat flux (G_0), latent heat flux (λE), sensible heat flux (H), hourly (ET_h) and daily (ET_d) evapotranspiration. The associated subscripts (a), (b) and (c) refer to the RMSE computed for respectively all skies, clear sky and cloudy sky conditions. The two ET_d scaling methods are distinguished as follows : $ET_d\ ratio$ refers to the scaling computed using the evaporative fraction and the G_0/Rn ratio, and $ET_d\ sine$ refers to method based on a sine function. Sky conditions are only rep-

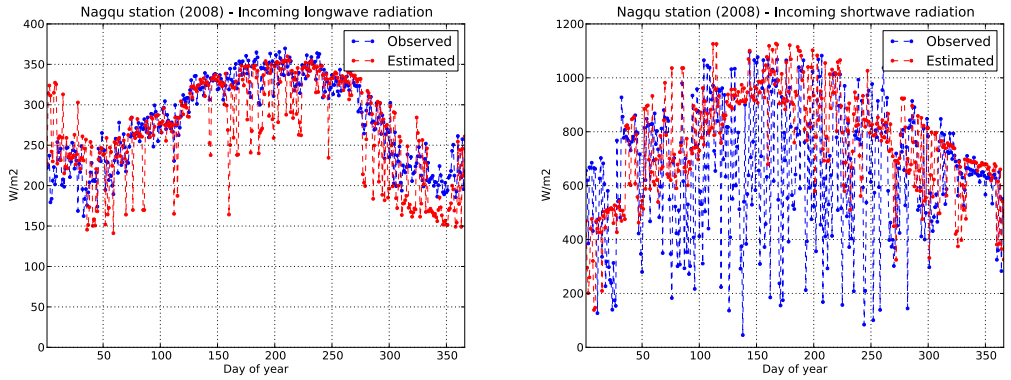

(a) Downward longwave radiation

(b) Downward shortwave radiation

Figure 7.3: Time-serie of downward longwave and shortwave radiation for the Nagqu station during the year 2008.

resentative of the atmosphere state in the line of sight between the sensor and land surface at the moment of the calculation timestamp (2 pm Beijing Time), and thus correspond to the presence or absence (but gap-filled) of temperature data in the corresponding FY-2 acquisition.

Theoretically, during cloudy (partly or fully) days, the solution of the surface radiative balance is more complicated when using NWPM outputs. Up to 257 W/m^2 of RMSE between measured and estimated net radiation for the year 2010 at the Nagqu station is observed for cloudy conditions, when the error reaches 135 W/m^2 for clear sky (Tables 7.2b and 7.2c). This difference can be explained by the fact that for cloudy days, the GRAPES model may not well estimate shortwave and longwave incoming radiation, since it is difficult to reproduce the exact behavior of small-scale cloud structures. However, in Table 7.2, at the Linzhi station the RMSE in Rn estimation reaches 369 W/m^2 for clear sky conditions, and 314 W/m^2 for cloudy sky. The fact is that sometimes, contrary to the previous situation, as the GRAPES grids are representative of large areas it leads to a higher cloud fraction simulated over the station.

A comparison between the simulated and measured incoming radiation shows that the majority of errors is explained by the shortwave term. Figure 7.3 reveals that the GRAPES model has difficulties to catch the variations of downward shortwave radiation. Therefore, here these variations are explained by cloudy sky conditions (Table 7.2c), while at the Linzhi station they occur during potential clear sky conditions. An other explanation can be found in the fact that the Linzhi station is located in a mountainous area where local convective events are important, mainly during the monsoon season. Meanwhile, this problem is not observed

for the Qomolangma station which is located in a similar geographical context.

This issue leads to a global overestimation of Rn at the four stations, especially during the monsoon season. The excess of available energy is for instance mainly transferred to the ground heat flux (for Nagqu and Linzhi) and sensible heat flux in 2008, except at Namco. In 2009, excess of available energy is transferred to latent heat flux, except at Qomolangma station. And in 2010, this energy excess is attributed to sensible heat flux. Only the Namco station seems to achieve an acceptable accuracy on ground heat flux (RMSE < 61 W/m^2). All the other stations gave RMSE on G_0 < 100 W/m^2 except at Nagqu, and also at Linzhi in 2008 but errors are then considerably reduced in 2009-2010 (Table 7.2a).

The overestimation of the instantaneous λE leads automatically to an increase of the daily scaled values. Following the method of the constant ratio, the scale factor is mainly provided by the magnitude of the evaporative fraction, which increases with λE overestimates. The method based on a sine function is also sensitive to the provided value of λE since it determines the amplitude of the sinusoidal shape. The error analysis demonstrates clearly that for all skies conditions, the sine method for daily scaling of ET always provide better results, even at Qomolangma station. The improvement in ET_d estimation is illustrated by Figure 7.4 at the Linzhi station (RMSE always inferior to 1 mm/day).

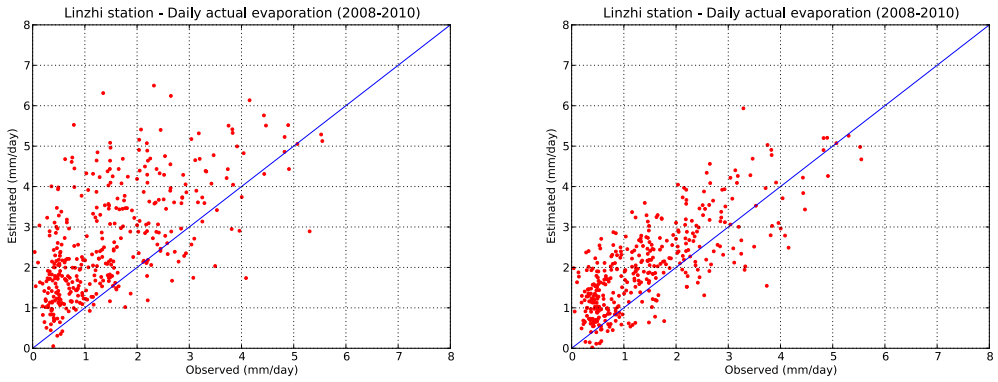

(a) ET_d based on a constant ratio

(b) ET_d based on a sine function

Figure 7.4: Comparison between measured and estimated daily actual evapotranspiration at the Linzhi station scaled by a constant ratio (a) and a sine function (b) over the period (2008-2010).

Figure 7.5 is an example of daily integrated evapotranspiration (ET_d) for the 14^{th} October 2008 over the whole Tibetan Plateau. The black frame of images represents the study area defined by the CEOP-AEGIS project (Zheng et al., 2011). However, results present this systematic gap on the west part of the Tibetan

Plateau, since the targeted domain of GRAPES data was unfortunately reduced.

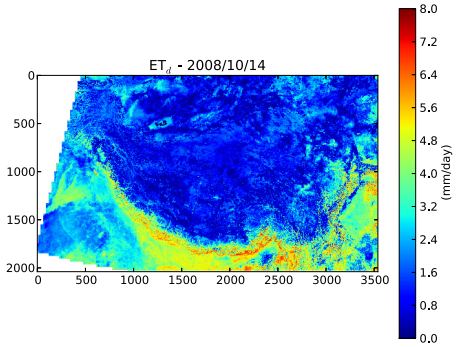

(a) ET_d based on a constant ratio

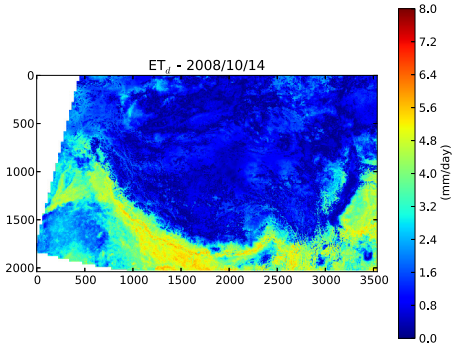

(b) ET_d based on a sine function

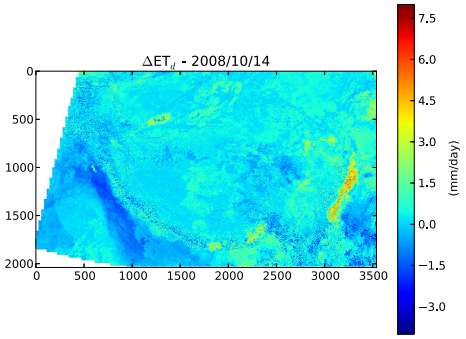

(c) Difference between the two scaling methods

Figure 7.5: Example of ET_d over the Tibetan Plateau for the 14^{th} October 2008, and difference between the two scaling methods.

ET_d can be obtained by the use of daily mean net radiation weighted by the ratio G_0/Rn and partitioned by the evaporative fraction (Figure 7.5a), as described in Section 7.3. This method assumed that the two latter terms are constant during the diurnal period. Figure 7.5b also shows an ET_d map over the Tibetan Plateau at the same date, but obtained using the sine function. Figure 7.5c highlights the differences between the two methods. It appears clearly that the use of the sine function for the scaling of ET_d reduces the daily values, not only at the four validation sites, but also at the scale of the Tibetan Plateau. The daily rates of evapotranspiration seem more homogeneous and consistent for high-elevation land surfaces.

Table 7.2: RMSE in the estimation of instantaneous net radiation (Rn), ground heat flux (G_0), latent heat flux (λE), sensible heat flux (H), hourly (ET_h) and daily (ET_d) actual evapotranspiration for the 2008-2010 period, and corresponding to all skies (7.2a), clear sky (7.2b) and cloudy sky (7.2c) conditions.

(a)

	2008 - All skies				2009 - All skies				2010 - All skies			
Variables	Nagqu	Namco	Linzhi	Qomo	Nagqu	Namco	Linzhi	Qomo	Nagqu	Namco	Linzhi	Qomo
Rn (W/m^2)	208.45	165.75	340.17	134.09	-	206.43	200.92	105.67	207.08	133.26	180.07	126.15
G_0 (W/m^2)	125.51	59.70	131.55	72.27	-	60.99	85.44	81.56	103.75	48.22	90.51	96.95
λE (W/m^2)	113.02	128.51	104.94	106.77	-	139.82	121.20	119.22	114.18	74.37	73.48	140.66
H (W/m^2)	114.58	92.85	223.50	123.24	-	99.89	98.62	157.19	142.23	116.89	132.21	189.68
ET_h (mm/hour)	0.17	0.19	0.15	0.17	-	0.20	0.18	0.18	0.17	0.11	0.11	0.22
ET_d $ratio$ (mm/day)	1.96	1.98	1.61	1.62	-	2.07	1.81	2.08	1.48	1.53	1.38	2.73
ET_d $sine$ (mm/day)	1.71	1.26	0.95	1.42	-	1.39	0.96	1.62	1.25	0.82	0.78	2.00
Nb. of obs.	126	131	145	233	1	230	109	240	106	85	84	55

(b)

	2008 - Clear sky				2009 - Clear sky				2010 - Clear sky			
Variables	Nagqu	Namco	Linzhi	Qomo	Nagqu	Namco	Linzhi	Qomo	Nagqu	Namco	Linzhi	Qomo
Rn (W/m^2)	143.04	145.63	369.97	105.18	-	156.42	185.14	79.50	135.46	114.29	151.98	95.17
G_0 (W/m^2)	128.53	63.91	149.26	66.21	-	48.02	69.08	78.71	92.74	55.19	66.05	94.56
λE (W/m^2)	104.88	131.29	113.03	97.98	-	119.77	129.59	104.01	80.13	60.30	74.97	120.52
H (W/m^2)	101.02	98.45	246.57	121.19	-	83.74	95.76	151.80	114.27	98.50	139.04	175.08
ET_h (mm/hour)	0.15	0.19	0.16	0.14	-	0.18	0.19	0.15	0.12	0.09	0.11	0.18
ET_d $ratio$ (mm/day)	2.12	2.08	1.35	1.55	-	2.03	1.67	1.96	1.15	1.34	1.51	2.33
ET_d $sine$ (mm/day)	1.53	1.31	0.91	1.36	-	1.31	0.96	1.48	0.97	0.73	0.82	1.70
Nb. of obs.	42	28	64	164	0	86	49	180	52	36	45	41

(c)

	2008 - Cloudy sky				2009 - Cloudy sky				2010 - Cloudy sky			
Variables	Nagqu	Namco	Linzhi	Qomo	Nagqu	Namco	Linzhi	Qomo	Nagqu	Namco	Linzhi	Qomo
Rn (W/m^2)	234.41	170.81	314.64	184.17	-	231.20	212.94	160.33	257.89	145.64	207.81	189.71
G_0 (W/m^2)	123.97	58.52	115.65	84.95	-	67.56	96.76	89.84	113.34	62.96	112.28	103.64
λE (W/m^2)	116.87	127.74	98.07	125.21	-	150.53	108.28	152.35	139.32	83.21	71.72	184.05
H (W/m^2)	120.79	91.27	200.60	127.99	-	108.39	100.89	166.16	164.74	128.74	123.86	224.64
ET_h (mm/hour)	0.17	0.19	0.14	0.18	-	0.22	0.16	0.22	0.20	0.12	0.11	0.27
ET_d $ratio$ (mm/day)	1.87	1.96	1.79	1.78	-	2.10	1.91	2.39	1.74	1.65	1.20	3.67
ET_d $sine$ (mm/day)	1.80	1.25	0.98	1.49	-	1.44	0.97	1.91	1.48	0.88	0.74	2.65
Nb. of obs.	84	103	81	69	1	144	60	60	54	49	39	14

7.5 Towards hourly monitoring of surface heat fluxes

From the observations made by Faivre et al. (2012) on the use of the hourly time step (FY-2 data) for few sunny and partly cloudy days, it appeared that the assumption about the constancy of G_0/Rn ratio and evaporative fraction is not verified by ground measurements. During the diurnal cycle, the evaporative fraction presents a sinusoidal shape, such as the behavior of net radiation. Also, the ratio G_0/Rn is never constant since the onset of the sinusoidal evolution of ground heat flux during daytime is shifted, such as the land surface temperature. These conclusions led to evaluate the potential of an other daily evapotranspiration scaling method (Equation 7.1), which proved its efficiency in Section 7.4.

However, calculations of the surface energy balance on a hourly basis can still significantly improve the quality of the time-series of daily evapotranspiration, especially considering the high occurrence of gaps due to clouds during the monsoon season. The Feng-Yun series of geostationary satellites provides hourly acquisitions. This gain is obtained with a loss of spatial information (5 km x 5 km), but it allows to perform LST gap-filling and estimation of actual evapotranspiration every hour, even under cloudy sky conditions.

Following the study by Faivre et al. (2012), MSSEBS is applied using hourly LST from gap-filled FY-2 data for an investigation conducted over the whole month of June 2008 (720 hourly calculations), specifically chosen for the intensity of the monsoon season. The resolution of atmospheric stability parameters is dynamically adjusted as a function of the mean PBL height. The calculation grid size is ranging from 5 km during nighttime to sometimes 30 km during the afternoon. The observed diurnal mean PBL height is usually 2 km. Table 7.3 presents the calculation scales chosen following the mean PBL height estimated over the Tibetan Plateau from GRAPES data. The mean height classification is defined in order to always retrieve integer numbers by dividing up the initial area of interest (3540 by 2040 pixels for VNIR based data).

Table 7.3: Definition of the cell size for stability parameters calculation in function of the Planetary Boundary Layer height (PBL_h).

Mean PBL_h	Limits	Cell size	Grid dimension
500 m	PBL_h < 750 m	5 km	708 $\times$ 408
1000 m	750 m < PBL_h < 1250 m	10 km	354 $\times$ 204
1500 m	1250 m < PBL_h < 1750 m	15 km	236 $\times$ 136
2000 m	1750 < PBL_h < 2500 m	20 km	177 $\times$ 102
3000 m	2500 m < PBL_h	30 km	118 $\times$ 68

Figure 7.6 shows that diurnal variations of net radiation at the Namco station are not well reproduced and the resolved SRB does not reflect the observed fluctuations of available energy for cloudy sky conditions. Only few days during the month of June are completely clear. The overall tendency at the four stations is still to the overestimation of Rn values. This overestimation appears in the calculations of hourly evapotranspiration, as demonstrated at the Qomolangma station in Figure 7.7a, but the tendency is inverted during the middle of the month. This inversion is partly explained by the large relative error (> 30%) introduced after the energy balance closure based on Bowen ratio, and also by the remaining problem of cloud simulation by GRAPES.

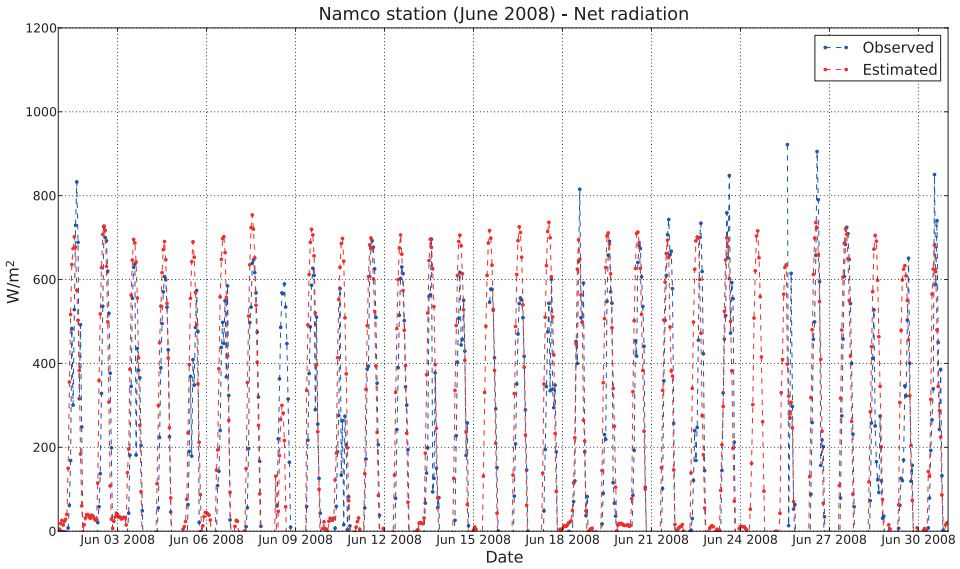

Figure 7.6: Time-serie of measured and estimated net radiation at the Namco station (June 2008).

Figure 7.7b illustrates the gain obtained during the month of June 2008 by integrating the estimations of hourly evapotranspiration at the Qomolangma station, regarding the two others ET_d scaling methods presented in Sections 7.3 and 7.4. Figures 7.8a and 7.8b document this improvement by comparing $ET_d\ sine$ and $ET_d\ hourly$ validation for all stations. Table 7.4 reveals that the most important gain is achieved at the Namco station, with a final RMSE reduced to 0.98 mm/day, which is 3.3 times less than the initial estimation based on the constant ratio method. However, it is important to notice that here the error is calculated only for 17 available ET_d values due to gaps in ground measurements. Also, the hourly integration is more accurate for retrieving ET_d because it only takes into account the hourly timestamps which are present in ground measurements. The

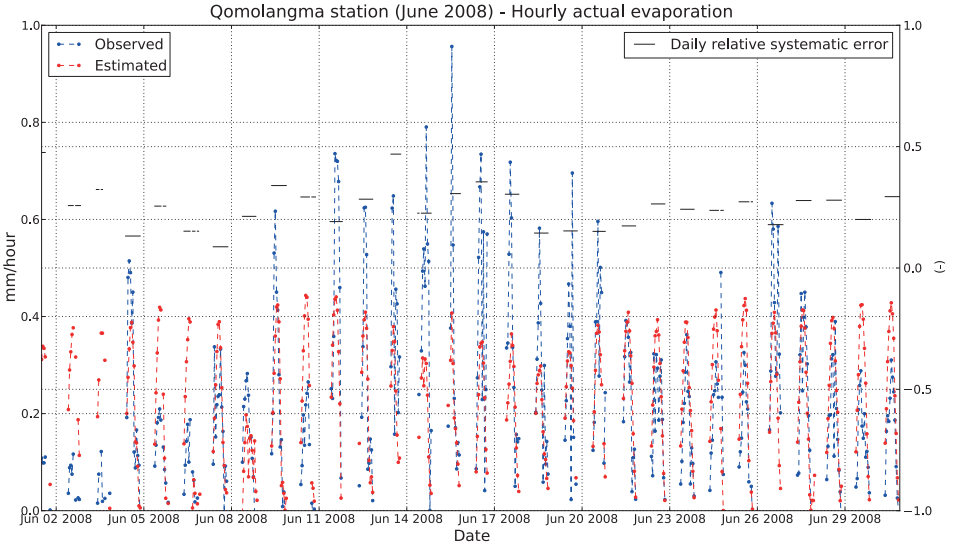

(a) 1-month time-serie of ET_h

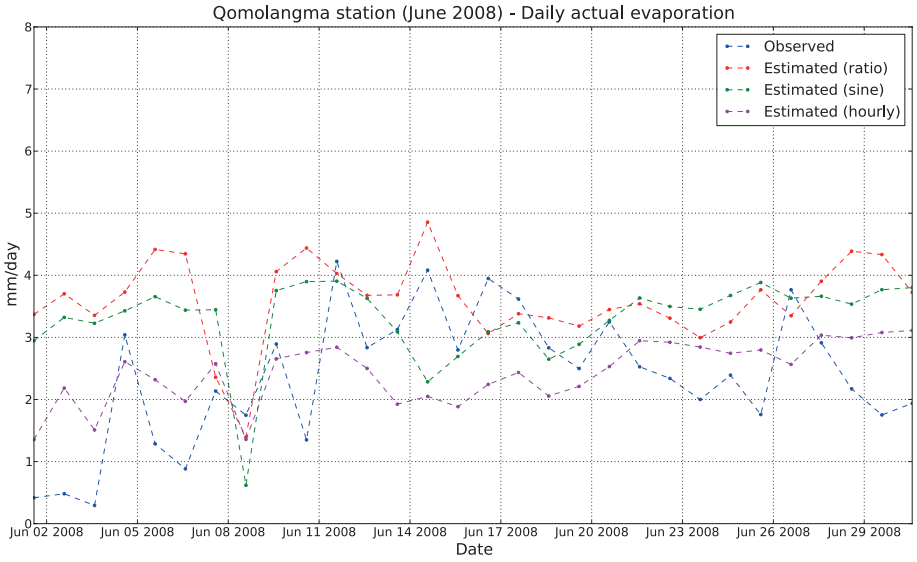

(b) 1-month time-serie of ET_d

Figure 7.7: Time-serie of measured and estimated (a) hourly and (b) daily actual evapotranspiration at the Qomolangma station (June 2008).

ET_d *ratio* and ET_d *sine* methods automatically provide higher daily rates (Figure 7.7b) since they consider the whole diurnal period. As depicted in Figure 7.7a, some turbulent flux measurements are skipped due to the Bowen ratio correction (threshold values in flux densities), mainly around the sunrise and sunset period but sometimes also during the day. Unfortunately this implies some bias in the

evaluation that cannot be removed.

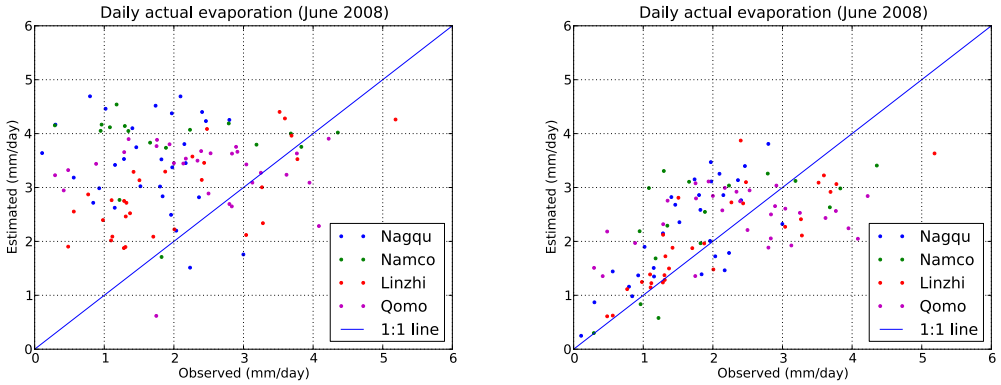

(a) ET_d based on a sine function

(b) ET_d based on an hourly integration

Figure 7.8: Comparison between the results of the (a) sine function and (b) hourly integration for all stations during the month of June 2008.

Table 7.4: RMSE in the estimation of daily actual evapotranspiration for the month of June 2008.

	June 2008			
Variables	Nagqu	Namco	Linzhi	Qomo
ET_d *ratio* (mm/day)	2.28	3.16	2.23	1.73
ET_d *sine* (mm/day)	2.16	2.26	1.19	1.54
ET_d *hourly* (mm/day)	0.83	0.98	0.65	1.03
Nb. of obs.	30	17	30	30

In definitive, this study still suffers from some limitations. i) The measurements performed at Namco station are certainly affected by the proximity of the lake (advection) and must therefore be used carefully to compare with 1km grid fluxes. ii) Qomolangma and Linzhi stations are located in mountainous areas and measurements have to be also carefully compared with MSSEBS outputs. The inconsistency between scales may play an important role in the comparison. iii) Although the ET_h approach tends to give better results, a detailed analysis of results shows that the algorithm used to derive the soil heat flux is not appropriate, at least in some context. Moreover, at the diurnal scale the estimated ground heat flux follows the diurnal pattern of the net radiation, while it is more linked to the

daily pattern of the land surface temperature. Also, some G_0 measurements are suspected to be unreliable due to some erratic daily behaviors.

7.6 Additional investigations

It is obviously difficult to investigate precisely the paramaterization of heat transfer at large scales. The ability of MSSEBS to provide reliable results over the Tibetan Plateau is essentially due to the quality of input data describing land surface parameters and atmospheric state. In the frame of the CEOP-AEGIS project, a set of enhanced land surface data products were available for this study (see Sections 3.3 and 3.4), which was an unique opportunity. The complete 3D (and so the at-surface and at-PBL) atmospheric behavior, over a such area and during a such continuous period, represents a huge contribution for producing a 3-years time-serie.

However, improvements can be made in term of description of the terrain roughness as seen in Chapters 5 and 6, which is by default still described by vegetation (Moran, 1990). Considering the presence of high elevated areas, Himalayan mountains may play a role in aerodynamic roughness length for momentum transfer. A comparative study can be performed over the 3-years period for determining the importance of taking into account the relief in z_{0m} retrieval.

Moreover, the estimation of turbulent heat fluxes with SEBS or MSSEBS is highly dependent on the atmospheric state at the reference level, which corresponds at this scale to the Planetary Boundary Layer. The capacity of a NWPM to accurately describe the atmospheric behavior through the integration process between heterogenous land surface and the top of PBL is a key issue. This aspect is mainly dependent to the choice of land surface and PBL schemes, but also to the input re-analysis.

7.6.1 Roughness at the Tibetan Plateau scale

Taking benefits from the investigations made in Chapters 5 and 6 related to the roughness length retrieval, the adapted z_{0m} formulation from Menenti and Ritchie (1994) is applied here to the 3-years estimation of turbulent heat fluxes over the Tibetan Plateau. It is a good way for evaluating its reliability in an operational context. Figure 7.9 shows an example of the spatial distribution of roughness length z_{0m} for the 1^{st} August 2008. In Figure 7.9a roughness is only driven by the presence of green vegetation, while in Figure 7.9b the Himalayan belt is clearly highlighted.

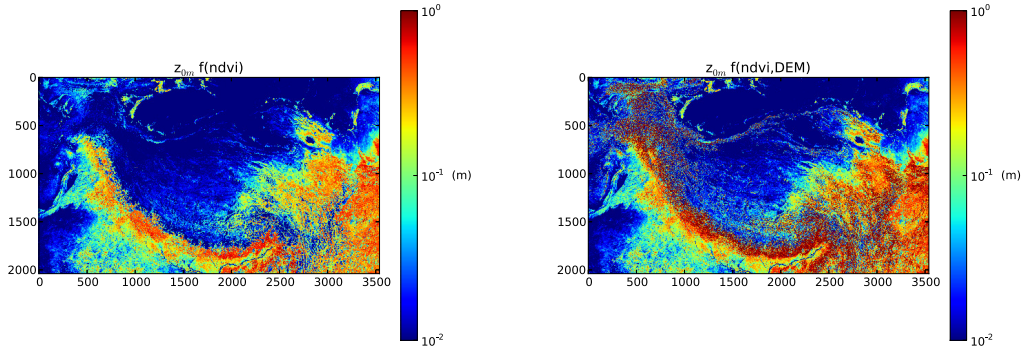

(a) z_{0m} following Moran (1990)

(b) z_{0m} from Menenti and Ritchie (1994)

Figure 7.9: Comparison between the two roughness length formulations at the scale of the Tibetan Plateau for the 1^{st} August 2008.

7.6.2 Alternative atmospheric variables

Ueno et al. (2011) have used the Weather Research and Forecast model (Skamarock et al., 2008) to simulate the meso-scale convective systems genesis that occurred in 2008 over the Sichuan Basin in China. The authors have kindly provided their WRF simulations since these latter were covering an important part of Asia, and so the Tibetan Plateau. In this study three nested domains were defined : 10-50°N, 60-130°E; 14-47°N, 65-123°E; and 25- 40°N, 98-110°E with horizontal grid spacing of 60 km, 20 km and 4 km respectively. Calculations were conducted in two-way nesting between the domains. The extent and the spatial resolution of the second sector are adequate for providing atmospheric input data to MSSEBS.

Convective parameterization by the Kain-Fritsch scheme (Kain and Fritsch, 1990) and WSM6 cloud microphysics scheme (Hong and Lim, 2006) were used for the first and second sectors, and only the microphysics was applied in the third sector. The Mellor-Yamada-Janic scheme (Mellor and Yamada, 1982) was adopted for the calculation of the Plateau Boundary Layer. Land components were calculated by the Noah land surface scheme (Chen et al., 1996; Chen and Dudhia, 2001; Ek, 2003). The Rapid Radiative Transfer Model scheme for longwave radiation (Mlawer et al., 1997) and the Dudhia scheme for shortwave radiation (Dudhia, 1989) were applied. Japanese 25-year Re-Analysis (JRA-25) data (Onogi et al., 2007) were used to define the atmosphere boundary conditions with a time-step of 6 hours. The simulation period provided here is ranging from the 21^{st} to the 24^{th} June 2008 and the first 12 hours are for spin-up. Two entire days (22^{nd} and 23^{rd} June) are extracted from this dataset and allow to perform 48 hourly MSSEBS

calculations.

7.6.3 Preliminary results

On the role of elevation

The comparison of RMSE for estimated hourly and daily actual evapotranspiration over the period 2008-2010 (Table 7.5) with previous RMSE for all skies conditions (Table 7.2a) reveals that results are almost similar. The situation seems to be the same as what was observed for the Yingke station, in the Heihe river basin. The ground stations are located in open areas, which does not affect values of z_{0m}. Even the stations located in mountainous areas are not close enough to the surrounding relief for influencing the calculation of roughness inside the computing kernel. However, RMSE for the Linzhi and Qomolangma stations are slightly lower (-0.02 mm/day) when using this z_{0m} formulation. Errors in λE and H are also both systematically reduced (up to -3 W/m^2) compared to Table 7.2a, so it reveals a better partitioning. Figure 7.10 shows that z_{0m} values are a little bit higher over the three years at the Qomolangma station with a difference ranging from 0.002 m to 0.008 m.

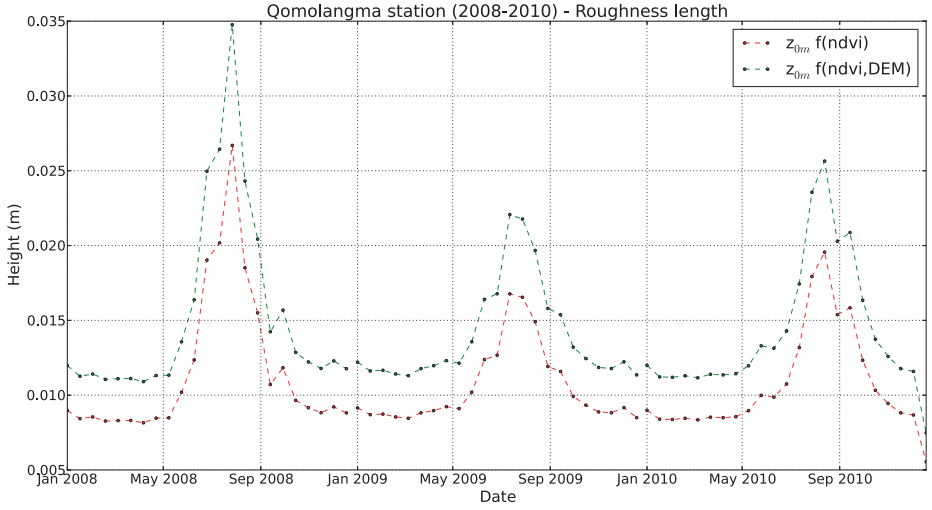

Figure 7.10: Time-serie of roughness length for momentum following Moran (1990) and Menenti and Ritchie (1994) at the Qomolangma station (2008-2010).

These results are preliminary and require further investigations through several observation stations located in mountainous areas with various land cover conditions, and a long-term evaluation. Also, it is obviously difficult to evaluate the radical change of roughness length values in the Himalayan belt (values close to 1 meter) since the set-up and maintenance of stations is quite difficult.

Table 7.5: RMSE in the estimation of turbulent heat fluxes, hourly and daily actual evapotranspiration by integrating the adapted formulation of z_{0m} for the 2008-2010 period.

Variables	Nagqu	Namco	Linzhi	Qomo
2008 - All skies				
λE (W/m^2)	113.02	128.51	102.94	105.69
H (W/m^2)	114.58	92.85	222.07	122.66
ET_h (mm/hour)	0.17	0.19	0.14	0.16
ET_d $sine$ (mm/day)	1.71	1.26	0.93	1.40
2009 - All skies				
λE (W/m^2)	-	139.82	118.34	117.97
H (W/m^2)	-	99.89	97.08	155.51
ET_h (mm/hour)	-	0.20	0.17	0.17
ET_d $sine$ (mm/day)	-	1.39	0.94	1.60
2010 - All skies				
λE (W/m^2)	114.18	74.37	71.74	139.46
H (W/m^2)	142.23	116.89	129.09	188.93
ET_h (mm/hour)	0.17	0.11	0.10	0.21
ET_d $sine$ (mm/day)	1.25	0.82	0.76	1.98

In these areas, the evapotranspiration rate is considered as really weak and is less considered in hydrological studies than snow and ice (glaciers) balance.

Sensitivity to atmospheric inputs

Table 7.6 presents RMSE between measured and estimated radiative components and surface heat fluxes for the $22^{nd}$and 23^{rd} June 2008. Only three stations are considered since at Namco data are missing during this period. It has been demonstrated previously that the most difficult radiative term to estimate is the incoming shortwave radiation, and it is still verified here with RMSE for longwave radiation always inferior to 50 W/m^2 for both models, but with lower errors for GRAPES. The comparison between the two days of simulation using both GRAPES and WRF models reveals that shortwave radiation is less well simulated by WRF at Nagqu and Linzhi stations with RMSE > 200 W/m^2 (while < 200 W/m^2 with GRAPES) except at the Qomolangma station where the situation is inverted (307 W/m^2 for GRAPES and 208 W/m^2 for WRF). Errors in net radiation retrieval follow the same repartition.

The estimation of ground heat flux is still hazardous and the variation of RMSE between the use of the two NWPM is explained by the difference of radiative budget. Errors in λE retrieval are always < 100 W/m^2 with GRAPES. RMSE on H is larger but partitioning of Rn is better. While with WRF inputs, RMSE is reduced for H at Nagqu and Qomolangma stations, but errors are systematically transferred to the other term which reveals a wrong net radiation partitioning. Considering the hourly evapotranspiration rate, RMSE are lower when using GRAPES input data (maximum of 0.13 mm/hour at Nagqu) and are for instance two times larger at Qomolangma station when using WRF dataset (0.18 mm/hour).

Figure 7.11 illustrates the differences of PBL development between GRAPES and WRF models. The phases are identical, while the amplitude (up to 800 m higher for WRF) and the decreasing speed (still larger for WRF) differ. These differences obviously lead to variations in terms of temperature and humidity at the PBL level, which partly explain the differences between estimated heat fluxes. Even though the grid sizes are different, this figure and RMSE of radiative components show clearly how atmospherical variables can differ following the model chosen, the choice of physics schemes and re-analysis input data. These differences have a considerable impact on the estimation of turbulent heat fluxes.

The aim of this short investigation is not to incite users to prefer GRAPES instead of WRF, but to demonstrate how MSSEBS (and so SEBS) is sensitive to various parameters, even to atmospheric inputs. Also, considering the small time scale, these results are only representative of this period and of the three stations considered and cannot lead to criticize the accuracy and the choice of

Table 7.6: RMSE in the estimation of instantaneous longwave incoming radiation ($L_w \downarrow$), shortwave incoming radiation ($S_w \downarrow$), net radiation (Rn), ground heat flux (G_0), latent heat flux (λE), sensible heat flux (H) and hourly actual evapotranspiration (ET_h) for the 22^{nd}-23^{rd} June 2008 period, respectively using GRAPES and WRF atmospheric input data.

Variables	Nagqu	Namco	Linzhi	Qomo
22^{nd} & 23^{rd} June 2008 - GRAPES				
$L_w \downarrow$ (W/m^2)	21.75	-	25.08	44.81
$S_w \downarrow$ (W/m^2)	154.81	-	191.33	307.87
Rn (W/m^2)	102.17	-	192.56	206.45
G_0 (W/m^2)	122.42	-	54.55	83.65
λE (W/m^2)	86.74	-	67.97	62.89
H (W/m^2)	92.38	-	101.47	101.48
ET_h (mm/hour)	0.13	-	0.10	0.09
22^{nd} & 23^{rd} June 2008 - WRF				
$L_w \downarrow$ (W/m^2)	48.30	-	40.34	48.71
$S_w \downarrow$ (W/m^2)	229.61	-	277.33	208.31
Rn (W/m^2)	145.14	-	256.38	191.70
G_0 (W/m^2)	125.13	-	73.30	87.75
λE (W/m^2)	122.38	-	80.33	123.51
H (W/m^2)	50.92	-	118.20	74.65
ET_h (mm/hour)	0.18	-	0.12	0.18
Nb. of obs.	12	0	12	24

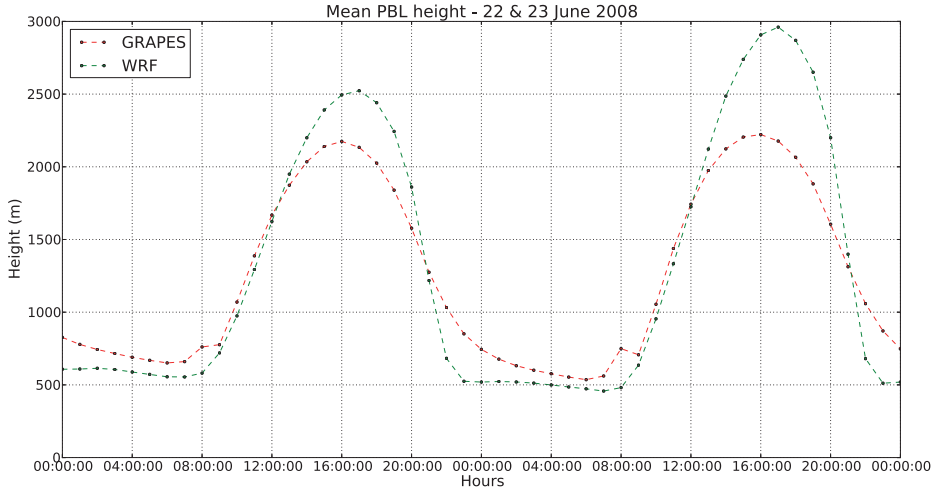

Figure 7.11: Mean Planetary Boundary Layer height over the Tibetan Plateau simulated by GRAPES and WRF models for the 22^{nd} and 23^{rd} June 2008.

WRF configuration made by Ueno et al. (2011), which are mainly dependent of the targeted applications. Moreover, whatever the NWPM chosen, the problem of scales and of local effects raised in the validation cannot be avoided.

Recently, Lohou and Patton (2014) reproduced the effect of shallow cumulus shading on the energy balance, which has significant local impacts and particularly on turbulent heat fluxes. These clouds are rather small with more or less a size of one kilometer, and may represent a huge part of the cloud fraction at the scale of the Tibetan Plateau. The authors demonstrated that the cloud shading leads to an increase of the evaporative fraction up to 20-30% locally and about 2-3% regionally. Typically, these small cloud structures cannot be represented by large scale NWPM with grid size of few tens kilometers, and will always be a source of deviation between observations and estimates of energy balance.

7.7 An overview of final ET products

7.7.1 At the station scale

Figure 7.12a illustrates the complete 3-years time-series (2008-2010) of daily actual evapotranspiration at the Nagqu, Namco, Linzhi and Qomolangma stations. The final product presented here was obtained following the promising conclusions made in the previous sections : a daily scaling based on Equation 7.1 and a z_{0m} parameterization adapted from Menenti and Ritchie (1994). The four stations present obviously all a similar seasonal trend, since they are close enough and all

located on the Plateau, with a peak centered on July in the range 4-5 mm/day (up to 6 mm/day at Linzhi). However, ET estimates at the Linzhi station are rather high during the winter. All the stations present ET_d fluctuations during the annual cycle, which are larger during the monsoon season. This is explained by the occurrence of convective events which provoke large amplitudes in daily ET rates.

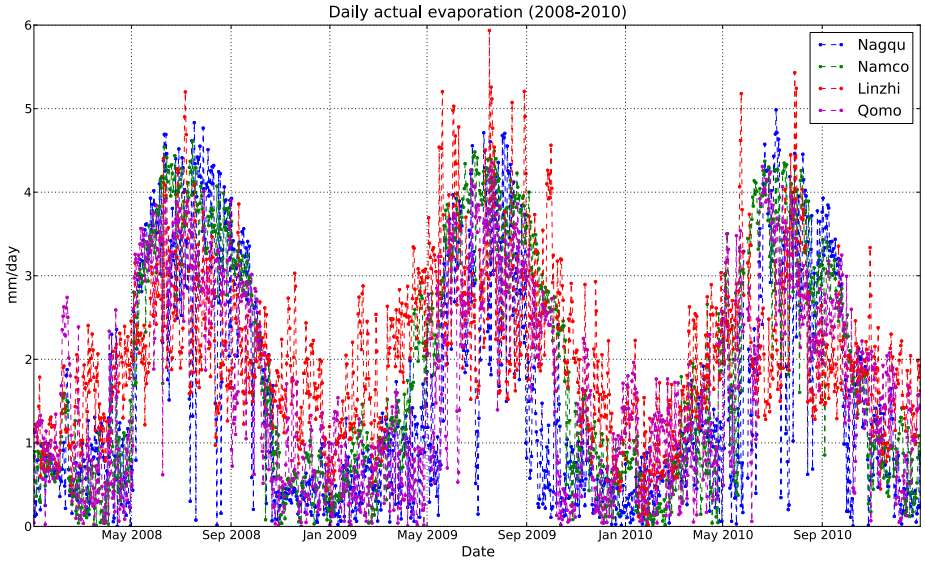

(a) Daily ET

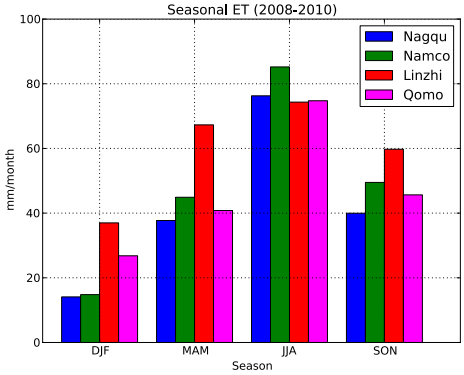

(b) Seasonal ET

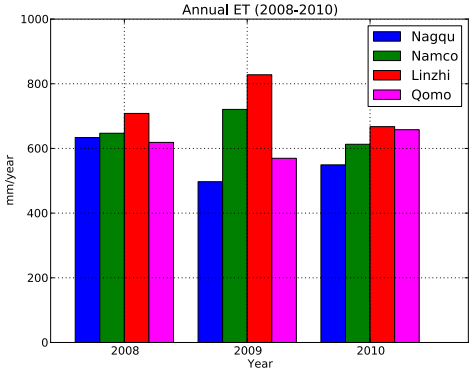

(c) Annual ET

Figure 7.12: (a) Daily, (b) seasonal and (c) annual evapotranspiration rate at the Nagqu, Namco, Linzhi and Qomolangma stations for the period 2008-2010.

Figure 7.12b summarizes the seasonal trend for each station over the complete period 2008-2010. The difference of monthly means for seasonal ET is large for

Nagaqu and Namco stations between winter (< 20 mm/month) and summer ($\pm$ 80 mm/month). This difference is lower for Qomolangma station : from about 30 mm/month to $\pm$ 75 mm/month. The seasonal mean is always higher at Linzhi station, except during summer (< 80 mm/month, which is similar to Qomolangma), and its annual evolution is smoother with only a difference of $\pm$ 40 mm/month between winter and summer.

Figure 7.12c presents the annual sum of ET_d for each year of the period 2008-2010 at the four reference stations. The highest annual ET is obviously observed at Linzhi with values in the range 600-700 mm/year in 2008 and 2010, and a peak for 2009 (> 800 mm/year). The Namco station presents the same dynamic with $\pm$ 600 mm/year in 2008 and 2010, and > 800 mm/year in 2009. At the Qomolangma station, the annual ET rate is almost constant : $\pm$ 600 mm/year with a slight decrease in 2009 and an increase in 2010. The Nagqu station presents a similar trend in the range 500-600 mm/year. Globally, annual ET rates are quite similar and homogeneous in 2008 and 2010 between the four stations (differences < 100 mm/year, with the Linzhi station as leading), but have large differences in 2009 (nearly 200 mm/year).

It is interesting to see that each station has its own seasonal and inter-annual variation, even when they are located in similar areas, such as Nagqu and Namco (plateau), or Linzhi and Qomolangma (valley). The Namco area is maybe influenced by the immediate vicinity of the lake, which can contribute to raise ET estimates. The latitude, elevation, slope and orientation of the valleys can also have a large impact on evapotranspiration rates. These areas are also strongly subject to local effects.

7.7.2 At the Tibetan Plateau scale

Figure 7.13 gives an overview of the monthly ET rates averaged by season over the Tibetan Plateau for the period 2008-2010. The lower ET rates are always observed for the high-elevated areas such as the Himalayan belt and the plateau, and also for the northern desertic regions : Gobi and Taklamakan deserts with ET < 40 mm/month in winter and ET < 120 mm/month in summer. However, during spring and summer a contrast appears with the development of the highest values (from 80 to 120 mm/month) in the south-east part of the Plateau and in Taklamakan desert. This difference is explained by a more important vegetation density in these areas, than over the rest of TP.

The plains located from south-west to south-east of the Tibetan Plateau present higher ET values. These areas correspond to the headwaters of Indus, Ganga, Brahmaputra and Yangtze basins. The plains of Pakistan and India have a minimal ET rate of $\pm$ 100 mm/month in winter, and a maximal of $\pm$ 180 mm/month in summer. The Yangtze headwater has a similar seasonal amplitude but with lower

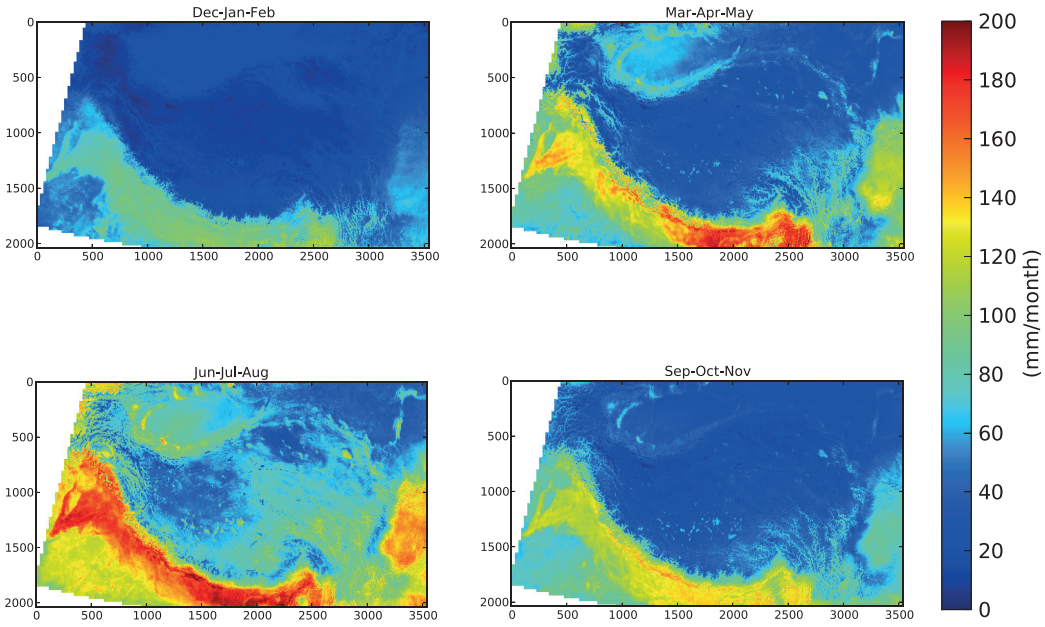

Figure 7.13: Seasonal evapotranspiration rate (mm/month) over the Tibetan Plateau for the period 2008-2010.

ET rates (from 60 mm/month to 140 mm/month).

Figure 7.14 presents the annual ET rates over the Tibetan Plateau for each year, and for the overall period 2008-2010. The spatial repartition between low and high values is obviously similar to Figure 7.13. The annual mean for the plateau is nearly 600 mm/year, with highest values in the south-east part due to the seasonal vegetation growth (up to $\pm$ 800 mm/month). Gobi desert has an ET annual mean around 400 mm/year, while Taklamakan desert is almost around 700 mm/year due to the vegetation. The Yangtze headwater annual mean corresponds to the range 1200-1400 MM/year. The drained plains of Pakistan and India (Indus and Ganga headwaters) have an annual mean ET of about 1500 mm/year, and higher in eastern India (Brahmaputra headwater) with $\pm$ 1800 mm/year. These areas have clearly a higher annual ET rate during 2008 with a total ranging from 1600 mm/year to 2000 mm/year.

The advantage with such ET products, compared to NWPM outputs for instance, is clearly that the spatial resolution is rather high when the temporal resolution is very convenient. This type of time-serie is relevant for detailed hydrological studies over large areas. Also, as mentioned earlier, the parameterization of surface roughness is more advanced, since models such as NWPM usually rely on look-up tables following the type of land-cover (and a theoretical seasonality when vegetation is considered).

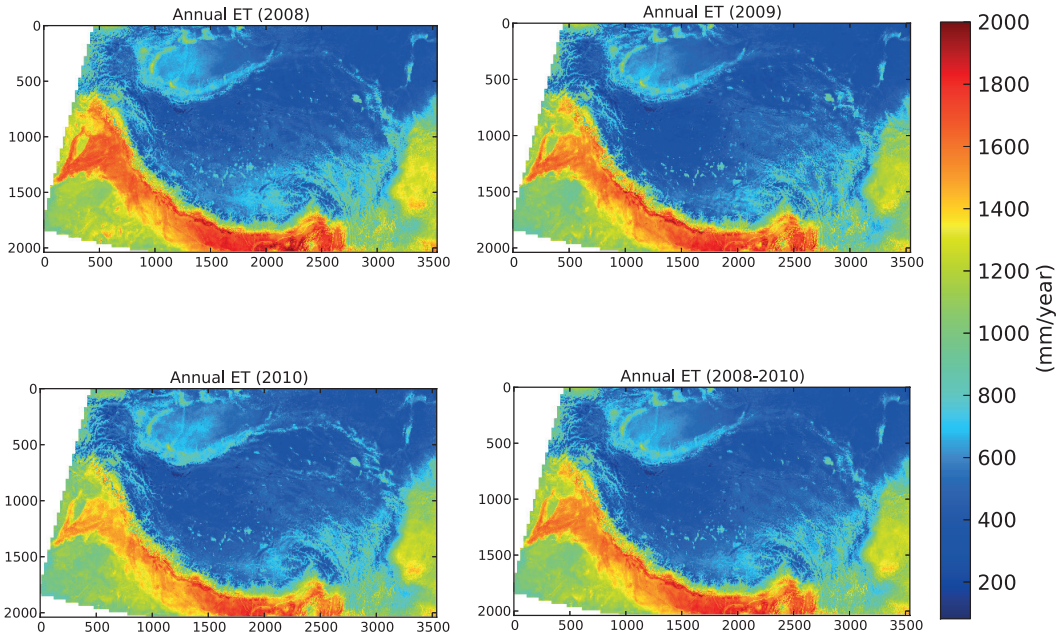

Figure 7.14: Annual evapotranspiration rate (mm/year) over the Tibetan Plateau for the period 2008-2010.

7.8 Conclusion

The production of an evapotranspiration time-serie over a such extent at this location and during such a time period is something new in the hydrological community. Some studies already led to long-term monitoring of land surface evapotranspiration in China but mainly over rather limited areas (Jia et al., 2009, 2012b). The MODIS global evapotranspiration product MOD16 (Mu et al., 2013) is systematically produced at a spatial resolution of 1 km^2, but it only provides 8-day, monthly and annual rates and the Tibetan Plateau area is not covered. In this sense, this study is filling a gap.

The implementation of the combined SEBS and MSSEBS approaches proposed by Su (2002) and Colin (2006) for surface energy balance calculation, and the processing chain developed to compute daily surface energy balance allow to produce consistent time series of heat fluxes on a daily basis over the entire Tibetan plateau (annual RMSE inferior to 2 mm/day). The complete dataset of daily evapotranspiration (2008-2010) has been used in the frame of the CEOP-AEGIS project as an input for the distributed water balance model (Faivre et al., 2013; Liu et al., 2013).

The evaluation of MSSEBS calculations demonstrates that the accuracy of the

SEB estimates can vary following a seasonal trend. During the monsoon season, convective events occur frequently and affect the surface radiative balance. The differentiation between the calculations performed using filled and non-filled LST data over the validation sites, proved that errors in the estimation of instantaneous heat fluxes are generally less important for clear sky conditions. Meanwhile, ground measurements are extremely gappy and finally, very few occurrences are available for validation.

Also, the comparison of the ET_d scaling strategies reveals that the method based on the extrapolation by the mean of a sine function gives always better agreements for any sky conditions 7.2. The focus study on the month of June 2008, corresponding to 720 continuous hourly calculations, demonstrated that the better scaling strategy during cloudy sky conditions (e.g. during the monsoon season) is the integration of ET_h estimations 7.4. Results are significantly improved, but partly due to the consideration of some hourly gaps. Moreover, further refinements have to be made to better estimate the soil heat flux, which will improve the estimation of the net available energy for turbulent heat fluxes.

Additional investigations showed that the consideration of elevation for roughness length retrieval may slightly improve the estimation of turbulent heat fluxes. This aspect still require further validations. Moreover, MSSEBS results are highly dependent of the input data quality. Estimations of surface radiative balance and partitioning between turbulent heat fluxes can considerably vary following the choice of NWPM outputs.

Nevertheless, it is important to be conscious about the caution that requires this kind of validation since the difference between the scales considered for estimations (i.e. GRAPES grid is about 30 by 30 km and LST FY-2 about 5 by 5km) and observations (i.e. EC system footprint) is huge. In this way, the use of Large Aperture Scintillometer measurements for validation once again would be more appropriate. However, the roughness of this area and the lack of human and material supply increase the difficulty to ensure any precise, reliable and continuous ground measurements. Moreover, it would have been interesting to perform validation studies also over downstream flat and vegetated areas such as in India.

Chapter 8

General conclusion

8.1 Achievements

The parameterization of heat transfer by remote sensing, and based on SEBS scheme for turbulent heat fluxes retrieval, already proved to be very convenient for estimating evapotranspiration (ET) over homogeneous land surfaces. However, the use of such a method over heterogeneous landscapes (e.g. semi-arid regions or agricultural land) becomes more difficult, since the principle of similarity theory is compromised by the presence of different heat sources with various heights. This thesis aimed at first to propose and evaluate some models based on vegetation geometry for retrieving the surface roughness length for momentum transfer (z_{0m}), which is a key parameter in the characterization of heat transfer. But, such an investigation can only be led at a small scale with very-high resolution remote sensing data, for a precise description of the land surface. Therefore, the second aspect of this work was to determine how to address the roughness length retrieval for regional studies, and more generally, also if SEBS is suitable for estimating turbulent heat fluxes at larger spatial and temporal scales.

At the local scale (Chapter 4), the extraction of a digital surface model from a LIDAR points cloud associated with wind measurements in a CFD model, has provided 3D wind fields. Maps of roughness length for momentum transfer were generated by the inversion of wind profiles (Equation 4.1). This aerodynamic approach is very sensitive to the wind speed and direction given as an input to the CFD model, and accounts for the upstream airflow history (e.g. shelter effect due to windbreakers, flat land without obstacles). Also, two detailed geometrical approaches (Raupach, 1994; MacDonald et al., 1998) accounting for wind direction and surface elevation were implemented in a single computing tool. The roughness length values obtained are rather similar for both geometrical models and do not really vary with the orientation of wind flow in the context of the Yingke area.

Then, the evaluation of the roughness length retrieval methods in Chapter 5 has been performed at the scale of measured heat fluxes footprint. Three other (semi) empirical models for z_{0m} retrieval were added in this assessment (Moran, 1990; Brutsaert, 1982; Menenti and Ritchie, 1994). Land surface evapotranspiration was calculated by the combination of airborne VNIR & TIR acquisitions, with ground meteorological observations and the different roughness length data. CFD-based roughness length parameterization gave a better estimation of sensible heat flux at the meteorological station scale, but the formulation proposed by Brutsaert (1982) allows for a slightly better partitioning of net radiation. Moreover, this latter formulation was elaborated for relatively homogeneous land cover such as the Yingke station surroundings.

Since the spatial validation based on heat flux footprint has been possible for only one occurrence, two time-series of 14 days including flux measurements and SEBS calculations were compared at the scale of the meteorological station. The temporal evaluation has confirmed the previous results, but also that the kB^{-1} model (Massman, 1999; Su et al., 2001), essential to determine roughness length to heat transfer (z_{0h}) from z_{0m}, is not suitable for complex geometric and aerodynamic configurations. Moreover, in order to really evaluate the potential of the CFD-based roughness length retrieval face to the simple relation proposed by Brutsaert (1982), the same study should be conducted over several study areas with various landscapes.

The additional evaluation performed in Chapter 6 is first focused on the use of the CFD-based and Brutsaert (1982) methods for roughness length retrieval, with the integration of a different kB^{-1} model (Jia, 2004). This latter on the thermal heterogeneity of land surface captured by the mean of bi-angular measurements (i.e. 0° and +53°) of surface temperature (LST) and fractional vegetation cover (f_c). Such devices were not set-up at the Yingke meteorological station, but observations of pure vegetation and soil components temperature has been performed. Following Norman et al. (1995) and Menenti et al. (2001), the angular behavior of LST and f_c can be synthetically retrieved from such ground measurements. Then, the temporal evaluation of estimated heat fluxes has confirmed the conclusions of Chapter 5 about the strengths of the CFD-based and Brutsaert (1982) models, even if RMSE are larger with the use of kB^{-1} model proposed by Jia (2004). Also, it revealed that this latter is suitable only for conditions where the land surface is thermally contrasted.

This evaluation was then transposed at the Heihe river basin scale, which is very convenient to assess both the characterization of z_{0m} over large areas, and the alternate kB^{-1} model with the use of bi-angular AATSR data. Two z_{0m} retrieval models were retained : the method of Moran (1990) based on NDVI, and the modified formulation proposed by Menenti and Ritchie (1994) which integrates NDVI and DEM. A cross analysis allowed to evaluate the two roughness and the

two kB^{-1} models together. From this experimental design, it appeared that :

- the model formulated by Jia (2004) provides larger kB^{-1} values over vegetated areas, and is less sensitive to variations in z_{0m} values.

- the adapted z_{0m} model from Menenti and Ritchie (1994) gives obviously higher roughness length estimates for mountainous areas while they remain stable for flat terrain.

- the original kB^{-1} model integrated in SEBS (Su, 2002) provides a slightly better heat flux partitioning over flat regions such as the Yingke area.

- the second kB^{-1} model (Jia, 2004), combined to the adapted z_{0m} formulation (Menenti and Ritchie, 1994), allows for a very accurate turbulent heat flux partitioning over mountainous areas.

It is obviously interesting to evaluate the reliability of each z_{0m} model over rough areas, but the representativeness of EC heat flux measurements to evaluate kilometric estimations seems weak due to the terrain complexity and its induced local effects.

Then, in the perspective of large scale and long-term studies for the monitoring of land surface evapotranspiration, SEBS algorithm was adapted in Chapter 7 for dealing with the multiple scales of input data, in respect with the representative scale of the involved physical processes. The Multi-Scale Surface Energy Balance System (MSSEBS) principle has been implemented into SEBS, and applied to an area of 2.5 million square kilometers including the Tibetan Plateau and the headwaters of the major rivers of eastern and southern Asia. The combination of continuous LST gap-filled observations with advanced land surface parameters and atmospheric fields, allowed to compute a 3-years time-series (2008-2010) of instantaneous land surface turbulent heat fluxes at a daily frequency. Two methods for the scaling of daily evapotranspiration (ET_d) were evaluated (Jackson et al., 1983; Crago, 1996a) in order to retrieve the most accurate daily rate from the extrapolation of one estimation over the diurnal period .

Results have been then evaluated against heat flux measurements provided by Eddy Covariance systems at four locations over the Tibetan Plateau. The scaling method proposed by Jackson et al. (1983), for a daily integration based on a sine function, clearly showed a better agreement with ground measurements. However, during the monsoon season, the integration of hourly heat flux calculations gave much better results, by taking into account the daily pattern of net radiation affected by cloud coverage. Moreover, the z_{0m} model, as proposed in Chapter 6 over the Heihe basin, has slightly improved the estimation of heat fluxes for hilly areas. MSSEBS has demonstrated to be much more sensitive to the difference

of atmospheric fields provided as an input. For some locations, the RMSE in the estimation of ET_d can be up to two times greater following the atmospheric data chosen.

Finally, this validation should be considered somehow as indicative since, even if calculations are performed for a spatial resolution of 1 km^2, LST pixels represent an area of 25 km^2 which is difficult to compare with the footprint of an EC system. Moreover, ground stations are too close and not sufficiently sparse through the Tibetan Plateau, and prevent to validate MSSEBS results for different surface conditions.

8.2 Perspectives

The investigations on roughness length retrieval in Chapter 4 are a first attempt to use very high resolution LIDAR data (i.e. digital elevation and surface models) over the complex land cover of the Yingke area. However, this investigation still suffers of some limitations. First, several case studies should be explored, but this aspect is compromised by the absence of other acquisitions available over the Yingke area. Then, the choice of a proper computing spatial resolution for both CFD-based and geometrical methods has to be addressed. Concerning the CFD model, a perspective of improvement could be the use of full-waveform data, in order to account for obstacle porosity in the propagation of airflow. A similar model dedicated to thermodynamic applications would be also very promising for a precise characterization of both roughness length for momentum and heat transfer at the local scale. Also, the study presented in Chapter 5 should be conducted for various type of landscape, with for instance the presence of hilly surfaces, or of major obstacles in the surroundings such as tall tree rows in the Yingke area.

More generally, all the evaluations conducted in Chapters 5 and 6 have to be repeated over longer time periods, in order to perform a real assessment of the potential of each z_{0m} and kB^{-1} models. At the local scale, this aspect is quite difficult since the experimental design and the required materials are relatively substantial. However, at the scale of the Heihe river basin (or somewhere else), it is more feasible with the exploitation of long-term ESA archives for bi-angular VNIR and TIR observations. The coming next satellite missions will also make it possible in the future.

Finally, as mentioned in Chapters 6 and 7, the use of Large Aperture Scintillometers for the turbulent heat flux measurements should be a requirement when evaluating calculations made at a square kilometer spatial resolution. Moreover, whatever is the scale of the study area, it appears important to address the evaluation of an algorithm such as MSSEBS (or SEBS) over several ground stations, and if feasible for a wide range of landscapes.

Résumé

Introduction

L'évapotranspiration (ET) des surfaces continentales représente un paramètre clé dans la clôture du bilan hydrologique, ainsi que pour la gestion de l'eau. L'évapotranspiration est un terme commun pour les bilans hydrologique et d'énergie de la surface, puisque la quantité d'eau évaporée correspond à l'énergie consommée lors du passage de la phase liquide à la phase gazeuse. Le transport de vapeur est donc est donc associé au transport de chaleur (latente). Le flux de chaleur latente est alors défini comme le transfert d'énergie circulant par unité de temps qui est représenté par la vaporisation de l'eau depuis la surface du sol vers l'atmosphère. L'évapotranspiration est contrôlée par l'humidité du sol, le type de végétation et son état de croissance, l'énergie disponible à la surface et par l'état de l'atmosphère.

Il est donc important de déterminer précisément le partitionement de l'énergie disponible entre les flux de chaleur sensible (réchauffement ou refroidissement de la surface) et de chaleur latente (évapotranspiration de la surface) pour un ensemble d'échelles spatiales et temporelles. L'observation et la modélisation des flux de chaleur turbulents issus des surfaces continentales ont été un domaine de recherche très actif depuis les travaux de Bowen (1926) sur l'amplitude relative du transfert de chaleur pour des surfaces sèches et humides (Monteith, 1965; Feddes, 1971; Verma et al., 1976; Hall et al., 1979; Price, 1982; De Bruin and Jacobs, 1989; Beljaars and Holtslag, 1991; Lhomme et al., 1994). La plupart des techniques conventionnelles qui utilisent des mesures ponctuelles pour estimer les termes du bilan d'énergie, sont représentatives uniquement à l'échelle locale, et ne peuvent donc pas être étendues à des échelles plus larges en raison de l'hétérogénéité de la surface, ainsi que de la nature dynamique et de la distribution spatiale du transfert de chaleur.

La télédétection, avec sa capacité de couverture spatiale étendue et de fréquence de revisite régulière, est devenue un outil puissant et de plus en plus utilisé dans le suivi des changements terrestres et environnementaux. Les propriétés des surfaces continentales telles que l'albédo, la fraction du couvert végétal, la température de

surface, obtenues à partir des données d'Observation de la Terre (OT) dans le domaine spectral optique (i.e. du visible, proche-infrarouge, jusqu'à l'infrarouge thermique) sont utilisées dans de nombreux modèles traitant des processus hydrologiques, météorologiques et écologiques. L'estimation et le suivi de l'ET par télédétection est également devenu une application courante.

Échange de chaleur à l'interface sol-atmosphère

L'énergie disponible à la surface se dissipe de trois manières. Une fraction pénètre dans le sol par conduction et le réchauffe, c'est le flux de chaleur dans le sol. L'énergie restante se dissipe en direction de l'atmosphère sous forme d'échange convectif turbulent. Le partitionnement vers l'atmosphère entre le flux de chaleur sensible et le flux de chaleur latente est fonction de l'eau présente dans la partie supérieure du sol et disponible pour l'évapotranspiration. La répartition du rayonnement net à la surface entre ces trois flux de chaleur est dépendante des propriétés et de l'état de la surface. Selon le type de sol et son occupation, les propriétés de la surface telles que l'albédo et l'émissivité varient et modifient son bilan radiatif. L'état de la surface tel que l'humidité, l'activité végétale et la couverture neigeuse conditionnent fortement le bilan radiatif et se traduit par une variation de la température de surface, de l'énergie disponible pour les flux turbulents et de leur partitionnement. La variation spatiale de l'état et des propriétés constitue l'hétérogénéité de la surface. Aussi, l'hétérogénéité des surfaces n'est pas uniquement à considérer dans la dimension horizontale, elle est également dépendante du relief, qui influe sur les paramètres bioclimatiques, ainsi que sur l'exposition au rayonnement atmosphérique. La distance à partir de laquelle on observe des variations significatives est appelée longueur d'échelle. Quelle que soit l'échelle considérée, l'hétérogénéité de la surface se traduit au sein de l'atmosphère.

Les échanges turbulents s'opèrent entre la surface et un niveau atmosphérique appelé couche limite atmosphérique, elle correspond à la partie basse de la troposphère qui est en interaction avec la surface. Au-delà, l'atmosphère est libre et ses mouvements ainsi que son état thermodynamique ne sont plus dépendants de la surface. La hauteur de la couche limite a un cycle journalier pour lequel elle est maximale, en raison des flux de chaleurs turbulents provenant de la surface au cours de la journée. Elle agit comme un intégrateur des éléments échangés, son évolution est donc progressive face à la forte variabilité spatiale et temporelle des flux en surface. Son état a un effet rétroactif car il détermine les gradients de température et d'humidité et donc les flux. Cette interaction entre la couche limite et la surface tend alors vers une situation d'équilibre, lorsque que toute la couche est mélangée. On considère alors deux échelles pour les propriétés de la couche limite (McNaughton and Raupach, 1996) : le temps nécessaire pour atteindre un

équilibre (échelle de temps caractéristique), et la longueur de la surface intégrée par la couche limite en équilibre (longueur d'échelle atmosphérique). Cependant, la couche limite atmosphérique n'a pas une structure uniforme, on distingue (Brutsaert, 1982) :

- la couche de surface, située à l'interface sol-atmosphère, très influencée par l'hétérogénéité de la surface et dont la hauteur est déterminée par les flux de chaleur échangés entre la surface et l'atmosphère.

- la couche de mélange, partie supérieure où la masse d'air est plus homogène, et dont le mouvement est déterminé par l'état de la surface et la rotation terrestre.

Le flux de chaleur sensible est fonction du gradient de température entre la surface et un niveau atmosphérique de référence. Dans le cas d'une surface homogène et infinie, on suppose que la masse d'air est en équilibre avec cette surface et qu'une mesure de température à un niveau donné est représentative de la température de la masse d'air en tout point à ce niveau. Cependant, pour des conditions atmosphériques identiques, le partitionnement et la densité des flux de chaleur échangés entre la surface et l'atmosphère varient fortement en milieu hétérogène. Ainsi, chaque élément de la surface créant sa propre couche limite interne, on considère que la mesure de température de référence doit se faire à un niveau de référence tel que les hétérogénéités soient intégrées dans la couche de mélange. Toutefois, il est peu probable que le gradient mesuré soit représentatif des flux turbulents échangés par la surface sous-jacente dans la mesure où la couche de surface est perturbée par l'hétérogénéité environnante.

Bien que la mesure des flux de chaleur soit réalisable à l'échelle d'une station météorologique pour des surfaces homogènes, elle est cependant impossible de manière spatialisée (sur l'ensemble d'un bassin versant par exemple). L'utilisation de modèles atmosphériques méso-échelle couplés avec des modèles de surface permettent de simuler l'évolution tridimensionnelle des flux turbulents au cours du temps. Toutefois, ce type de modèle nécessite de nombreuses variables en entrée, une assimilation éventuelle de données et un temps de calcul important. Par ailleurs, les données d'observation de la Terre ont démontrées leur utilité pour la spatialisation de l'évapotranspiration et de nombreuses études ont permis de développer différents algorithmes pour l'estimation du bilan d'énergie des surfaces naturelles et cultivées (revue par Li et al. (2009c). Les données acquises dans le visible et proche infrarouge permettent de retrouver l'albédo de la surface, qui associé à la température de surface mesurée dans l'infrarouge thermique, permettent la spatialisation du bilan radiatif. Les variables telles que la fraction du couvert végétal (f_c) ou le Leaf Area Index (LAI) permettent de caractériser l'état

de la surface et sont utiles dans la définition de paramètres clés pour l'estimation des transferts de chaleur (Choudhury et al., 1987; Su et al., 2001).

Algorithme de calcul du bilan d'énergie

La plupart des algorithmes proposés permettent le partitionnement des flux turbulents entre une limite humide et une limite sèche qui s'expriment par le gradient de température normalisé entre la surface et l'atmosphère à un niveau de référence (Li et al., 2009c). Ce concept proposé par Menenti and Choudhury (1993) est appelé Surface Energy Balance Index (SEBI). Les conditions aux limites sont soit observées (Bastiaanssen et al., 1998; Roerink et al., 2000), soit calculées (Su, 2002; Jia et al., 2003a; Colin, 2006). Ce type d'approche représente un outil d'estimation du bilan d'énergie de la surface relativement simple à mettre en oeuvre et qui nécessite relativement peu de données en entrée ainsi que de temps de calcul.

L'algorithme intitulé Surface Energy Balance System (SEBS) formulé par Su (2002) est un schéma de paramétrisation basé sur le concept du SEBI, qui est reconnu pour son utilisation aussi bien à l'échelle locale que régionale, et ce pour n'importe quelle condition de stabilité atmosphérique. L'association de données de télédétection acquises dans les domaines du visible, proche infrarouge (albédo, NDVI, LAI, f_c) et infrarouge thermique (température de surface) avec la mesure du rayonnement à la surface et de variables atmosphériques à une niveau de référence (température, vitesse du vent, humidité spécifique) permet de calculer les gradients observés de température, ainsi que ceux aux limites, entre la surface et l'atmosphère à l'échelle du pixel. Su (2002) propose également l'adaptation du choix des fonctions de stabilité selon si la hauteur de référence considérée est située dans la couche de surface ou dans la couche de mélange (Brutsaert, 1999).

Indépendamment des erreurs liées à la mesure des différentes variables atmosphériques ou aux modèles permettant de retrouver les paramètres de surface (température, albédo, LAI), SEBS est sensible à la paramétrisation de la résistance aérodynamique, c'est à dire la résistance au transfert de chaleur au sein d'une couche d'atmosphère. L'expression de la résistance aérodynamique requiert le calcul de la longueur de rugosité au transfert de quantité de chaleur (z_{0h}), et par conséquent celle au transfert de quantité de mouvement (z_{0m}) par l'intermédiaire du modèle de kB^{-1} (Massman, 1999). La longueur de rugosité est dépendante du profil vertical de vent, est influencée par la géométrie de la surface et variable dans l'espace et dans le temps. Or, les modèles de rugosité pour l'estimation de z_{0m} utilisés dans SEBS sont définis à partir de relations empiriques basées généralement sur le NDVI et pour certains types des couverts homogènes. Leur utilisation pour la caractérisation de surfaces hétérogènes est donc hors de leur domaine de

validité. De plus, ces modèles ne prennent pas en compte le caractère dynamique de la longueur de rugosité. Su et al. (2001) reconnait alors que l'utilisation des modèles d'estimation de longueur de rugosité n'est pas toujours appropriée dans la mesure où ils ne tiennent pas compte de l'historique de l'écoulement de la masse d'air en milieu hétérogène.

Dans la cas d'études régionales, la capacité d'échantillonnage des capteurs spatiaux devient grossière (e.g. 1 km) et le maillage des données atmosphériques est encore plus lâche. A cette échelle, nous considérons que l'effet d'agrégation de l'hétérogénéité de la surface ainsi que des masses d'air, ne permet pas de considérer la rugosité locale de la surface, au moins pour les surfaces naturelles, puisque les surfaces urbaines étendues ne sont pas abordées dans ce travail. Menenti et al. (1996) considèrent qu'il existe une échelle régionale à partir de laquelle la longueur de rugosité est indépendante de la direction du vent, permettant alors l'utilisation d'une définition statique de ce paramètre. Les principaux obstacles à l'écoulement de l'air sont représentés par l'alternance de sol nu (lisse) et de végétation (plus ou moins rugueuse), et évidemment par le relief. La rugosité due à l'élévation reste constante au cours du temps, en revanche celle induite par la végétation présente un cycle annuel, plus ou moins important en fonction du type de végétation et du climat.

Au delà de la caractérisation de la géométrie de la surface, qui est plutôt limitée à grande échelle, d'autres problèmes émergent. Les études méso-échelle reposent sur le combinaison de données d'OT dans le domaine du visible, du proche infrarouge et de l'infrarouge thermique avec des champs atmosphériques au nivau de la couche limite, qui ont tous leur propre résolution spatiale. Une des difficulté majeure est de définir l'échelle appropriée (i.e. la longueur d'échelle atmosphérique) pour le calcul de la résistance aérodynamique au transfert de chaleur et de ses longueurs de rugosité associées (z_{0m}, z_{0h}), entre une étendue atmosphérique et la surface sous-jacente.

Par ailleurs, la plupart des algorithmes de bilan d'énergie utilisant des données de télédétection produisent des valeurs d'évapotranspiration instantanée. Il est évidemment nécessaire de convertir la valeur instantanée d'ET calculÃl'e au moment du passage du satellite, en une valeur journalière ou à une échelle de temps plus longue, pour un usage davantage important dans des applications hydrologiques. De plus, l'avantage de travailler avec des données ayant une résolution spatiale moyenne ou faible, est que la résolution temporelle pour l'observation des surfaces continentales et le suivi des flux de chaleur peut considérablement augmenter. Dans un tel contexte, le calcul du bilan d'énergie peut facilement atteindre une base journalière, voire même horaire avec les satellites géostationnaires, ce qui est très convenable pour mener des investigations sur les stratégies d'intégration temporelle.

Objectifs de la thèse

D'après la discussion précédente, quelques questions peuvent être soulevées et les objectifs de cette thèse seront d'y répondre. Ces questions sont formulées de la manière suivante :

- Est-ce que la caractérisation géométrique de la surface permet une meilleure estimation des variables impliquées dans les échanges turbulents de chaleur entre le sol et l'atmosphère ?

- Peut-on améliorer la caractérisation du transfert de masse et de chaleur sur des surfaces hétérogènes par la prise en compte des aspects dynamiques de la circulation de l'air ?

- Est-ce qu'une meilleure caractérisation de la rugosité à grande échelle (i.e. le relief) a une influence sur l'estimation des flux de chaleur turbulents ?

- Est-ce que l'algorithme SEBS est adapté pour le suivi des flux de chaleurs à large échelle et à une fréquence temporelle élevée ?

L'ensemble de ces questions sera abordé grâce à l'exploitation d'un panel important de données de télédétection. Les différents processus et propriétés de la surface doivent alors être caractérisés à une résolution spatiale appropriée. Cependant, une résolution spatiale plus élevée implique inévitablement une résolution temporelle plus faible, et donc la réduction des cas d'étude. Ce travail de thèse est donc structuré conformément à cette considération, et sera détaillé dans les paragraphes suivants, puis synthétisé par la Figure 1.1.

Le travail consiste dans un premier temps en la caractérisation locale de la géométrie de la surface à l'aide d'un modèle numérique de surface (MNS) obtenu par les acquisitions d'un système LIDAR imageur. L'introduction du modèle de surface dans une modèle de mécanique des fluides (CFD) permettra de générer des champs de vent tridimensionnels. L'inversion de chaque profil vertical de vent produira une spatialisation de la longueur de rugosité au transfert de quantité de mouvement (z_{0m}). Deux autres approches géométriques prenant en compte la direction du vent seront également appliquées au modèle de surface.

Dans le but d'évaluer la fiabilité et la précision des modèles géométriques et de la méthode basée sur l'utilisation du CFD pour l'estimation de la longueur de rugosité, ceux-ci seront comparés à trois autres formulations simplifiées et qui correspondent à une définition statique de z_{0m}. L'évaluation sera effectuée à l'aide de différentes simulations SEBS des flux de chaleur turbulents, intégrant respectivement les valeurs de rugosité spatialisées. La performance de chaque méthode sera alors déterminée en comparant les résultats avec les mesures de flux de chaleur

réalisées au sol. De plus, les simulations SEBS requièrent la combinaison des propriétés de la surface (albédo, température, émissivité, LAI, et f_c) avec les mesures atmosphériques (température de l'air, vitesse du vent, humidité spécifique, pression, rayonnement). Les variables de surface doivent être retrouvées à partir des observations aéroportées très haute résolution dans le domaine du visible, proche infrarouge et infrarouge thermique.

L'évaluation de l'estimation de z_{0m} doit être étendue au delà du contexte local d'une station météorologique, puisque beaucoup d'études hydrologiques ont pour but la modélisation du cycle de l'eau à l'échelle régionale, continentale, ou encore globale. En ce sens, une méthode d'estimation capable de prendre en compte l'influence du relief pour des applications à grande échelle doit être proposée. De plus, puisque la résistance aérodynamique est sensible aux deux longueurs de rugosité pour le transfert de quantité de chaleur et de mouvement, il apparait évident d'évaluer au moins deux modèles de kB^{-1} dans SEBS. Ces deux aspects mènent alors à une intéressante analyse croisée des paramétrisations de z_{0m} et de z_{0h} (à travers le modèle de kB^{-1}) à différentes échelles spatiales.

L'aspect final de ce travail sera de combiner des produits avancés de propriétés de la surface, avec des observations de température du sol à la mi-journée et les variables atmosphériques correspondantes pour le calcul des flux de chaleur instantanés à une fréquence journalière sur l'ensemble du plateau tibétain. Cela implique également de définir une longueur d'échelle pour le calcul des résistances aérodynamiques, qui doit être cohérente à la fois avec la résolution spatiale des données fournies en entrée, et avec les processus impliqués. A partir des calculs de bilan d'énergie instantanés, une stratégie d'intégration capable de reproduire le comportement diurne des flux de chaleur doit être sélectionnée dans le but de fournir un taux d'évapotranspiration journalier fiable. La disponibilité d'observations horaires et reconstruites (obstruction par les nuages) ainsi que de variables atmosphériques, pour des simulations SEBS à haute fréquence, permet d'explorer le bénéfice de leur intégration sur l'ensemble de la journée, et principalement en conditions nuageuses lorsque le forçage radiatif et la réponse de la surface sont changeants.

Organisation du document

Le Chapitre 2 est dédié à l'estimation de l'évapotranspiration par télédétection. La théorie liée à la modélisation des flux d'énergie est d'abord décrite. Ensuite, le concept du Surface Energy Balance Index (SEBI) proposé par Menenti and Choudhury (1993) est expliqué, puisqu'il est principalement à l'origine du Surface Energy Balance System élaboré par Su (2002), et donc essentiel pour la compréhension de l'approche conceptuelle. Une rapide description de l'algorithme

SEBS est également donnée.

Le Chapitre 3 présente d'abord l'ensemble des sites d'étude : le bassin versant du Heihe ainsi que les stations expérimentales d'A'rou et du Yingke, puis le Plateau du Tibet et ces quatre stations d'observations. Les différentes données utilisées dans ce travail sont ensuite détaillées : les données de télédétection spatiale et aéroportée, les variables météorologiques observées et simulées.

Dans le Chapitre 4, les investigations sur l'estimation de la longueur de rugosité pour le transfert de quantité de mouvement sont décrites (Colin and Faivre, 2010). L'exploitation de données LIDAR spatialisées permet de produire des modèles numériques d'élévation et de surface à très haute résolution (MNT & MNS). Le MNS met en évidence la micro-topographie locale telle que la structure de la végétation, et est très adapté pour l'application de deux modèles géométriques d'estimation de la rugosité proposés respectivement par Raupach (1994) et MacDonald et al. (1998). Le modèle de surface permet également de mener des expérimentations sur l'inversion de champs de vent générés par un modèle de mécanique des fluides (Lopes, 2003).

Le Chapitre 5 aborde premièrement la production des paramètres de surface à partir des données aéroportées très haute résolution. Les méthodes proposées dans le Chapitre 4 (géométriques et aérodynamiques) pour l'estimation de la longueur de rugosité sont ensuite évaluées à travers des simulations SEBS. Trois autres formulations simplifiées pour l'estimation de z_{0m} sont aussi incluses dans le but d'évaluer si la prise en compte des effets dynamiques permet une meilleur caractérisation du transfert de chaleur, comparé à une définition statique. Ce travail sera réalisé à l'échelle de l'aire de contribution des flux turbulents mesurés au sol (système Eddy Covariance).

Dans le Chapitre 6, les paramétrisations de z_{0m} et de kB^{-1} sont évaluées à travers une évaluation croisée. Deux méthodes d'estimation de la rugosité plutôt prometteuses, ainsi que deux modèles de kB^{-1} sont comparés à l'aide d'un ensemble de simulations SEBS. La même étude est réalisée à une échelle spatiale plus grande, avec des méthodes d'estimation de z_{0m} spécifiques pour la prise en compte du relief et/ou de la végétation. Un pré-traitement pour l'obtention des paramètres de la surface à l'échelle régionale est toujours nécessaire, dont la procédure spécifique sera détaillée.

Le Chapitre 7 traite de la capacité de SEBS à produire des séries temporelles d'évapotranspiration méso-échelle, avec la démonstration sur l'ensemble du Plateau du Tibet pour la période 2008-2010. L'approche multi-échelle proposée par Colin (2006) est appliquée à SEBS afin de traiter convenablement avec les différentes résolutions spatiales. Ensuite, à partir d'une estimation des flux de chaleurs turbulents par jour, deux méthodes d'intégration journalière de l'ET sont évaluées. Des calculs, basés sur des observations horaires de la température de la surface, sont également produits pour un mois complet, dans le but d'évaluer le

bénéfice des intégrations horaires. Les validations reposent sur la comparaison avec les mesures de flux réalisées sur les quatre sites d'observation situés sur le Plateau du Tibet.

Le Chapitre 8 correspond à la conclusion générale de cette thèse. Il rappelle les principaux objectifs de ce travail, et résume les résultats obtenus ainsi que les observations faites respectivement dans chaque chapitre. Les améliorations et les perspectives envisageables pour la poursuite de ce travail sont également abordées.

Réalisations

La paramétrisation du transfert de chaleur par télédétection, basée sur le schéma SEBS, s'est déjà avérée très adaptée pour l'estimation de l'évapotranspiration (ET) sur des surfaces naturelles homogènes. Cependant, l'utilisation d'une telle méthode pour des paysages hétérogènes (e.g. régions semi-arides ou surfaces agricoles) est plus délicate, puisque le principe de la théorie de la similarité est compromis par la présence de différentes sources de chaleur et de hauteurs variées. Dans un premier temps, cette thèse a pour objectif de proposer et d'évaluer différents modèles basés sur la géométrie de la végétation qui permettent d'estimer la longueur de rugosité pour le transfert de quantité de mouvement à la surface (z_{0m}), cette dernière étant un paramètre clé dans la caractérisation du transfert de chaleur. En revanche, une telle investigation ne peut être menée qu'à une petite échelle et à l'aide de données de télédétection très haute résolution permettant ainsi une description très détaillée de la surface. Ensuite, le second aspect de ce travail est de déterminer de quelle manière estimer la longueur de rugosité dans le cas d'études régionales, et plus généralement, de vérifier si l'algorithme SEBS est adapté pour l'estimation des flux de chaleur turbulents à de grandes échelles spatiales et temporelles.

A l'échelle locale (Chapitre 4), l'extraction d'un modèle digital de surface à partir de données LIDAR, puis son association avec des mesures de vent dans un modèle CFD, ont permis de reproduire des champs de vent tridimensionnels sur la zone d'étude du Yingke. Des cartes de longueur de rugosité au transfert de quantité de mouvement ont été générées par l'inversion des profils de vent (Equation 4.1). Cette approche aérodynamique est très sensible à la vitesse et à la direction du vent données en entrée du modèle CFD, et tient compte de l'historique du flux d'air en amont (e.g. effet d'abri lié aux brise-vent, ou inversement, des surfaces planes sans obstacles). Deux approches géométriques (Raupach, 1994; MacDonald et al., 1998), tenant compte de la direction du vent et de la topographie, ont également été implémentées dans un même outil informatique. Il apparaît que les valeurs de longueur de rugosité obtenues sont plutôt similaires pour les deux ap-

proches géométriques, et ne varient pas significativement avec l'orientation du vent sur la zone d'étude du Yingke.

Ensuite, l'évaluation des méthodes d'estimation de la longueur de rugosité dans le Chapitre 5 est réalisée à l'échelle de l'aire de contribution intégrée par les flux de chaleur mesurés. Trois autres modèles (semi-)empiriques pour l'estimation de z_{0m} ont été ajoutés dans cette évaluation (Moran, 1990; Brutsaert, 1982; Menenti and Ritchie, 1994). L'évapotranspiration de surface est alors calculée grâce à la combinaison d'acquisitions aéroportées VIS-PIR & IRT avec des mesures météorologiques effectuées au sol, ainsi qu'avec les différentes données de longueur de rugosité. La paramétrisation basée sur la méthode CFD permet d'obtenir une meilleure estimation du flux de chaleur sensible à l'échelle de la station météorologique. En revanche, la formulation proposée par Brutsaert (1982) permet un partitionnement du rayonnement net légèrement meilleur. De plus, cette dernière formulation a été élaborée pour des surfaces relativement homogènes telles que les alentours immédiats de la station de mesure du Yingke.

Puisque la validation spatiale basée sur l'aire de contribution aux flux de chaleur mesurés n'a été possible que pour une occurrence, deux séries temporelles comprenant deux semaines de mesures de flux, ainsi que leur estimation par SEBS, ont été réalisées et comparées à l'échelle de la station météorologique. Cette évaluation temporelle a permis de confirmer les résultats précédents, mais également que le modèle de kB^{-1} (Massman, 1999; Su et al., 2001), essentiel pour déterminer la longueur de rugosité au transfert de quantité de chaleur (z_{0h}) à partir de z_{0m}, n'est pas adapté pour les configurations géométriques et aérodynamiques complexes. De plus, afin de réellement évaluer le potentiel de la méthode basée sur l'utilisation du modèle CFD face à la relation simple proposée par Brutsaert (1982), la même étude devrait être menée pour différents sites et avec des paysages variés.

L'évaluation additionnelle réalisée dans le Chapitre 6 est d'abord concentrée sur l'utilisation de la méthode dite CFD et de celle proposée par Brutsaert (1982) pour le calcul de la longueur de rugosité, avec l'intégration d'un nouveau modèle de kB^{-1} (Jia, 2004). Ce dernier est basé sur l'hétérogénéité thermique de la surface, mise en évidence au moyen de mesures bi-angulaires (i.e. 0° et +53°) de la température de surface (LST) et de la fraction du couvert (f_c). De tels dispositifs n'ont pas été installés sur la station météorologique du Yingke, mais des observations de température de la végétation et du sol nu ont été réalisées. D'après Norman et al. (1995) et Menenti et al. (2001), le comportement angulaire de la température de surface et de la fraction du couvert peut être reconstruit à partir de ces mesures au sol. Ensuite, l'évaluation temporelle des flux de chaleur estimés a confirmé les conclusions faites dans le Chapitre 5 à propos de la fiabilité des méthodes basées sur le modèle CFD et celui de Brutsaert (1982), même si les RMSE sont plus grandes avec l'utilisation du modèle de kB^{-1} proposé par Jia (2004).

De plus, ce dernier se révèle adapté uniquement lorsque la surface présente un contraste thermique important.

Cette évaluation a été ensuite transposée à l'échelle du bassin du Heihe, qui est très approprié pour évaluer tant la caractérisation de z_{0m} sur de grandes étendues, que le modèle alternatif de kB^{-1} avec l'utilisation de données AATSR biangulaires. Deux modèles de z_{0m} sont alors retenus : la méthode de Moran (1990), basée sur le NDVI, et la formulation modifiée de Menenti and Ritchie (1994), qui intègre la végétation (NDVI) ainsi que le relief (MNT). Une analyse croisée permet d'évaluer conjointement les deux modèles de rugosité, ainsi que les deux modèles de kB^{-1}. De cette démarche expérimentale, il est apparu que :

- le modèle formulé par Jia (2004) produit de plus grandes valeurs de kB^{-1} pour les zones végétalisées, et est moins sensible aux variations des valeurs de z_{0m}.

- le modèle de z_{0m}, adapté de Menenti and Ritchie (1994), fournit évidemment des estimations de longueur de rugosité plus élevées pour les zones montagneuses, et stables pour des terrains plats.

- le modèle original de kB^{-1}, intégré dans SEBS (Su, 2002), fournit un partitionnement des flux de chaleur légèrement meilleur pour les surfaces planes telles que la zone du Yingke.

- le second modèle de kB^{-1} (Jia, 2004), combiné à la formulation modifiée de z_{0m} (Menenti and Ritchie, 1994), permet un partitionnement très précis des flux de chaleur turbulents pour les zones montagneuses.

Il est évidemment intéressant d'évaluer la fiabilité de chaque modèle de z_{0m} sur les zones à forte rugosité de surface. Cependant, la représentatitivité des mesures de flux par système Eddy Covariance, pour évaluer des estimations kilométriques, semble faible en raison de la complexité du terrain et des effets locaux induits.

Par ailleurs, dans la perspective d'études à large échelle, et pour le suivi à long terme de l'évapotranspiration de surface, l'algorithme SEBS a été adapté dans le Chapitre 7 pour traiter les différentes résolutions des données d'entrée, dans le respect de l'échelle représentative des processus physiques impliqués. Le principe du Multi-Scale Surface Energy Balance System (MSSEBS) a été implémenté dans SEBS et appliqué à une zone de 2,5 millions kilomètres carrés, incluant le Plateau du Tibet et l'amont des principaux fleuves de l'Asie orientale et méridionale. La combinaison d'observations continues de température de surface avec des paramètres de surface avancés et des champs atmosphériques, permet de calculer une série temporelle de trois années (2008-2010) des flux turbulents instantanés à une fréquence journalière. Deux méthodes pour la transformation

en évapotranspiration journalière (ET_d) ont été évaluées (Jackson et al., 1983; Crago, 1996a) afin de calculer un taux journalier le plus précis possible à partir de l'extrapolation d'une estimation réalisée au cours de la période diurne.

Les résultats sont évalués à l'aide des mesures de flux de chaleur fournies par les systèmes Eddy Covariance pour quatre sites localisés sur le Plateau du Tibet. La méthode proposée par Jackson et al. (1983), une intégration journalière basée sur une fonction sinus, présente très clairement un meilleur accord avec les mesures au sol. Cependant, durant la mousson, l'intégration de calculs horaires des flux de chaleur fournit de bien meilleurs résultats que les deux méthodes précédentes, grâce à la prise en compte du comportement journalier du rayonnement net affecté par la couverture nuageuse. De plus, le modèle de z_{0m} tel que proposé dans le Chapitre 6 sur le bassin du Heihe, permet de légèrement améliorer l'estimation des flux de chaleur pour les zones montagneuses. MSSEBS est par ailleurs davantage sensible aux différents champs atmosphériques fournis en entrée. Pour certains sites, les RMSE dans l'estimation de l'ET_d peuvent être jusqu'à deux fois plus grandes en fonction des données atmosphériques choisies.

En définitive, cette validation devrait en quelque sorte être considérée comme indicative puisque, bien que les calculs soient réalisés à une résolution spatiale d'un kilomètre carré, chaque pixel de température de surface représente une aire de vingt-cinq kilomètres carrés. Cela est donc difficilement comparable avec l'aire de contribution intégrée par les systèmes de mesure Eddy Covariance. De plus, les stations de mesure au sol sont trop proches et pas assez disséminées à travers le Plateau du Tibet, ce qui ne permet pas de valider les résultats issus de MSSEBS pour des conditions de surface rigoureusement différentes.

Perspectives

Les investigations sur l'estimation de la longueur de rugosité présentées dans le Chapitre 4 sont une première tentative pour l'utilisation de données LIDAR très haute résolution (i.e. modèle digital d'élévation ou de surface) sur le paysage complexe du Yingke. Cependant, cette investigation souffre encore de quelques limitations. Premièrement, plusieurs cas d'étude devraient être explorés, mais cet aspect est compromis par l'absence d'autres acquisitions disponibles sur le site du Yingke. Ensuite, le choix d'une résolution de calcul appropriée tant pour la méthode CFD que pour les méhodes géométriques doit être étudié. Concernant le modèle CFD, une perspective d'amélioration pourrait être l'utilisation des données LIDAR complètes dans le but de prendre en compte la porosité des obstacles dans la propagation du flux de la masse d'air. Un modèle similaire mais dédié à des applications thermodynamiques serait également prometteur pour la caractérisation précise des longueurs de rugosité au transfert de quantité de mouve-

ment et de quantité de chaleur à l'échelle locale. De plus, l'étude présentée dans le Chapitre 5 devrait être menée pour différents types de paysage avec, par exemple, la présence de collines ou d'obstacles majeurs environnants, tels que les imposantes haies présentes dans la zone du Yingke.

Plus généralement, l'ensemble des évaluations conduites dans les Chapitre 5 et 6 doivent être répétées sur de plus longues périodes, dans le but de réaliser une réelle évaluation du potentiel de chaque modèle d'estimation de z_{0m} et de kB^{-1}. A l'échelle locale, cet aspect est plutôt difficile puisque la démarche expérimentale et le matériel requis sont relativement considérables. Cependant, à l'échelle du bassin du Heihe (ou ailleurs) cela est davantage réalisable avec l'exploitation des observations bi-angulaires VIS-PIR & IRT dans les archives de l'ESA. Les prochaines missions satellites le permettront également dans le futur.

Enfin, comme il est mentionné dans les Chapitres 6 et 7, l'utilisation de scintillomètres à grande ouverture pour la mesure des flux de chaleur turbulents est nécessaire pour l'évaluation des estimations réalisées à une résolution spatiale d'un kilomètre carré. Quelle que soit l'échelle de l'aire d'étude, il est aussi important d'évaluer les résultats d'un algorithme tel que MSSEBS (ou SEBS) à l'aide de plusieurs stations au sol, et dans la mesure du possible pour une grande variété de paysages.

References

Arya, S. P. S. (1975). A drag partition theory for determining the large-scale roughness parameter and wind stress on the arctic pack ice. *Journal of Geophysical Research*, 80(24):3447–3454.

Babel, W., Eigenmann, R., Ma, Y., and Foken, T. (2011). Analysis of turbulent fluxes and their representativeness for the interaction between the atmospheric boundary layer and the underlying surface on tibetan plateau. Technical report, CEOP-AEGIS Deliverable Report De1.2, University of Strasbourg, France, ISSN 2118-7843: 35p.

Babel, W., Li, M., Sun, F., Ma, Y., Chen, X., Colin, J., Ma, Y., and Foken, T. (2012). Aerodynamic and thermodynamic variables for four stations on tibetan plateau – introduction on the ceop-aegis database in netcdf. Technical report, CEOP-AEGIS Deliverable Report De1.3, University of Strasbourg, France, ISSN 2118-7843: 90p.

Baret, F., Clevers, J., and Steven, M. (1995). The robustness of canopy gap fraction estimates from red and near-infrared reflectances: a comparison of approaches. *Remote Sensing of the Environment*, 54:141–151.

Bastiaanssen, W. (1995). *Regionalization of surface flux densities and moisture indicators incomposite terrain: a remote sensing approach under clear skies in Mediterranean climates*. PhD thesis, Landbouwuniversiteit.

Bastiaanssen, W. and Bandara, K. (2001). Evaporative depletion assessments for irrigated watersheds in sri lanka. *Irrigation Science*, 21(1):1–15.

Bastiaanssen, W., Menenti, M., Feddes, R., and Holtslag, A. A. M. (1998). A remote sensing surface energy balance algorithm for land (sebal). 1. formulation. *Journal of Hydrology*, (212-213):198–212.

Bastiaanssen, W. G. M., Cheema, M. J. M., Immerzeel, W. W., Miltenburg, I. J., and Pelgrum, H. (2012). Surface energy balance and actual evapotranspiration

of the transboundary indus basin estimated from satellite measurements and the etlook model. *Water Resources Research*, 48:16.

Becker, F. and Li, Z.-L. (1995). Surface temperature and emissivity at various scales: definition, measurement and related problems. *Remote Sensing Reviews*, 12:225–253.

Beljaars, A. and Holtslag, A. (1991). Flux parameterization over land surfaces for atmospheric models. *Journal of Applied Meteorology*, 30(3):327–341.

Bisht, G. and Bras, R. L. (2010). Estimation of net radiation from the modis data under all sky conditions: Southern great plains case study. *Remote Sensing of Environment*, 114(7):1522–1534. Export Date: 9 August 2010 Source: Scopus.

Blumel, K. B. (1999). A simple formula for estimation of the roughness length for heat transfer over partly vegetated surfaces. *J. Appl. Meteorol.*, 38:814–829.

Bowen, I. S. (1926). The ratio of heat losses by conduction and by evaporation from any water surface. *Physics Review*, 27:2433–2443.

Brutsaert, W. (1982). *Evaporation into the atmosphere*. Kluwer Academic, Dordrecht, The Netherland, springer edition.

Brutsaert, W. (1999). Aspects of bulk atmospheric boundary layer similarity under free-convective conditions. *Reviews of Geophysics*, 37(4):439–451.

Brutsaert, W. and Sugita, M. (1992). Application of self-preservation in the diurnal evolution of the surface energy budget to determine daily evaporation. *J. Geophys. Res.*, 18(97):377–382.

Carlson, T., Dodd, J., Benjamin, S., and Cooper, J. N. (1981). Satellite estimation of the surface energy balance, moisture availability and thermal ldots. *Journal of Applied Meteorology*, 20:67–87.

Carlson, T. N. and Ripley, D. A. (1997). On the relation between ndvi, fractional vegetation cover, and leaf area index. *Remote Sensing of Environment*, 62:241–252.

Chamberlain, A. C. (1966). Transport of gases to and from grass and grass-like surfaces. *Proceedings of the Royal Society of London*, A290:236–265.

Chen, D. H., Xue, J. S., Yang, X. S., Zhang, H. L., Shen, X. S., Hu, J. L., Wang, Y., Ji, L. R., and Chen, J. B. (2008). New generation of multi-scale nwp system (grapes): general scientific design. *Chinese Science Bulletin*, 53(22):3433–3445.

Chen, F. and Dudhia, J. (2001). Coupling an advanced land surfaceâĂŘhydrology model with the penn stateâĂŘncar mm5 modeling system. part 1: Model implementation and sensitivity. *American Meteorological Society*, 129:569–585.

Chen, F., Mitchell, K., Schaake, J., Xue, Y., Pan, H., Koren, V., Duan, Y., Ek, M., and Betts, A. (1996). Modeling of landâĂŘsurface evaporation by four schemes and comparison with fife observations. *Journal of Geophysical Research*, 101:7251–7268.

Chen, S. H. and Sun, W.-Y. (2002). A one-dimensional time dependent cloud model. *Journal of the Meteorogical Society of Japan*, 80(99-118).

Choudhury, B. J., Idso, S. B., and Reginato, R. J. (1987). Analysis of an empirical model for soil heat flux under a growing wheat crop for estimating evaporation by an infrared-temperature based energy balance equation. *Agricultural and Forest Meteorology*, 39:283–297.

Choudhury, B. J., Reginato, R. J., and Idso, S. B. (1986). An analysis of infrared temperature observations over wheat and calculation of latent heat flux. *Agric. For. Meteorolog.*, 37:77–88.

Colaizzi, P. D., Evett, S. R., Howell, T. A., and Tolk, J. A. (2006). Comparison of five models to scale daily evapotranspiration from one-time-of-day measurements. *American Society of Agricultural and Biological Engineers*, 49(5):1409–1417.

Colin, J. (2006). *Apport de la télédétection optique à la définition d'indicateurs de performance pour l'utilisation de l'eau en agriculture*. PhD thesis, Université Louis Pasteur, Strasbourg.

Colin, J. and Faivre, R. (2010). Aerodynamic roughness length estimation from very high-resolution imaging lidar observations over the heihe basin in china. 14(12):none.

Colin, J., Menenti, M., Rubio, E., and Jochum, A. (2006). A multi-scales surface energy balance system for operational actual surface evapotranspiration. *AIP Conference Proceedings*, 852:178–184.

Colin, J., Roupioz, L., Ghafarian, H., Bai, J., Jia, L., Liu, S., Faivre, R., Nerry, F., and Menenti, M. (2011). Surface radiative and energy balance time-series processing and validation procedure document. Technical report, CEOP-AEGIS Deliverable Report De3.3, University of Strasbourg, France, ISSN 2118-7843: 34p.

Counehan, J. (1971). Wind tunnel determination of the roughness length as a function of the fetch and the roughness density of three-dimensional roughness elements. *Atmospheric Environment (1967)*, 5(8):637–642.

Covey, W. (1963). *A method for the calculation of logarithmic wind profile parameters and their standard errors*, chapter The Energy Budget at the Surface, Part II, Report No. 72, pages 28–33. USDA-ARS.

Crago, R. D. (1996a). Comparison of the evaporative fraction and the priestley-taylor alpha for paramererizing daytime evaporation. *Water Resources Research*, 32(5):1403–1409.

Crago, R. D. (1996b). Conservation and variability of the evaporative fraction during the daytime. *Journal of Hydrology*, 180:173–194.

Crago, R. D. and Brutsaert, W. (1996). Daytime evaporation and the serf-preservation of the evaporative fraction and the bowen ratio. *Journal of Hydrology*, 178:241–255.

De Bruin, H. A. R. and Jacobs, A. F. G. (1989). Forest and regional scale processes. *Philosophical Transactions of the Royal Society of London. Series B, Biological Sciences*, 1223, Forest, Weather and Climate(324):393–406.

De Vries, A. C., Kustas, W. P., Ritchie, J. C., Klaassen, W., Menenti, M., Rango, A., and Prueger, J. H. (2003). Effective aerodynamic roughness estimated from airborne laser altimeter measurements of surface features. *International Journal of Remote Sensing*, 24(7):1545–1558.

Dorren, L., Berger, F., and Maier, B. (2007). Mapping the structure of forestal vegetation with an airborne light detection and ranging (lidar) system in mountainous terrain [cartographier la structure de la vegetation forestiere avec un systeme lidar aeroporte en terrain montagnard]. *Revue Francaise de Photogrammetrie et de Teledetection*, (186):54–59.

Dudhia, J. (1989). Numerical study of convection observed during the winter monsoon experiment using a mesoscale two-dimensional model. *Journal of the Atmospheric Sciences*, 46:3077–3107.

Ek, M. (2003). Implementation of noah land sur- face model advances in the national centers for environmental predic- tion operational mesoscale eta model. *Journal of Geophysical Research : Atmospheres*, 108(D22):8851.

Faivre, R., Colin, J., Roupioz, L., Ghafarian, H., Li, Z., Jia, L., Nerry, F., and Menenti, M. (2012). Preliminary time-series maps of fluxes over 3 years, with

a target frequency of one week. Technical report, CEOP-AEGIS Deliverable Report De3.4, University of Strasbourg, France, ISSN 2118-7843: 27p.

Faivre, R., Colin, J., Roupioz, L., Ghafarian, H., Li, Z., Jia, L., Nerry, F., and Menenti, M. (2013). Validated time-series maps of fluxes over 3 years, with a frequency of one day. Technical report, CEOP-AEGIS Deliverable Report De3.5, University of Strasbourg, France, ISSN 2118-7843: 22p.

Feddes, R. A. (1971). *Water, heat and crop growth*. PhD thesis, Agricultural University, Wageningen, The Netherlands.

Ghafarian, H., Menenti, M., Jia, L., and Ouden, H. (2012). Reconstruction of cloud-free time-series satellites observations of land surface temperature. *EARSel eProceedings*, 11(2):123–131.

Gowda, P. H., Chavez, J. L., Colaizzi, P. D., Evett, S. R., Howell, T. A., and Tolk, J. A. (2007). Remote sensing based energy balance algorithms for mapping et: Current status and future challenges. *Transactions of the ASABE*, 50(5):1639–1644.

Hall, A. E., Canell, G. H., and Lawton, H. W. (1979). *Agriculture in semi-arid environments*. Springer-Verlag Berlin Heidelberg New York.

Hofton, M. A., Rocchio, L., Blair, J., and Dubayah, R. (2002). Validation of vegetation canopy lidar sub-canopy topography measurements for a dense tropical forest. *Journal of Geodynamics*, 34(3-4):491–502.

Hong, S. and Lim, J. J. (2006). The wrf single-moment 6-class microphysics scheme (wsm6). *Journal of the Korean Meteorological Society*, 42:129–151.

Hong, S.-H., Noh, Y., and Dudhia, J. (2005). A new vertical diffusion package with an explicit treatment of entrainment processes. *American Meteorological Society*, 134:2318–2341.

Huband, N. D. S. and Monteith, J. L. (1986). Radiative surface temperature and energy balance of a wheat canopy. *Boundary Layer Meteorology*, 36:1–17.

Iqbal, M. (1983). *An introduction to solar radiation*. Academic Press Canada.

Jackson, R. D., Hatfield, J. L., Reginato, R. J., Idso, S. B., and Pinter, P. J. (1983). Estimation of daily evapotranspiration from one-time-of-day measurement. *Agricultural Water Management*, 7(3):351–362.

Jackson, R. D., Kustas, W. P., and Choudhury, B. J. (1988). A re-examination of the crop-water stress index. *Irrig. Sci.*, 9:309–317.

Jackson, R. D., Reginato, R. J., and Idso, S. B. (1977). Wheat canopy temperatures : a practical tool for evaluating water requirements. *Water Ressources Research*, 13:651–656.

Jia, L. (2004). *Modeling heat exchanges at the land-atmosphere interface using multi-angular thermal infrared measurements*. PhD thesis, Wageningen University, Netherlands.

Jia, L., Li, Z., Ruan, Z., Hu, G., Yang, J., and Menenti, M. (2012a). Improving accuracy in land surface heat and water fluxes estimation by multi-parameterizations and multi-source satellite observations. In *ESA-MOST Dragon 2 Final Results*, volume SP-704. European Space Agency.

Jia, L., Li, Z. L., Menenti, M., Su, Z., Verhoef, W., and Wan, Z. (2003a). A practical algorithm to infer soil and foliage component temperatures from bi-angular atsr-2 data. *International Journal of Remote Sensing*, 24(23):4739–4760.

Jia, L., Menenti, M., Nerry, F., Najjar, G., Stoll, M.-P., and Su, Z. (2001). Evaluation of the surface energy balance index with the field and airborne data collected at hartheim and colmar. In *Final Results workshop on DAISEX (Digital Airborne Spectrometer EXperiement)*, volume SP-499, pages 235–240. ESTEC-ESA.

Jia, L., Su, Z., Hurk, B. v. d., Menenti, M., Moene, A., Bruin, H. A. R. D., Yrisarry, J. J. B., Ibanez, M., and Cuesta, A. (2003b). Estimation of sensible heat flux using the surface energy balance system (sebs) and atsr measurements. *Physics and Chemistry of the Earth*, 28:75–88.

Jia, L., Xi, G., Liu, S., Huang, C., Yan, Y., and Liu, G. (2009). Regional estimation of daily to annual regional evapotranspiration with modis data in the yellow river delta wetland. *Hydrology and Earth System Sciences*, 13:1775–1787.

Jia, Z., Liu, S., Xu, Z., Chen, Y., and Zhu, M. (2012b). Validation of remotely sensed evapotranspiration over the hai river basin, china. *Journal of Geophysical Research*, 117(D13113):21.

Kain, J. S. and Fritsch, J. M. (1990). A one-dimensional entraining/detraining plume model and its application in convective parameterization. *Journal of the Atmospheric Sciences*, 47:2784–2802.

Ketchum Jr., R. D. (1971). Airborne laser profiling of the arctic pack ice. *Remote Sensing of Environment*, 2(C):41–52.

Kustas, W. P., Choudhury, B. J., Kunkel, K. E., and Gay, L. W. (1989a). Estimate of the aerodynamic roughness parameters over an incomplete canopy cover of cotton. *Agricultural and Forest Meteorology*, 46:91–105.

Kustas, W. P., Choudhury, B. J., Moran, M. S., Reginato, R. J., Jackson, R. D., Gay, L. W., and Weaver, H. L. (1989b). Determination of sensible heat flux over sparse canopy using thermal infrared data. *Agricultural and Forest Meteorology*, 44:197–216.

Kustas, W. P. and Daughtry, C. S. T. (1989). Estimation of the soil heat flux/net radiation ratio from spectral data. *Agric. For. Meteorol.*, 49:205–223.

Kustas, W. P. and Norman, J. (1999). Evaluation of soil and vegetation heat flux predictions using a simple two-source model with radiometric temperatures for partial canopy cover. *Agricultural and Forest Meteorology*, 46:91–105.

Lettau, H. (1969). Note on aerodynamic roughness-parameter estimation on the basis of roughness-element description. *J. Appl. Meteorol.*, 8(5):828–832.

Lhomme, J.-P., Monteny, B., and Amadou, M. (1994). Estimating sensible heat flux from radiometric temperature over sparse millet. *Agricultural and Forest Meteorology*, 68:77–91.

Li, F., Qiang, L., Qing, X., Qinhuo, L., and Zhigang, L. (2009a). Design and implementation of airborne wide-angle infrared dual-mode line/area array scanner in heihe experiment. *Advances in Earth Sciences*, 24(7):696–705.

Li, X., Cheng, G., Liu, S., Xiao, Q., Ma, M., Jin, R., Che, T., Liu, Q., Wang, W., Qi, Y., Wen, J., Li, H., Zhu, G., Guo, J., Ran, Y., Wang, S., Zhu, Z., Zhou, J., Hu, X., and Xu, Z. (2013). Heihe watershed allied telemetry experimental heihe watershed allied telemetry experimental research (hiwater) : Scienctific objectives and experimental design. *American Meteorological Society*, 94:1145–1160.

Li, X., Li, X. i., Li, Z., Ma, M., Wang, J., Xiao, Q., Liu, Q., Che, T., Chen, E., Yan, G., Hu, Z., Zhang, L., Chu, R., Su, P., Liu, Q., Liu, S., Wang, J., Niu, Z., Chen, Y., Jin, R., Wang, W., Ran, Y., Xin, X., and Ren, H. (2009b). Watershed allied telemetry experimental research. *Journal of Geophysical Research D: Atmospheres*, 114(22).

Li, Z.-L., Jia, L., Su, Z., Wan, Z., and Zhang, R. (2003). A new approach for retrieving precepitable water water from atsr2 split-window channel data over land area. *International Journal of Remote Sensing*, 24:5059–5117.

Li, Z.-L., Tang, R., Wan, Z., Bi, Y., Zhou, C., Tang, B., Yan, G., and Zhang, X. (2009c). A review of current methodologies for regional evapotranspiration estimation from remotely sensed data. *Sensors*, 9:3801–3853.

Liu, X., Zheng, H., and Immerzeel, W. (2013). Time series analysis of water balance data. Technical report, CEOP-AEGIS Deliverable Report De8.3, University of Strasbourg, France, ISSN 2118-7843: 15p.

Lohou, F. and Patton, E., G. (2014). Surface energy balance and boyancy response to shallow cumulus shading. *Journal of the Atmospheric Sciences*, 71(2):665–682.

Lopes, A. M. G. (2003). Windstation - a software for the simulation of atmospheric flows over complex topography. *Environmental Modelling and Software*, 18(1):81–96.

MacDonald, R. W., Griffiths, R. F., and Hall, D. J. (1998). An improved method for the estimation of surface roughness of obstacle arrays. *Atmospheric Environment*, 32(11):1857–1864.

Massman, W. J. (1999). A model study of kbh-1 for vegetated surfaces using localized near-field' lagrangian theory. *Journal of Hydrology*, 223:27–43.

McNaughton, K. G. and Raupach, M. R. (1996). *Scaling up in hydrology using remote sensing*, chapter Responses of the convective boundary layer and the surface energy balance to large scale heterogeneity, pages 171–182. Wiley and Sons, Chichester, England.

Mellor, G. L. and Yamada, T. (1982). Development of a turbulence closure model for geophysical fluid problems. *Reviews of Geophysics and Space Physics*, 20:851–875.

Menenti, M. (1984). *Physical aspects and determination of evaporation in deserts applying remote sensing techniques*. PhD thesis, Wageningen Agricultural University, Wageningen, The Netherlands.

Menenti, M. (2000). *Remote sensing in hydrology and water management*, chapter 8 : Evaporation, pages 157–188. Springer.

Menenti, M. and Choudhury, B. J. (1993). Parameterization of land surface evaporation by means of location dependent potential evaporation and surface temperature range. *Exchange Processes at the Land Surface for a Range of Space and Time Scales, Proceedgins of the Yokohama Symposium, IAHS Publication*, (212):561–568.

Menenti, M., Colin, J., Faivre, R., Roupioz, L., and Jia, L. (2010). Generalization of the surface energy balance calculation over the tibetan plateau. Technical report, CEOP-AEGIS Deliverable Report De3.2, University of Strasbourg, France, ISSN 2118-7843: 32p.

Menenti, M., Jia, L., Li, Z.-L., Djepa, V., Wang, J., Stoll, M.-P., Su, Z., and Rast, M. (2001). Estimation of soil and vegetation temperatures with multiangular thermal infrared observations : Imgrass, heife and sgp 1997 experiments. *Journal of Geophysical Research*, D11(11997-12010).

Menenti, M. and Ritchie, J. C. (1994). Estimation of effective aerodynamic roughness of walnet gulch watershed with laser altimeter measurements. *Water ressources research*, (5):1329–1337.

Menenti, M., Ritchie, J. C., Humes, K. S., Parry, R., Pachepsky, Y., Gimenez, D., and Leguizamon, S. (1996). Estimation of scale dependent effective roughness lengths for momentum with laser and radar altimeter data.

Mlawer, E. J., Taubman, S. J., Brown, P. D., Iacono, M. J., and Clough, S. A. (1997). Radiative transfer for inhomogeneous atmospheres: Rrtm, a validated correlated-k model for the longwave. *Journal of Geophysical Research : Atmospheres*, 102(D14):16,663–16,682.

Monteith, J. L. (1965). Evaporation and environment. In Fogg, G., editor, *The State and Movement of Water in Living Organisms*, pages 205–234, New York. Sympos. Soc. Exper. Biol., Academic Press.

Monteith, J. L. and Unsworth, M. H. (1973). *Principles of environmental physics*. Edward Arnold Press.

Moran, M. S. (1990). *A satellite-based approach for evaluation of the spatial distribution of evapotranspiration from agricultural lands*. PhD thesis, University of Arizona.

Mu, Q., Zhao, M., and Running, S. W. (2013). Modis global terrestrial evapotranspiration (et) product. Technical report, NASA.

Murray, T. and Verhoef, A. (2007). Moving towards a more mechanistic approach in the determination of soil heat flux from remote measurements. a universal approach to calculate thermal inertia. *Agricultural and Forest Meteorology*, 147:80–87.

Norman, J. M., Kustas, W. P., and Humes, K. S. (1995). Two-source approach for estimating soil and vegetation energy fluxes in observations of directional

radiometric surface temperature. *Agricultural and Forest Meteorology*, 77:263–293.

Onogi, K., Tsutsui, J., Koide, H., Sakamoto, M., Kobayashi, S., Hatsushika, H., Matsumoto, T., Yamazaki, N., Kamahori, H., Takahashi, K., Kadokura, S., Wada, K., Kato, K., Oyama, R., Ose, T., Mannoji, N., and Taira, R. (2007). The jra-25 reanalysis. *Journal of the Meteorological Society of Japan. Ser. II*, 85(3):369–432.

Owen, P. R. and Thomson, W. R. (1968). Heat transfer across rough surfaces. *Journal of Fluid Mechanics*, (15):321–324.

Penman, H. L. (1948). Natural evaporation from open water, bare soil, and grass. volume A193, pages 120–146, London. The Royal Society A.

Pleim, J. E. (2006). A simple, efficient solution of flux-profile relationships in the atmospheric surface layer. *Journal of Applied Meteorology and Climatology*, 45(341-347).

Prata, F. (2002). Land surface temperature measurement from space : Aatsr algorithm theoretical basis document. Technical report, CSIRO Atmospheric Research Aspendale, Australia.

Prévot, H. L., Paw, U. K. T., and Seguin, B. (1994). Canopy modelling for estimating sensible heat flux from thermal infrared measurements. In *Workshop on Thermal Remote Sensing of The Energy And Water Balance Over Vegetation in Conjunction With Other Sensors*, pages 17–22.

Price, J. (1982). On the use of satellite data to infer surface fluxes at meteorological scales. *Journal of Applied Meteorology*, 21:1111–1122.

Price, J. (1990). Using spatial context in satellite data to infer regional scale evapotranspiration. *IEEE Transactions on Geoscience and Remote Sensing*, 28(5):940–948.

Raupach, M. R. (1994). Simplified expressions for vegetation roughness length and zero-plane displacement as functions of canopy height and area index. *BOUNDARY-LAYER METEOROL.*, 71(1-2):211–216.

Roerink, G., Su, Z., and Menenti, M. (2000). S-sebi: A simple remote sensing algorithm to estimate the surface energy balance. *Physics and Chemistry of the Earth*, 25(2):147–157.

Rosenberg, N. J., Blad, B. L., and Verma, S. B. (1983). *Microclimate, The biological environment*. John Wiley and Sons, New York.

Schuepp, P., Leclerc, M., and Macpherson, J. (1990). Footprint prediction of scalar fluxes from analytical solutions of the diffusion equation. *Boundary-Layer Meteorology*, 50(1-4):353–373.

Skamarock, W., Klemp, J., Dudhia, J., Gill, D., Barker, D., Duda, M., Huang, X., Wang, W., and Powers, J. (2008). A description of the advanced research wrf version 3, ncar technical note. Technical report, Mesoscale and Microscale Meteorology Division, National Center for Atmospheric Research, Boulder, Colorado, USA.

Stewart, J. B. (1995). Turbulent surface fluxes derived from radiometric surface temperature osf sparse prairie grass. *Journal of Geophysical Research*, 100(D12):25429–25433.

Streutker, D. R. and Glenn, N. (2006). Lidar measurement of sagebrush steppe vegetation heights. *Remote Sensing of Environment*, 102(1-2):135–145.

Su, H., McCabe, M., Wood, E. F., Su, Z., and Prueger, J. H. (2005). Modeling evapotranpiration during smacex : comparing two approaches for local and regional-scale prediction. *Journal of Hydrometeorology*, 6:910–922.

Su, Z. (2002). The surface energy balance system (sebs) for estimation of turbulent heat fluxes at scales ranging from a point to a continent. *Hydrology and Earth System Sciences*, 6(1):85–99.

Su, Z. (2005). Hydrological application of remote sensing: Surface fluxes and other derived variables - surface energy balance (latent and sensible heating, net radiation). *Encyclopedia of Hydrological Sciences*, pages 1–22.

Su, Z., Li, X., Zhou, Y., Wan, L., Wen, J., and Sintonen, K. (2003). Estimating aeral evaporation from remote sensing. *Proc. IEEE Int.*, 2:1166–1168.

Su, Z., Schmugge, T., Kustas, W. P., and Massman, W. J. (2001). An evaluation of two models for estimation of the roughness height for heat transfer between the land surface and the atmosphere. *Journal of Applied Meteorology*, 40:1933–1951.

Sugita, M. and Brutsaert, W. (1990). Regional fluxes from remotely sensed skin temperature and lower boundary layer measurements. *Water Resources Research*, 26(12):2937–2944.

Sugita, M. and Brutsaert, W. (1991). Daily evaporation over a region from lower boundary layer profiles measured with radiosondes. *Water Resources Research*, 27:747–752.

Suttleworth, W. J., Gurney, R. J., Hsu, A. Y., and Ormbsby, J. P. (1989). Fife : the variations in energy partition at surface flux sites. In Publications, I., editor, *Proceedings of the IAHS Third International Assembly*, volume 186, pages 67–74.

Taconet, O. and Vidal-Madjar, D. (1988). Application of a flux algorithm to a field-satellite campaign over vegetated area. *Remote sensing of environment*, 26(3):227–239.

Tang, B., Bi, Y., Li, Z. L., and Xia, J. (2008). Generalized split-window algorithm for estimate of land surface temperature from chinese geostationary fengyun meteorological satellite (fy-2c) data. *Sensors*, 8:933–951.

Tang, B.-H. and Li, Z.-L. (2011). Algorithms for surface albedo, emissivity and temperature from geostationary satellite. Technical report, CEOP-AEGIS Deliverable Report De2.3, University of Strasbourg, France, ISSN 2118-7843: 25p.

Taylor, P. A. a. b., Sykes, R.I.c, Mason, and P.J.d (1989). On the parameterization of drag over small-scale topography in neutrally-stratified boundary-layer flow. *Boundary-Layer Meteorology*, 48(4):409–422.

Theurer, W. (1993). *Dispersion of ground-level emissions in complex built-up areas*. PhD thesis, Doctoral Thesis, Department of Architecture, University of Karlsruhe, Germany.

Thom, A. S. (1972). Momentum, mass, anfd heat exchange of vegetation. *Quarterly Journal of the Royal Meteorological Society*, 98:124–134.

Thornton, P. E., Running, S. W., and White, M. A. (1997). Generating surfaces of daily meteorological variables over large regions of complex terrain. *Journal of Hydrology*, 190:214–251.

Twine, T. E., Kustas, W. P., Norman, J. M., Cook, D. R., Houser, P. R., Meyers, T. P., Prueger, J. H., Starks, P. J., and Wesley, M. L. (2000). Correcting eddy-covariance flux underestimates over a grassland. *Agricultural and Forest Meteorology*, 103:279–300.

Ueno, K., Sugimoto, S., Koike, T., Tsutsui, H., and Xu, X. (2011). Generation processes of mesoscale convective systems following midlatitude troughs around the sichuan basin. *Journal of Geophysical Research D: Atmospheres*, 116:15 p.

Van de Griend, A. and Owe, M. (1993). On the relationship between thermal emissivity and the normalized difference vegetation index for natural surfaces. *International Journal of Remote Sensing*, 14(6):1119–1131.

Verhoef, A., Bruin, H. A. R. D., and HURK, B. J. J. M. V. d. (1997). Some practical notes on the parameter kb-1 for sparse vegetation. *Journal of Applied Meteorology*, 36(5):560–572.

Verma, S. B. (1989). Aerodynamic resistances to transfers of heat, mass and momentum. estimation of areal evapotranspiration. *International Association of Hydrological Sciences*, (177):13–20.

Verma, S. B., Rosenberg, N. J., Blad, B. L., and Baradas, N. W. (1976). Resistance-energy balance method for predicting evapotranpiration, determination of boundary layer resistance, and evaluation of error effects. *Agronomy Journal*, 68:776–782.

Wang, C., Menenti, M., Stoll, M.-P., Feola, A., Belluco, E., and Marani, M. (2009). Separation of ground and low vegetation signatures in lidar measurements of salt-marsh environments. *IEEE Transactions on Geoscience and Remote Sensing*, 47(7):2014–2023.

Wieringa, J. (1998). How far can agrometeorological station observations be considered representative? In *23rd Conference on Agriculture and Forest Meteorology*.

Wieringa, J., Davenport, A. G., Grimmond, C. S. B., and Oke, T. R. (2001). New revision of davenport roughness classification. In *3rd European and African Conference on Wind Engineering, Eindovhen, Netherlands*.

Wittich, K.-P. and Hansing, O. (1995). Area-averaged vegetative cover fraction estimated from satellite data. *International Journal of Biometeorology*, 38(209-215).

Wood, E. F., Su, H., McCabe, M., and Su, Z. (2003). Estimating evaporationfrom satellite remote sensing. *IGARSS*, pages 21–25.

Wooding, R. A. a., Bradley, E., and Marshall, J. (1973). Drag due to regular arrays of roughness elements of varying geometry. *Boundary-Layer Meteorology*, 5(3):285–308.

Xue, J. S., Zhuang, S. Y., Zhu, G. F., Zhang, H., Liu, Z. Q., Liu, Y., and Zhuang, Z. R. (2008). Scientific design and preliminary results of three-dimensional variational data assimilation system of grapes. *Chinese science bulletin*, 53(22):3446–3457.

Yan, G., Li, Z.-L., Tang, B.-H., Xiao, Z., Mu, X., Jia, L., Yang, J., Liu, Q., Li, J., and Liu, Q. (2011a). Description of land surface properties retrieved

from spectro-radiometric data in the optical spectral region. Technical report, CEOP-AEGIS Deliverable Report De2.5, University of Strasbourg, France, ISSN 2118-7843: 13p.

Yan, G., Verhoef, W., Liu, Q., Xiao, Z., Menenti, M., Jia, L., Liu, Q., Mu, X., Li, J., Zhong, B., and Ren, H. (2011b). Multi-source remote sensing, algorithm theoretical basis document. Technical report, CEOP-AEGIS Deliverable Report De2.4, University of Strasbourg, France, ISSN 2118-7843: 136p.

Zhang, R. H. and Shen, X. S. (2008). On the development of the grapes - a new generation of the national operational nwp system in china. *Chinese Science Bulletin*, 53(22):3429–3432.

Zheng, H., Immerzeel, W., D'Urso, G., and Colin, J. (2011). Design of data processing protocol for eo based water balance products. Technical report, CEOP-AEGIS Deliverable Report De8.1, University of Strasbourg, France, ISSN 2118-7843: 34p.

Zhu, G. F., Xue, J. S., Zhang, H., Liu, Z. Q., Zhuang, S. Y., Huang, L. P., and Dong, P. M. (2008). Direct assimilation of satellite radiance data in grapes variational assimilation system. *Chinese science bulletin*, 53(22):3465–3469.

Zhuang, S., Wan, Q., Guofu, Z., and Jishan, X. (2005). Grapes 3dvar and its preliminary application on remote sensing data assimilation. In *2005 IEEE International Geoscience and Remote Sensing Symposium, 2005. IGARSS'05. Proceedings*, volume 1.

List of publications

Articles

- Colin J., Faivre R., *Aerodynamic roughness length estimation from very high-resolution imaging LIDAR observations over the Heihe basin in China*, Hydrology and Earth System Sciences, Special issue: Observing and modeling the catchment-scale water cycle, 14, 2010.

Proceedings

- Faivre R., Colin J., Menenti M., Lindenbergh R., Van Den Bergh., Yu H., Jia L., Xin L., *Project 5322 Mid-Term Report, Key eco-hydrological parameters retrieval and land data assimilation system development in a typical inland river basin of china's arid region*, European Space Agency, Dragon 2 Mid-Term results Symposium, Guilin, P.R. of China, May 2010.

- Colin J., Menenti M., Faivre R., Liu Q., Shen X., *Turbulent flux partitioning from local to meso scale over high elevation arid regions of China*, European Space Agency, Living Planet Symposium, Bergen, Norway, June 2010, in proceedings (SP-686).

- Faivre R., Ghafarian H., Tang B., Colin J., Jia L., Roupioz L., *Multi-annual data products on turbulent heat fluxes at the local and continental scale using AATSR and FY-2 data*, Dragon 2 Final results Symposium, Beijing, P.R. of China, June 2012, in proceedings (SP-704).

Reports

- Menenti, M., Colin, J., Faivre, R., Roupioz, L., Jia, L., 2010, *Generalization of the surface energy balance calculation over the Tibetan Plateau*, CEOP-AEGIS Deliverable Report De3.2, Ed. University of Strasbourg, France, ISSN 2118-7843: 32 p.

- Colin, J., Roupioz, L., Ghafarian, H., Bai, J., Jia, L., Liu, S.M., Faivre, R., Nerry, F., Menenti, M., 2011, *Surface Radiative and Energy Balance time-series processing and validation procedure document*, CEOP-AEGIS Deliverable Report De3.3, Ed. University of Strasbourg, France, ISSN 2118-7843: 34 p.

- Faivre, R., Colin, J., Roupioz, L., Ghafarian, H., Li, Z., Jia, L., Nerry, F., Menenti, M., 2012, *Preliminary time-series maps of fluxes over 3 years, with a target frequency of one week*, CEOP-AEGIS Deliverable Report De3.4, Ed. University of Strasbourg, France, ISSN 2118-7843: 27 p.

- Faivre, R., Colin, J., Roupioz, L., Ghafarian, H., Jia, L., Menenti, M., 2012, *Multi-scale parameterization of turbulent heat fluxes for heterogeneous land surfaces*, European Space Agency, Dragon 2 Final Report.

- Faivre, R., Colin, J., Roupioz, L., Ghafarian, H., Li, Z., Jia, L., Nerry, F., Menenti, M., 2013, *Validated time-series maps of fluxes over 3 years, with a frequency of one day*, CEOP-AEGIS Deliverable Report De3.5, Ed. University of Strasbourg, France, ISSN 2118-7843: 22 p.

Posters

- Faivre R., Colin J., Menenti M., *Investigations on roughness length retrieval from very-high resolution optical remote sensing for turbulent flux estimation over Heihe River basin in China*, Dragon 2 Mid-Term results Symposium, Guilin, P.R. of China, May 2010.

- Faivre R., Colin J., Jia L., Menenti M., *Multi-scale parameterization of turbulent heat fluxes : a case study from local to meso-scale over Heihe River basin*, Dragon 2 Mid-Term results Symposium, Guilin, P.R. of China, May 2010.

- Faivre R., Colin J., Menenti M., *Coupling of meso-scale atmospheric model and AATSR data for turbulent heat fluxes parameterization over the Heihe River basin*, Dragon 2 Symposium, Prague, Chezh Republic, June 2011.

- Faivre R., Colin J., Ghafarian H., Menenti M., *Medium resolution parameterization of turbulent heat fluxes over the Tibetan Plateau*, Dragon 2 Final results Symposium, Beijing, P.R. of China, June 2012.

- Faivre R., Colin J., Menenti M., Ghafarian H., Tang B., Shen X., *A 3-year time serie of daily actual evaporation over the Tibetan Plateau*, CEOP-AEGIS final meeting, Beijing, P.R. of China, April 2013.

Robin Faivre

Multi-sensor remote sensing parameterization of heat fluxes over heterogeneous land surfaces

Résumé

La paramétrisation du transfert de chaleur par télédétection, basée sur le schéma SEBS, s'est déjà avérée très adaptée pour l'estimation de l'évapotranspiration (*ET*) sur des surfaces naturelles homogènes. Cependant, l'utilisation d'une telle méthode pour des paysages hétérogènes (e.g. régions semi-arides ou surfaces agricoles) est plus délicate, puisque le principe de la théorie de la similarité est compromis par la présence de différentes sources de chaleur et de hauteurs variées.
Dans un premier temps, cette thèse a pour objectif de proposer et d'évaluer différents modèles basés sur la géométrie de la végétation qui permettent d'estimer la longueur de rugosité pour le transfert de quantité de mouvement à la surface (z_{0m}), cette dernière étant un paramètre clé dans la caractérisation du transfert de chaleur. En revanche, une telle investigation ne peut être menée qu'à une petite échelle et à l'aide de données de télédétection très haute résolution permettant ainsi une description très détaillée de la surface. Ensuite, le second aspect de ce travail est de caractériser le transfert de chaleur dans le cas d'études régionales. Puis, la capacité de SEBS à estimer les flux de chaleur turbulents à de grandes échelles spatiales et temporelles sera évaluée. Pour ce faire, l'approche multi-échelle de SEBS (MSSEBS) a été implémentée afin de traiter une zone de 2,4 millions km^2, incluant le Plateau du Tibet et l'amont des principaux fleuves d'Asie du sud-est. La combinaison de données horaires de température de surface FY-2 avec un rayonnement net journalier et des paramètres de surface avancés, permet de produire une série temporelle d'*ET* sur le Plateau du Tibet pour la période 2008-2010, et à une fréquence journalière.

Mots clés : Télédétection optique, surfaces naturelles hétérogènes, bilan d'énergie, transfert de chaleur, évapotranspiration, longueur de rugosité, échelles spatiales et temporelles.

Abstract

The parameterization of heat transfer by remote sensing, and based on SEBS scheme for turbulent heat fluxes retrieval, already proved to be very convenient for estimating evapotranspiration (*ET*) over homogeneous land surfaces. However, the use of such a method over heterogeneous landscapes (e.g. semi-arid regions or agricultural land) becomes more difficult, since the principle of similarity theory is compromised by the presence of different heat sources with various heights.
This thesis aims at first to propose and evaluate some models based on vegetation geometry for retrieving the surface roughness length for momentum transfer (z_{0m}), which is a key parameter in the characterization of heat transfer. Such an investigation can only be led at a small scale with very-high resolution remote sensing data, for a precise description of the land surface. Therefore, the second aspect of this work is to determine how to address the characterization of heat transfer for regional studies. Then, the reliability of SEBS for estimating turbulent heat fluxes at large spatial and temporal scales has been evaluated. To do so, the Multi-Scale SEBS approach (MSSEBS) has been implemented for a 2.4 million km^2 area including the Tibetan Plateau and the headwaters of the major rivers of East and South Asia. The addition of gap-filled hourly FY-2 LST data to advanced daily averaged net radiation and land surface parameters, allows to compute time-series of land surface *ET* over the Tibetan Plateau during the period 2008-2010, and on a daily basis.

Keywords : Optical remote sensing, heterogeneous land surfaces, surface energy balance, heat transfer, evapotranspiration, roughness length, spatial and temporal resolutions.